KUOPION YLIOPISTON JULKAISUJA C. LUONNONTIETEET JA YMPÄRISTÖTIETEET 216
KUOPIO UNIVERSITY PUBLICATIONS C. NATURAL AND ENVIRONMENTAL SCIENCES 216

EVELIINA LAMMENTAUSTA

Structural and Mechanical Characterization of Articular Cartilage and Trabecular Bone with Quantitative NMR

Doctoral dissertation

To be presented by permission of the Faculty of Natural and Environmental Sciences of the University of Kuopio for public examination in Auditorium L22, Snellmania building, University of Kuopio, on Friday 28th September 2007, at 12 noon

Department of Physics
University of Kuopio

KUOPION YLIOPISTO
KUOPIO 2007

Distributor: Kuopio University Library
P.O. Box 1627
FI-70211 KUOPIO
FINLAND
Tel. +358 17 163 430
Fax +358 17 163 410
http://www.uku.fi/kirjasto/julkaisutoiminta/julkmyyn.html

Series Editors: Professor Pertti Pasanen, Ph.D.
Department of Environmental Science

Professor Jari Kaipio, Ph.D.
Department of Physics

Author's address: Department of Diagnostic Radiology
Oulu University Hospital
P.O. Box 50
FI-90029 OYS, Oulu
FINLAND
Tel. +358 8 315 2480
Fax +358 8 315 2112
E-mail: eveliina.lammentausta@gmail.com

Supervisors: Professor Jukka Jurvelin, Ph.D.
Department of Physics
University of Kuopio

Docent Miika Nieminen, Ph.D.
Department of Diagnostic Radiology
Oulu University Hospital

Reviewers: Senior Director Bernard Dardzinski, Ph.D.
Merck & Co., Inc.
West Point, PA, USA

Professor Felix Eckstein, M.D., Ph.D.
Institute for Anatomy and Musculoskeletal Research
Paracelsus Medical University
Salzburg, Austria

Opponent: Professor Sharmila Majumdar, Ph.D.
Department of Radiology
University of California, San Francisco
San Francisco, CA, USA

ISBN 978-951-27-0694-5
ISBN 978-951-27-0789-8 (PDF)
ISSN 1235-0486

Kopijyvä
Kuopio 2007
Finland

Lammentausta, Eveliina. Structural and mechanical characterization of articular cartilage and trabecular bone with quantitative NMR. Kuopio University Publications C. Natural and Environmental Sciences 216. 2007. 89 p.
ISBN 978-951-27-0694-5
ISBN 978-951-27-0789-8 (PDF)
ISSN 1235-0486

ABSTRACT

Osteoarthritis (OA) is the most common degenerative joint disease, impairing the quality of life of individuals and posing an economical burden to the society. The first degenerative changes are practically symptomless, which complicates the early diagnosis and development of treatment that would stop or even reverse the degeneration. Quantitative magnetic resonance imaging (MRI) has proved to be a promising tool for non-invasive evaluation of both articular cartilage and trabecular bone.

In the present study, the ability of quantitative MRI parameters to assess mechanical properties, structure and composition of human patellar cartilage and trabecular bone was investigated, as well as their ability to indicate the degree of degeneration. T_2 and Gd-DTPA^{2-}-enhanced T_1 relaxation times (dGEMRIC) of cartilage measured at 1.5 T and 9.4 T were related to proteoglycan (PG) and collagen content and mechanical parameters. In trabecular bone, T_2^* relaxation time and bone volume fraction derived from MR images were related to peripheral quantitative computed tomography (pQCT), histological and mechanical parameters. The histological Mankin score was utilized to determine the degree of cartilage degeneration. The ability of spectroscopic MR parameters of bone marrow was introduced as a novel method to assess the bovine trabecular structure as measured with microCT.

In articular cartilage, T_2 relaxation time showed the highest correlation with mechanical properties ($r = -0.62$, $p < 0.01$) at 1.5 T, whereas dGEMRIC provided the highest correlation at 9.4 T ($r=0.39$, $p < 0.01$). As expected, T_2 displayed a significant correlation with the collagen content (up to $r = -0.57$, $p < 0.01$), but also with PG content at 1.5 T ($r = -0.53$, $p < 0.01$). dGEMRIC correlated with PG content at 9.4 T ($r = 0.45$, $p < 0.01$) but not at 1.5 T. T_2 could detect the different degrees of cartilage degeneration at 1.5 T, and dGEMRIC detected advanced degeneration at 9.4 T. The topographical variation of T_2 at both field strengths showed similar trends with that of elastic modulus of cartilage, whereas dGEMRIC showed only weak topographical variation. For trabecular bone MRI, the modest correlation with mechanical properties was improved when MRI-derived BV/TV and T_2^* were combined into a linear model (up to $r = 0.50$, $p < 0.01$). No such improvement was achieved with pQCT parameters; however parameters measured with pQCT showed the best correlation with mechanical properties (up to $r = 0.65$, $p < 0.01$). Significant correlations were established between MRI parameters measured from bone and cartilage. Characteristically, higher correlations were observed when only samples with no or minimal degeneration were analyzed. Spectroscopic T_2, Carr-Purcell T_2 and $T_{1\rho}$ of trabecular bone showed significant relations (up to $r = -0.86$, $p < 0.05$) with structural parameters suggesting that spectroscopy may provide a fast tool for evaluating trabecular structure.

In conclusion, quantitative MRI parameters have proved feasible for use also in the clinical environment. However, the characteristic features of different articulating surfaces have to be considered. The present results highlight the need for a better understanding of the timeline of OA development and associated relaxation processes in both cartilage and bone.

Universal Decimal Classification: 543.429.23
National Library of Medicine Classification: QT 36, WN 185, WE 200, WE 300, WE 348, QS 532.5.C7
Medical Subject Headings: Biomedical Engineering; Magnetic Resonance Imaging; Biomechanics; Cartilage, Articular; Collagen; Proteoglycans; Bone and Bones; Bone Matrix; Osteoarthritis/diagnosis

To Ari

ACKNOWLEDGEMENTS

This study was carried out during the years 2004-2007 in the Department of Physics, University of Kuopio.

I owe my deepest gratitude to my primary supervisor, professor Jukka Jurvelin, Ph.D., for his inspiring and devoted supervision. It has been a privilege to work in his research group Biophysics of Bone and Cartilage (BBC).

I express my sincere thanks to my other supervisor docent Miika Nieminen, Ph.D., for being the essential advisor, band-mate and a friend.

I want to sincerely thank the official reviewers Senior researcher Bernard Dardzinski, Ph.D., and Professor Felix Eckstein, M.D.,Ph.D., for their constructive criticism to improve this thesis. I am grateful to Ewen Macdonald, D.Pharm., for linguistic revision.

It has been a pleasure to work with a colourful ensemble of skillful and devoted people. I want to thank Panu Kiviranta, B.M., for his assistance in the human patella measurements and for performing the histological measurements of cartilage samples. My "room-mates" Mikko Nissi, M.Sc., and Heikki Nieminen, Ph.D., deserve my gratitude for keeping up excellent spirit and interesting discussions - both work-related and non-work-related. In addition, I want to thank Mikko for invaluable help in the beginning of this research project. I thank Mikko Laasanen, Ph.D., Mikko Hakulinen, Ph.D., and Antti Kallioniemi, M.Sc. (eng.), for introducing me the reference measurement methods, and Tuomo Silvast, M.Sc., for performing the microCT measurements of bovine samples. I am grateful to docent Juha Töyräs, Ph.D., for his advice in Mankin score grading of cartilage samples. I wish to thank physics student Pauno Lötjönen for his tireless help on preparation of bovine knee samples and Erna Kaleva, M.Sc., for being my eyes, ears and Postman Pat in Kuopio during the last year. I cherish the spirit of the BBC group and would like to thank Rami Korhonen, Ph.D., Simo Saarakkala, Ph.D., Petro Julkunen, M.Sc. (eng.), Janne Karjalainen, M.Sc. (eng.), Jatta Kurkijärvi, M.Sc., Ossi Riekkinen, M.Sc., Jarno Rieppo, M.D., and Matti Timonen, B.Sc.

I am grateful to Mika Hyttinen, M.D., for help in the microscopic measurements of trabecular bone. I gratefully acknowledge Ilkka Kiviranta, M.D., Ph.D., for providing invaluable human samples and truly constructive comments and encouragement. I wish to express my thanks to Professor Heikki Helminen, M.D., Ph.D., for his fatherly encouragement, and the personnel of the Institute of Biomedicine, Anatomy, for help, especially to Mrs. Eija Rahunen for the preparation of the histological samples.

I am indebted to Research director Olli Gröhn, Ph.D., for his enthusiasm and patience in guiding me through the mysterious world of spectroscopic measurements, and to Johanna Närväinen, Ph.D., for her essential contribution in the preparation of the fourth manuscript. I also would like to thank the NMR research group at the Department of Neurobiology, A.I. Virtanen Institute.

I wish to send my thanks to professor Osmo Tervonen, M.D., Ph.D., at the Department of Diagnostic Radiology, Oulu University Hospital, for support and encouragement considering the finishing of this thesis as well as other research projects. I also would like to thank the personnel at the Department of Diagnostic Radiology, Oulu University Hospital, especially the folks along the Geek Corridor for the inspiring and informal atmosphere.

Atria Lihakunta Oyj, Kuopio, Finland, is acknowledged for providing bovine joints as a research material.

I would like to thank all my friends, relatives, and my colleagues in the field of music for understanding and helping me to keep my thoughts occationally away from work.

I will always be grateful to my parents Risto and Kirsti Lammentausta for their unselfish support and encouragement during my studies, and my brother Veli-Matti Lammentausta for his tireless technical help.

Finally, I want to express my deepest thanks to my husband Ari for his unconditional love and support. The adventures we share make my efforts meaningful.

The financial support by the Academy of Finland (grant no. 205886), the Finnish Academy of Science and Letters, Vilho, Yrjö and Kalle Väisälä Foundation, the Finnish Cultural Foundation of Northern Savo and the Radiological Society of Finland is gratefully acknowledged.

Oulu, September 2007

Eveliina Lammentausta

ABBREVIATIONS

AHP	adiabatic half-passage
BMD	bone mineral density
CL	central lateral
CM	central medial
CP	Carr-Purcell
CT	computed tomography
DTPA	diethylenetriaminepentaacetic acid
DXA	dual-energy X-ray absorptiometry
dGEMRIC	delayed gadolinium-enhanced MRI of cartilage
ECM	extracellular matrix
EDTA	ethylenediaminetetraacetate acid
FCD	fixed charge density
FEM	femur
FFT	finite Fourier transform
FID	free induction decay
FLASE	fast large-angle spin echo
FTIRI	Fourier transform infrared imaging
GAG	glycosaminoglycan
HS	hyperbolic secant
IL	inferolateral
IM	inferomedial
JSN	joint space narrowing
LASER	localization by adiabatic selective refocusing
MRI	magnetic resonance imaging
MRS	magnetic resonance spectroscopy
MT	magnetization transfer
NMR	nuclear magnetic resonance
OA	osteoarthritis
OP	osteoporosis
PAT	patella
PG	proteoglycan
pQCT	peripheral quantitative computed tomography
QCT	quantitative computed tomography
RF	radiofrequency
ROI	region of interest
SD	standard deviation
SL	superolateral
SM	superomedial
SSFP	steady-state free precession
STEAM	stimulated echo acquisition mode

SYMBOLS

A	atomic mass number
a_c	contact radius of indenter
app.BV/TV	apparent bone volume fraction
B_0	static magnetic field
B_1	magnetic field induced by RF pulse
$B_{1\mathrm{SL}}$	magnetic field induced by spin-lock RF pulse
B_{ext}	external magnetic field
B_{xy}	magnetic field in xy-plane
B_z	magnetic field in z-direction
BV/TV	bone volume fraction
$\mathrm{BV/TV_{GE}}$	BV/TV determined from gradient echo measurements
$\mathrm{BV/TV_{SE}}$	BV/TV determined from spin echo measurements
$\mathrm{BV/TV_{pQCT}}$	BV/TV determined with pQCT measurements
$\mathrm{BV/TV_{REF}}$	BV/TV determined with reference method (microscopy)
b	$\gamma^2 G^2(\Delta - \delta/3)$, parameter of diffusion measurement
C	concentration of contrast agent
CP-T_2	Carr-Purcell T_2 relaxation time
D	diffusion coefficient
$\mathrm{dGEMRIC_b}$	dGEMRIC of bulk tissue
$\mathrm{dGEMRIC_s}$	dGEMRIC of superficial tissue
E	energy
e	Euler's number
E_1	storage modulus
E_2	loss modulus
E_{d}	dynamic modulus
$E_{\mathrm{d,c}}$	dynamic modulus of cartilage
E_{s}	Young's (elastic) modulus
$E_{\mathrm{s,b}}$	Young's modulus of cartilage
$E_{\mathrm{s,c}}$	Young's modulus of bone
ETL	echo train length
G	amplitude of diffusion encoding gradient
$[\mathrm{Gd\text{-}DTPA}^{2-}]_{\mathrm{b}}$	$\mathrm{Gd\text{-}DTPA}^{2-}$ concentration in bath
$[\mathrm{Gd\text{-}DTPA}^{2-}]_{\mathrm{t}}$	$\mathrm{Gd\text{-}DTPA}^{2-}$ concentration in tissue
H_a	aggregate modulus
h	cartilage thickness
I_{b}	signal intensity of bone
I_{m}	signal intensity of marrow
I_{roi}	signal intensity of region of interest
k	Boltzmann's constant
M	net magnetization
MIL	mean intercept length
M_0	initial (net) magnetization
M_x	magnetization in x-direction
M_y	magnetization in y-direction

M_z	magnetization in z-direction
$M_\perp$	magnetization in xy-plane
$M_{\perp,0}$	initial magnetization in xy-plane
m_s	quantum number corresponding to angular momentum operator
N	number of neutrons in a nucleus
n_s	number of spins at certain energy state
OD	optical density
p	the probability of obtaining a certain result, statistical significance
r	linear correlation coefficient
R_1	T_1 relaxation rate
$R_{1\rho}$	$T_{1\rho}$ relaxation rate
R_2	T_2 relaxation rate
R_2^*	T_2^* relaxation rate
S	factor representing the accuracy of 180°pulse
s	nuclear spin angular momentum
SAR	specific absorption rate
SMI	structural model index
SNR	signal to noise ratio
T	absolute temperature
t	time
T_1	spin-lattice relaxation time
T_2	spin-spin relaxation time
$T_{2,\mathrm{b}}$	T_2 of bulk tissue
$T_{2,\mathrm{s}}$	T_2 of superficial tissue
T_2'	component of T_2 relaxation time induced by field inhomogeneities
T_2^*	apparent spin-spin relaxation time
$T_{2,\mathrm{intr}}$	intrinsic T_2 relaxation time
$T_{2,\mathrm{diff}}$	component of T_2 relaxation time affected by diffusion
$T_{2,\mathrm{exch}}$	component of T_2 relaxation time affected by proton exchange
$T_{1\rho}$	spin-lattice relaxation time in rotating frame
$T_{1\rho,\mathrm{f}}$	$T_{1\rho}$ of fat
$T_{1\rho,\mathrm{w}}$	$T_{1\rho}$ of water
TM	mixing time
t_D	diffusion time
$T_{1,0}$	T_1 relaxation time of tissue without contrast agent
TE	echo time
TI	inversion time
TR	repetition time
TSL	spin-lock time
Tb.Th	trabecular thickness
Tb.Sp	trabecular separation
Tb.N	trabecular number
Z	number of protons in a nucleus

α_1	T_1 relaxivity
γ	gyromagnetic ratio
Δ	time difference between diffusion encoding gradients
δ	duration of diffusion encoding gradient
ϵ	strain
$\hbar$	Dirac's constant
κ	theoretical scaling factor related to indentation geometry
ν	Poisson's ratio
θ	angle between $\vec{B}_0$ and vector joining two dipoles
σ	stress
σ_{d}	dynamic stress
σ_{u}	ultimate strength
σ_{y}	yield stress
τ	interval between 90°pulse and refocusing pulse
τ_{CP}	interval between refocusing pulses in Carr-Purcell T_2 measurement
τ_{c}	correlation time
ω_0	Larmor frequency

LIST OF ORIGINAL PUBLICATIONS

This thesis is based on the following original articles referred to by their Roman numerals:

I Lammentausta E., Kiviranta P., Nissi M.J., Laasanen M.S., Kiviranta I., Nieminen M.T. and Jurvelin J.S., T2 Relaxation Time and delayed Gadolinium-Enhanced MRI of cartilage (dGEMRIC) of human patellar cartilage at 1.5 T and 9.4 T: correlation with tissue mechanical properties, *Journal of Orthopaedic Research* 24(3):366-374 (2006); doi 10.1002/jor.20041

II Lammentausta E., Hakulinen M.A., Kiviranta I., Jurvelin J.S. and Nieminen M.T., Prediction of the mechanical properties of trabecular bone with quantitative MRI, *Physics in Medicine and Biology* 51:6187-6198 (2006); doi 10.1088/0031-9155/51/23/017

III Lammentausta E., Kiviranta P., Töyräs J., Hyttinen M.M., Kiviranta I., Nieminen M.T. and Jurvelin J.S., Quantitative MRI of parallel changes of articular cartilage and trabecular bone changes in degeneration, *Osteoarthritis and Cartilage*, in press (2007); doi:10.1016/j.joca.2007.03.019

IV Lammentausta E., Silvast T.S., Närväinen J., Jurvelin J.S., Nieminen M.T. and Gröhn O.H.J., T_2, Carr-Purcell T_2 and $T_{1\rho}$ of fat and water as surrogate markers for trabecular bone structure, submitted (2007)

The original articles have been reproduced with permission of the copyright holders. The thesis also contains previously unpublished data.

CHAPTER I
Introduction

A joint is a complex structure with several interacting components. During locomotion, the joint has to sustain momentary loads many times greater than the body weight [134]. Articular cartilage is an aneural and avascular tissue that covers the ends of articulating bones in diarthrodial joints, and its main functions are to optimally distribute joint loading to the underlying bone and to provide nearly frictionless movement of the articulating bones. The mechanical properties of articular cartilage are a unique result of the interaction of the main constituents, namely collagen network, proteoglycans and interstitial water [132]. Bones provide supporting skeletal framework necessary for locomotion and protection of organs. Trabecular bone is a three-dimensional network consisting of rod-like and plate-like trabeculae, and its functions are to dampen impact loads and to house the bone marrow that produces hematopoietic cells. The mechanical properties of trabecular bone can be attributed to the structure of the trabecular network and the mechanical properties of the individual trabeculae, and are affected by the marrow flow at high strain rates [183].

Osteoarthritis (OA) is the most common degenerative joint disease, causing pain and loss of joint function to the patients and posing a high economical burden to society [1]. The degeneration process includes disruption of the collagen network, loss of proteoglycans and thickening of the subchondral bone, i.e. sclerosis [24]. Due to the aneural nature of cartilage, the first signs of pain only appear after significant degeneration has occurred. The functionality of the joint is also impaired, and eventually OA may lead to complete loss of the articular cartilage and thickening of the underlying subchondral bone, acting as an articulating surface.

Due to the symptomless progression at the first stages, there is no consensus about the sequence of the first degenerative steps. The treatment of advanced osteoarthritis is based on pain relief. At present, it is not possible to restore the degenerated tissue to its original state, and if the pain is sufficiently severe, the only option is joint replacement surgery. Thus the detection of the early stages of osteoarthritis is essential if one wishes to prevent the complete loss of cartilage and to understand the progression of disease. Current diagnostic techniques rely on joint space narrowing (JSN) and the formation of osteophytes as assessed from X-ray radiographs and arthroscopy [87]. Problematically, they are able to distinguish only severe changes in cartilage integrity and thickness.

Osteoporosis (OP) is a metabolic disorder leading to brittleness of the trabecular network and increased fracture risk [83]. The current gold standard of OP classifica-

tion is bone mineral density measured with dual-energy X-ray absorptiometry (DXA). The structure of trabecular bone can be assessed from computed tomography (CT) images but the resolution of the current in vivo scanners is insufficient to visualize the individual trabeculae. DXA provides two-dimensional projection images neglecting the thickness of bones, which may lead to significant uncertainties to the measurement. Three-dimensional, volumetric bone mineral density can be measured reliably with computed tomography [29]. However, even the volumetric density does not provide accurate information of the quality of the trabeculae.

Recent advances in quantitative magnetic resonance imaging (MRI) techniques have enabled the non-invasive evaluation of both articular cartilage and trabecular bone [42, 195]. MRI parameters have been shown to provide information about the structure of cartilage and bone [42, 195], and even serve as surrogate markers for their mechanical properties [139]. Unlike X-ray radiography or CT, MRI techniques do not utilize ionizing radiation. MRI techniques also enable the evaluation of both bone and cartilage during the same session.

In the present study, quantitative MRI and MR spectroscopy (MRS) techniques were developed and tested to assess the structure and mechanical properties of articular cartilage and trabecular bone. MRI parameters measured at 1.5 T for cartilage and bone and at 9.4 T for cartilage were correlated to mechanical and histological properties of cartilage and bone and bone mineral density and trabecular structure measured by peripheral quantitative computed tomography (pQCT). In addition, MRS parameters of trabecular bone measured at 4.7 T were correlated to the structural parameters measured with microCT. The main aims of the present study were to validate the feasibility of the methods developed earlier at high field strength to assess the mechanical properties of healthy and degenerated tissue at clinically applicable field strength and to introduce spectroscopic methods to assess the structure of healthy trabecular bone.

CHAPTER II

Structure and composition of articular cartilage and trabecular bone

2.1 Articular cartilage

Articular cartilage is an avascular and aneural highly specialized tissue. Its unique structure provides nearly frictionless movement of articulating surfaces in joint and evenly distributes loads to the underlying bone. Articular cartilage covers the articulating surfaces in diarthrodial joints, i.e. joints that are enclosed in a fibrous capsule. The inner surface of the capsule is lined with synovium, which secretes synovial fluid [134]. The constituents of cartilage form two distinct phases, the solid phase and the fluid phase [132]. The solid phase, known as the extracellular matrix (ECM), includes collagen fibers, proteoglycans and chondrocytes. The fluid phase includes interstitial water and solutes, such as nutrients and ions.

2.1.1 Collagen network

Collagen constitutes approximately 15-22% of cartilage wet weight [134]. The collagen network in articular cartilage mainly consists of type II collagen, but types III, IX, X and XI and other minor collagens are also present [51, 44]. Collagen forms fibers whose orientation is related to loading stresses placed on cartilage [134]. According to the orientation of collagen fibers, three layers can be identified in mature articular cartilage (Figure 2.1) [132]. In the superficial zone, collagen fibers are oriented in parallel to the cartilage surface. In the transitional zone, the collagen orientation is more random curving towards the radial zone, where the main orientation of collagen fibers is perpendicular to the cartilage surface. Collagen fibers in the radial zone are anchored to the subchondral bone through the tidemark and calcified cartilage [133]. The superficial zone covers approximately 5-15%, transitional zone approximately 1-15% and radial zone approximately 70-90% of total thickness of human cartilage [12]. The collagen content decreases from the articular surface towards the deep cartilage [189].

2.1.2 Proteoglycans

Proteoglycans (PG) constitute approximately 4-7% of cartilage wet weight [134]. Large PG aggrecans are composed of glycosaminoglycan (GAG) molecules covalently linked to a protein core (mostly chondroitin-4-sulfate and chondroitin-6-sulfate) [78]. These

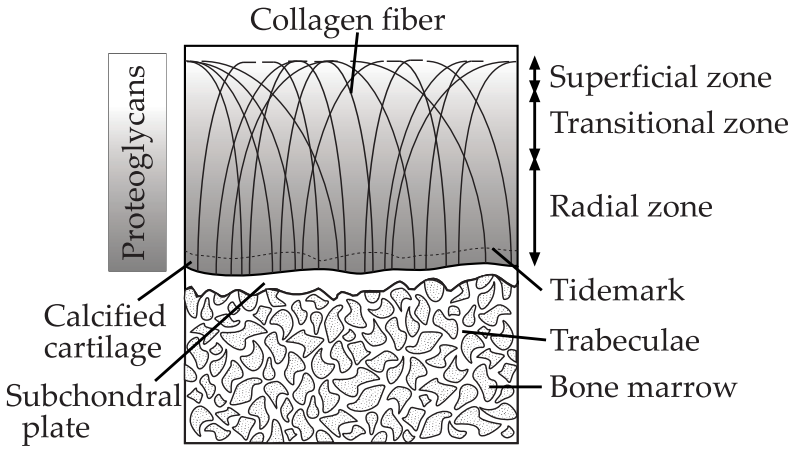

Figure 2.1: Schematic presentation of the structure of articular cartilage and trabecular bone.

aggrecans form huge composites of up to 100-200 aggrecan molecules linked noncovalently to hyaluronic acid. There is a negative charge associated with PGs which attracts cations, which in turn attract water molecules increasing the tendency of the tissue to swell [51]. Because PGs are immobilized in ECM, they give rise to high density of negative charges known as the fixed charge density (FCD) [118]. The PG content increases towards deep cartilage (Figure 2.1) [120, 92]. GAG side chains of PGs form also electrostatic bonds with collagen fibers yielding a cross-linked framework that resists tensile forces [51].

2.1.3 Chondrocytes

Chondrocytes are cells surrounded by the ECM. They synthesize type II collagen, PGs and chondronectin, a molecule that ensures contact between cells and the extracellular matrix [78]. Chondrocytes near the cartilage surface have an oval shape, while those in deeper cartilage are round [136]. The number of chondrocytes is largest in superficial tissue, while the most active chondrocytes can be found in the deep cartilage [34]. Even though chondrocytes are capable of synthesizing molecules for ECM maintenance, they are not able to repair severe damage in mature cartilage [134].

2.1.4 Interstitial water

The interstitial fluid constitutes 60-85% of cartilage wet weight [134]. A small percentage of this fluid is present in chondrocytes, about 30% is located within collagen fibers, but the majority is associated with PGs as a solute [135]. This interstitial water entrapped in tissue is exchangeable [121]. Since cartilage is avascular, nutrients and oxygen must diffuse from synovial fluid through the interstitial water of the matrix and this sets a limit on the permissable cartilage thickness [51]. The water content of cartilage decreases towards deeper tissue [103, 189]. The amount of water in tissue is controlled by the PG concentration and the subsequent swelling pressure, the organization of the collagen network and the mechanical strength of ECM [135].

2.2 Trabecular bone

Bones provide a skeletal framework that protects important organs, provides support to the body and enable mobility of the locomotive system. This is possible because of the calcified ECM, a unique feature that separates bone from other connective tissues. Bone acts also as a reservoir for several minerals, for example 99% of calcium in the body is stored in hydroxyapatite crystals [51].

Bone consists of an organic and inorganic phase. The main constituent of the organic phase is type I collagen (80-90%) embedded in a GAG gel. The inorganic phase consists mainly of hydroxyapatite ($Ca_{10}(PO_4)_6(OH)_2$) crystals and amorphous calcium phosphate. Inorganic crystals are arranged along the collagen fibers and are surrounded by amorphous ground substance [178].

Three types of cells can be found in the bone matrix [51]. Osteoblasts are cells that synthesize organic constituents of the bone matrix. When osteoblasts become trapped inside the bone matrix they maturate to form osteocytes. Osteoclasts are huge multinuclear cells that induce selective bone resorption. Although bone is one of the hardest tissues in the body, it constantly changes shape in relation to loading conditions due to remodeling by osteoblasts and osteoclasts.

Trabecular bone is a three-dimensional structure of trabecular plates and rods filled with bone marrow (Figure 2.1). It can be found in the inner parts of bone surrounded by a protecting and supporting layer of dense cortical bone. The shape of trabecular bone is constantly altered due to remodeling [51]. There are two types of bone marrow: red marrow, where blood cells are formed, and yellow marrow. The red marrow contains 40% fat and 60% hematopoietic cells, whereas yellow marrow consists of 95% fat [188].

2.3 Osteoarthritis and osteoporosis

Osteoarthritis (OA) is the most common degenerative joint disease. Twelve percent of the U.S. population aged 25 or older have OA and this percentage is predicted to increase [1]. In Finland, 5% of population aged 30 or older and 20% of population aged 75 or older have hip OA [7]. OA usually develops at older age [94] but it may as well develop as a consequence of rapidly applied excessive load [152]. OA occurs more frequently in the foot, knee, hip, spine and hand joints but it can occur in any synovial joint [24]. In addition to congenital factors, loading conditions of joints are considered to affect the development of OA [151, 134].

The first stage of OA involves PG depletion and fibrillation of collagen network which allows excessive swelling of the remaining PGs [24, 119]. The elastic modulus of cartilage decreases as the superficial cartilage wears out and the tissue may be more vulnerable to subsequent damage [174]. During the second stage, chondrocytes are stimulated to synthesize matrix macromolecules. Clusters of cells surrounded by newly synthesized matrix are formed due to chondrocyte proliferation. This stage may last for years, and in some patients it may slow down or even reverse the degeneration, at least temporarily [24].

Should the chondrocyte activity fail to stop the degeneration, then the third stage of OA occurs. This involves a progressive loss of articular cartilage and accompanying changes in the underlying trabecular bone [24]. The matrix is further damaged, and

death of chondrocytes without protection and instabilization of the matrix will occur. An increase in the density of the subchondral bone [17] and formation of cyst-like cavities that might further accelerate cartilage degeneration will occur in trabecular bone [67]. At the end stage of OA, the articular cartilage is completely lost, leaving the thickened dense subchondral plate functioning as the articular surface. Joint function is impaired, and bone remodeling combined with the loss of cartilage reshape the joint and this can even lead to shortening of the limb [24].

Typically, the changes in articular cartilage and subchondral bone are accompanied by formation of osteophytes [24]. Osteophytes are osteo-cartilaginous prominences that appear at the osteoarthritic articular surface, most commonly at the joint margins [74, 53]. Each joint has a characteristic pattern of osteophyte formation, and osteophytes may restrict joint motion and contribute to pain during motion [24].

Unfortunately, the early stages of OA are painless due to the aneural structure of articular cartilage, and it is the loss of cartilage that leads to symptoms of OA, pain and loss of joint function. Determining JSN from radiographs is utilized as a diagnostic technique but it has been shown that factors other than cartilage wearing, such as the placement of the menisci, may significantly affect the process [73]. It has been shown that the presence of definite osteophytes correlates strongly with joint pain and is an accurate method of defining OA but does not provide the best estimate of the severity of OA [176]. Clearly, markers of first, painless degenerative changes are urgently needed.

The internationally agreed description of osteoporosis (OP) is "a systemic skeletal disease characterized by low bone mass and microarchitectural deterioration of bone tissue, with a consequent increase in bone fragility and susceptibility to fractures" [4]. Osteoporosis can occur as a result of disuse but also can be detected in otherwise healthy subjects, particularly postmenopausal women [178]. Estrogen binds to specific receptors on osteoclasts activating the matrix secretion. When estrogen secretion drops markedly, the osteoclastic activity is greater than bone deposition, which may lead to a reduction of bone mass and an increase of fracture risk [51].

The current gold standard on OP diagnostics is BMD measured by DXA [83]. DXA, however, provides areal BMD but neglects the third dimension of bone so that it is possible that bone specimens with similar mineral density but different thicknesses will give different BMDs by DXA. Additionally, the accuracy of DXA alone is inadequate for evaluation of the fracture risk of an individual [82]. Quantitative CT (QCT) methods assess volumetric BMD, eliminating this source of uncertainty. In addition, CT measurements have been used to determine structural variables of trabecular bone, involving thickness and the number of individual trabeculae and volumetric fraction of trabecular bone, in order to assess the mechanical properties [76, 187].

CHAPTER III

Mechanical properties of articular cartilage and trabecular bone

3.1 Articular cartilage

The most challenging task undertaken by articular cartilage is, in addition to lubrication of contact surfaces in joint, to distribute loads to the underlying bone. The mechanical properties of articular cartilage arise from the interaction of its constituents, mainly PGs, collagen network and interstitial water. The ability of PGs to bind water allows them to swell, and the collagen network restricts this swelling to immobilize PGs, thereby inducing initial swelling pressure [132]. This endows on the tissue the ability to resist compressive loads. Collagen fibers are also prestressed by the swelling pressure of PGs which helps the collagen network to resist compressive stresses and the deformation of the matrix induced by joint loading. PGs and collagen contribute mutually to each others' mechanical properties, creating a composite material. This is analogous to the concept of steel-reinforced concrete. The matrix is further stabilized by additive specific molecule-to-molecule links between PGs and collagen network.

When a mechanical load is applied to cartilage, the pressure in cartilage matrix increases and interstitial fluid begins to flow to minimize the pressure gradients in the tissue. After releasing the load, the PGs expand causing the pressure gradient to reverse direction. PGs are considered to be primarily responsible for the equilibrium compressive stiffness, the collagen network accounts for the tensile and shear stiffness, and water for the transient viscoelastic creep and stress-relaxation behavior [132, 8].

3.1.1 Measurement schemes

Mechanical properties can be investigated by applying different loading schemes to cartilage and monitoring its deformation. There are three major geometries utilized in mechanical testing of cartilage (Figure 3.1). In unconfined compression, the cylindrical cartilage sample is isolated from subchondral bone and the load is applied by compressing the sample between two metallic platens with smooth impervious parallel surfaces. The sample is allowed to expand in the lateral direction and fluid flow is not restricted. In confined compression, the sample is inserted in a confining chamber that prevents lateral expansion, and loaded with a permeable piston to allow fluid flow in the axial direction. Indentation is a suitable geometry for *in situ* measure-

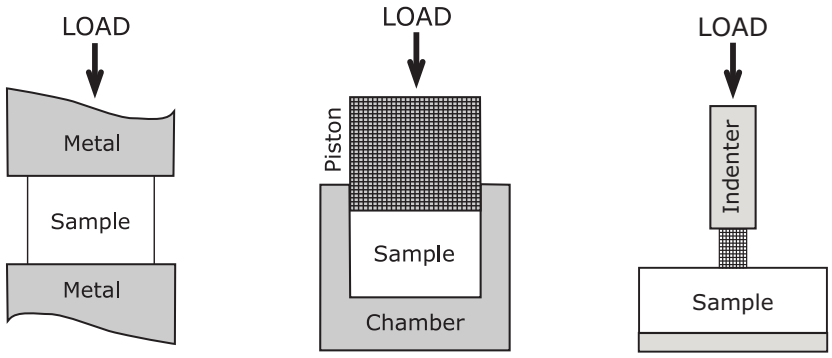

Figure 3.1: Schematic drawing of different measurement geometries for articular cartilage: unconfined compression (left), confined compression (center) and indentation (right).

ments. The intact or isolated cartilage sample still attached to subchondral bone is loaded with a permeable or impervious indenter aligned at the perpendicular to the cartilage surface. Usually the indenter is plane- or spherical-headed.

Three different loading schemes can be applied with all three loading geometries. In the stress-relaxation test, one or more compressive steps are applied and the force is measured as a function of time during the relaxation period. The creep test is performed by keeping the stress applied on the sample constant and recording the displacement of the tissue surface. In the dynamic test, several sinusoidal loading cycles are applied at a certain frequency and stress or strain amplitude.

3.1.2 Mechanical parameters

Different analytical and numerical models have been developed to characterize the mechanical properties of articular cartilage. To find an analytical solution, the structure of cartilage has to be simplified. The most popular models are the elastic single phasic model [69], viscoelastic model [147] and biphasic model [133]. Recently developed models provide accurate predictions of more complex structure, such as the triphasic model [99], the fibril-reinforced biphasic model [175, 95] and models considering the mechanical properties of cells [71].

For elastic material, Young's modulus can be written as [91]:

$$E_{\mathrm{s}} = \frac{\sigma}{\epsilon} \tag{3.1}$$

where σ is stress applied to material and ϵ is the strain induced by σ. This is commonly known as a generalization of Hooke's law. For indentation geometry, Young's modulus is provided by a modification of (3.1) [69]:

$$E_{\mathrm{s}} = \frac{\sigma}{\epsilon}\frac{\pi a_c(1-\nu^2)}{2h\kappa}, \tag{3.2}$$

where a_c is the contact radius of a plane-ended indenter, ν is Poisson's ratio, h is cartilage thickness and κ is a theoretical scaling factor which is a function of a_c/h and

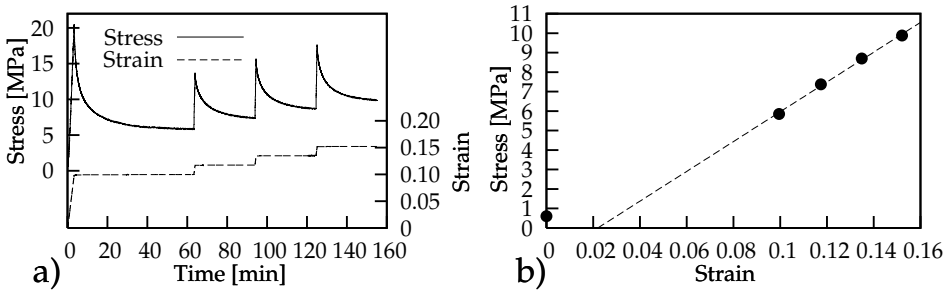

Figure 3.2: Determination of Young's modulus. From stress-relaxation test (a), stress-strain plot (b) is drawn and Young's modulus is calculated as a slope of the fitted line. the first point at zero strain is usually omitted to eliminate a possible error due to partial contact between the sample and the metal platens.

ν accounting for the finite and variable sample size [69]. Typically, Young's modulus is determined as a slope of the stress-strain plot generated from multiple consecutive stress-relaxation steps (Figure 3.2). For confined compression geometry, aggregate modulus indicates the stress-strain ratio. The relationship between Young's modulus and aggregate modulus in isotropic elastic material is controlled by Poisson's ratio of the tissue [80]:

$$H_a = \frac{(1-\nu)}{(1+\nu)(1-2\nu)} E_{\mathrm{s}} \tag{3.3}$$

Poisson's ratio is defined as the ratio of lateral and axial strains [91].

Dynamic modulus is determined to be the response of articular cartilage to cyclic loading or deformation at a particular frequency [68]. The dynamic modulus is complex in nature:

$$E_{\mathrm{d}} = E_1 + iE_2, \tag{3.4}$$

where E_1 is the storage modulus that is proportional to energy elastically stored in tissue, and E_2 is the loss modulus that describes the viscous energy dissipated in the loading process. Typically, the absolute value of the dynamic modulus is written as

$$E_{\mathrm{d}} = \sqrt{E_1^2 + E_2^2} = \frac{\sigma_{\mathrm{d}}}{\epsilon}, \tag{3.5}$$

where σ_{d} is dynamic stress. Due to the viscoelastic and instantaneously incompressible nature of cartilage, the dynamic modulus is typically several times the Young's modulus [27].

3.2 Trabecular bone

The composition and true tissue density as well as microscopic material properties are similar in trabeculae and cortical bone tissue [32]. The trabeculae which possess a specific stiffness, form a structure with its own structural stiffness [185]. The fragility of trabecular bone depends not only on the thickness and organization of the trabeculae [183] but also on the quality of the trabecular network, i.e. the mineral density

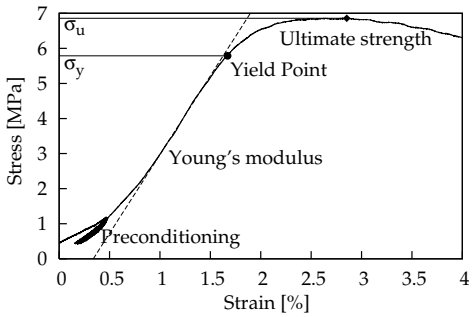

Figure 3.3: Determination of the mechanical properties of trabecular bone by applying a compressive test. Young's modulus is determined as slope of the linear elastic region and yield point is the starting point of the plastic region. Ultimate strength is the maximum stress.

[184] and collagen structure [25]. Viscous flow of bone marrow through pores in the trabecular structure contributes to the mechanical properties at high strain rates by increasing the strength, modulus and energy absorption of trabecular bone [32].

3.2.1 Measurement schemes

Cylindrical samples are typically used for mechanical testing of trabecular bone. Methods for compressive, tensile, bending and torsion testing have been developed to determine parameters describing loading behavior of trabecular bone [185]. All these tests are destructive in nature, since the aim is to break the trabecular structure. Compression is the most typical technique because relatively small samples can be used. It may be less accurate than the tensile test because of the sample end effects, i.e. the elevated strains in the trabeculae near metal platens and shear stresses caused by inadequately levelled sample ends. Ideally, the ratio between length and diameter of a sample in a compressive test is 3:1 or more. The definite advantage of compressive testing is its similarity to the natural loading conditions in many regions of the skeleton, e.g. in the vertebrae [185].

3.2.2 Mechanical parameters

The stress-strain curve of compressive testing of bone is divided into an elastic and plastic region. In the elastic region, deformations will recover once the loading is released, whereas in the plastic region deformations are irreversible. Young's modulus of trabecular bone is determined from the elastic region of the stress-strain curve (Figure 3.3). The most linear part of the curve is usually located between 40 and 65 percent of the maximum stress [106], and Young's modulus is calculated as the slope of the line fitted into the stress-strain data of this region [183]. The yield point is determined as the starting point of the plastic region. A good estimate for the yield point is to determine the intersection of the stress-strain curve and the linear fit used in the determination of Young's modulus with a 0.03% strain offset [185]. The yield stress σ_y is determined as the stress at yield point, and the ultimate stress σ_u as the maximum stress of the stress-strain curve.

CHAPTER IV

Quantitative NMR methods for articular cartilage and trabecular bone

The following is a summary of the concepts essential to understand the NMR relaxation in tissue, based on [64, 49]. The theory of NMR relaxation is presented in rich details in many textbooks [64, 49, 22, 36].

4.1 ^{1}H nuclear magnetic resonance

Every nucleus possesses an quantized intrinsic property called spin s or, more precisely, nuclear spin angular momentum. It can be visualized as a spinning motion of the nucleus about its own axis, forming a small magnetic field along the axis of spinning. The spin of a nucleus is nonzero when the nucleus has an odd atomic mass number A (odd number of protons Z and even number of neutrons N or vice versa) [200]. Nuclei with nonzero spin can experience nuclear magnetic resonance (NMR). When placed in an external magnetic field B_0, the spins of nuclei line up along the external field. The alignment, however, is not complete, and spins precess around the magnetic field line with angular frequency called the Larmor frequency:

$$\omega_0 = \gamma B_0, \tag{4.1}$$

where γ is the gyromagnetic ratio of the nucleus in question. This is analogous to the rotating gyroscope precessing around the axis of gravity.

Related to its spin, a nucleus can have $2s$+1 energy states:

$$E = -m_s \gamma \hbar B_0 = -m_s \hbar \omega_0, \tag{4.2}$$

where $m_s = -s, -s+1, ..., s-1, s$, and $\hbar$ is the Dirac's constant. Nuclei with $s = 1/2$ are the most favourable nuclei for NMR techniques because they have two distinct energy states and thus only one quantized energy describing the transition between these states. The spin of the hydrogen nucleus (^{1}H) is $1/2$, and this together with its natural abundance in tissues makes it the preferred nucleus for biological and medical NMR applications.

Due to thermal energy of the spins, the number of the nuclei in different energy states obeys Boltzmann's statistics. For $s = 1/2$ nuclei, the energy difference between the two quantum spin states is $\hbar\omega_0$, and there is a small excess of spins at the lower energy state, i.e. the spin aligned parallel to the B_0 ($m_s = -1/2$), compared to the

higher energy state, i.e. the spins aligned anti-parallel to the B_0 ($m_s = 1/2$). The number of the spins at the lower energy state exceeding the number of the spins at higher energy state is defined by

$$\frac{n_{s=-1/2}}{n_{s=+1/2}} = e^{-\Delta E/kT} = e^{-\hbar\omega_0/kT}, \tag{4.3}$$

where k is Boltzmann's constant and T is the absolute temperature. Since the energy difference between two quantum states is extremely small compared to thermal energy, the spin excess is very small. For example, for 10^{15} water molecules at 20°C temperature, the spin excess at 1.5 T is about $2{\cdot}10^4$. However, the large number of hydrogen nuclei in the tissue gives rise to the net magnetization M_0 along the B_0.

4.2 Relaxation

To generate a detectable NMR signal, the equilibrium state of the spins must be perturbed. Exact calculations of perturbation and relaxation of system of multiple spins are quantum mechanical, but a classical model of net magnetization can be applied as a model with sufficient accuracy.

Consider the external magnetic field parallel to z-axis. A radio frequency (RF) magnetic field $\vec{B}_1$ can be used to tip the net magnetization away from the direction of $\hat{z}$. The spins receive energy most efficiently from the RF field with the frequency of the Larmor frequency of the spins, i.e.

$$\vec{B}_1 = B_1(\cos\omega_0 t\hat{x} - \sin\omega_0 t\hat{y}). \tag{4.4}$$

This induces a time-dependent behavior of the net magnetization that can be characterized with

$$\frac{d\vec{M}}{dt} = \gamma\vec{M} \times \vec{B}_{\text{ext}}, \tag{4.5}$$

where $\vec{B}_{\text{ext}} = \vec{B}_0 + \vec{B}_1$. This together with (4.1) yields three components:

$$\frac{dM_x}{dt} = \gamma\left(M_y B_0 + M_z B_1 \sin\omega_0 t\right) \tag{4.6}$$

$$\frac{dM_y}{dt} = \gamma\left(M_z B_1 \cos\omega_0 t - M_x B_0\right) \tag{4.7}$$

$$\frac{dM_z}{dt} = \gamma\left(M_x B_1 \sin\omega_0 t + M_y B_1 \cos\omega_0 t\right). \tag{4.8}$$

After the perturbation, i.e. excitation of spins, the behavior of the net magnetization can be characterized with the Bloch equation:

$$\frac{d\vec{M}}{dt} = \gamma\vec{M} \times \vec{B}_{\text{ext}} + \frac{1}{T_1}\left(M_0 - M_z\right)\hat{z} - \frac{1}{T_2}\vec{M}_\perp, \tag{4.9}$$

where $\vec{B}_{\text{ext}} = B_0\hat{z}$ and $\vec{M}_\perp$ is the net magnetization in the xy plane. This yields three components of $\vec{M}(t)$:

$$M_x(t) = e^{-t/T_2}\left(M_x(0)\cos\omega_0 t + M_y(0)\sin\omega_0 t\right) \tag{4.10}$$

$$M_y(t) = e^{-t/T_2}\left(M_y(0)\cos\omega_0 t - M_x(0)\sin\omega_0 t\right) \tag{4.11}$$

$$M_z(t) = M_z(0)e^{-t/T_1} + M_0\left(1 - e^{-t/T_1}\right) \tag{4.12}$$

where T_1 and T_2 are the relaxation time constants. The relaxation processes are controlled by these constants, but other factors, such as chemical shift, quadrupole relaxation and vicinity of paramagnetic molecules, may complicate the processes.

4.2.1 T_1 relaxation

After the excitation of the spin system, energy exchange occurs between the spins and their molecular framework, or lattice, until a thermal equilibrium is reached and the z-component of net magnetization is recovered. A similar effect to the external RF field can be created by local fluctuating fields that have a time-dependent component in the xy-plane. The time-dependent component of these fluctuations is described by the correlation time τ_c. These dipole-dipole interactions arise from random molecular rotation or diffusion. The magnitude of the field inducing the fluctuations between two spins depends on their distance and direction compared to the direction of B_0. The relaxation rate $1/T_1$ of spin-lattice-relaxation is dependent on the magnitude of the fields present in the xy-plane (B_{xy}) and the correlation time of molecular motion:

$$\frac{1}{T_1} \propto B_{xy}^2 \frac{\tau_c}{1+\omega_0^2\tau_c^2}. \tag{4.13}$$

It can be seen that the relaxation is most efficient when $\omega_0\tau_c$=1. The B_{xy} field depends on the angle θ between $\vec{B}_0$ and vector joining two nuclei:

$$B_{xy} \propto \sin\theta\cos\theta \tag{4.14}$$

4.2.2 T_2 and T_2^* relaxation

After excitation of the spins, the net magnetization has a transverse component $\vec{M}_\perp$ in the xy-plane. The magnitude of the $\vec{M}_\perp$ is zero at thermal equilibrium, and its decay arises from interactions between neighboring nuclear spins. Because of the local fluctuations of magnetic field in the z-direction, the orientation of the spins will spread due to the different Larmor frequencies. This causes the magnitude of $\vec{M}_\perp$ to decay due to dephasing of the spins. The relaxation rate $1/T_2$ of spin-spin relaxation depends on the magnitude of z-direction of the fluctuating fields and of the correlation time of molecular motion:

$$\frac{1}{T_2} \propto B_z^2\tau_c. \tag{4.15}$$

T_2 relaxation time probes the components of motion with low frequencies that have no effect on T_1. However, the components that determine T_1 contribute also to T_2.

The B_z field depends on the angle θ between $\vec{B}_0$ and vector joining two nuclei:

$$B_z \propto (3\cos^2\theta - 1). \tag{4.16}$$

In a solution, the motion of the molecules causes θ to fluctuate randomly, and the dipole-dipole interaction is averaged over all orientations. This phenomenon is known as motional narrowing. In biological tissues with a highly organized structure, such as cartilage or tendon, this may significantly affect the signal intensity [43]. From (4.16) it can be seen that the minimum of dipolar interaction is achieved when θ=55°, known as the "magic angle".

Transverse dephasing of NMR signal includes contributions of static and dynamic dephasing regimes [65, 31]. The static component is caused by macroscopic field inhomogeneities caused by local variations of B_0 and varying susceptibility of the sample affect the dephasing of transverse magnetization. The effects induced by static (T_2') and dynamic (T_2) dephasing are combined into T_2^* so that

$$\frac{1}{T_2^*} = \frac{1}{T_2'} + \frac{1}{T_2}. \tag{4.17}$$

In addition to the intrinsic T_2, the dynamic dephasing of transverse magnetization is governed by diffusion of molecules in local magnetic field gradients and the exchange of molecules between sites with different resonance frequencies so that

$$\frac{1}{T_2} = \frac{1}{T_{2,\text{intr}}} + \frac{1}{T_{2,\text{diff}}} + \frac{1}{T_{2,\text{exch}}}, \tag{4.18}$$

where $T_{2,\text{intr}}$ is the intrinsic T_2 of the tissue arising from the dipolar interaction of the molecules, while $T_{2,\text{diff}}$ and $T_{2,\text{exch}}$ are the contributions of diffusion and exchange of molecules to measured T_2, respectively. $T_{2,\text{diff}}$ can be written as:

$$\frac{1}{T_{2,\text{diff}}} = \frac{n}{12} G^2 \gamma^2 D(\tau)^2, \tag{4.19}$$

where n is the number of the refocusing pulses, G is the amplitude of local gradient fields, D is the diffusion coefficient and τ is the interval between the pulses [65, 31].

4.2.3 $T_{1\rho}$ relaxation

$T_{1\rho}$ relaxation time refers to relaxation in the rotating frame [169, 160, 166]. In the $T_{1\rho}$ experiment, magnetization is tilted to the xy-plane and locked by an on-resonance field $\vec{B}_{1\text{SL}}$ induced by an RF pulse. During a spin-lock pulse, the magnetization relaxes towards equilibrium defined by $\vec{B}_{1\text{SL}}$ with the relaxation constant $T_{1\rho}$. The relaxation rate $1/T_{1\rho}$ is the function of the respective correlation time τ_c

$$\frac{1}{T_{1\rho}} \propto B_{xy}^2 \frac{\tau_c}{1 + \omega_0^2 \tau_c^2}. \tag{4.20}$$

Typical $\vec{B}_{1\text{SL}}$ fields are at a magnitude of a few gauss, thus the resonance frequencies are in the kHz range. $T_{1\rho}$ takes advantage of the benefits of high B_0 field, such as the better signal to noise ratio (SNR), while providing information of the relaxation phenomena at low field strengths. The behavior of $T_{1\rho}$ may thus be similar to that of T_2. $T_{1\rho}$ dispersion, i.e. $B_{1\text{SL}}$ field dependence of $T_{1\rho}$, provides information on the frequency distribution of molecules causing fluctuations at the low end of the frequency spectrum.

4.2.4 Physiological basis of relaxation

As described above, the dipole-dipole interaction is the main source of ^{1}H NMR relaxation in tissue. Within the water molecule, the fluctuation of the local field arises from rotational dynamics of the molecule with respect to the orientation of B_0, and

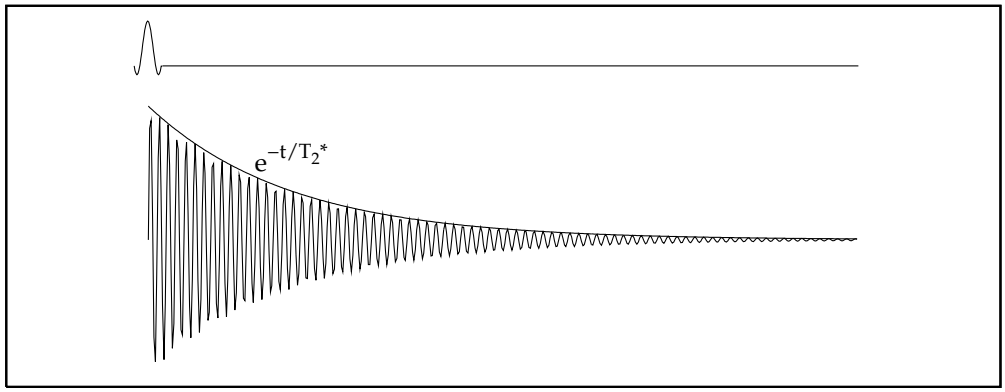

Figure 4.1: A free induction decay experiment. After a 90°pulse, the signal decays exponentially due to the dephasing of the magnetization. Both intrinsic T_2 and the field inhomogeneities contribute to the decay factor.

for hydrogen nuclei of different water molecules, the fluctuation is a function of the distance between two nuclei. The majority of water in tissue is free water. At room temperature, free water molecules have a correlation time of about $\sim 10^{-12}$ s, while tightly bound water may have a correlation time of $\sim 10^{-3}$ s [23]. The magnetic field corresponding to the Larmor frequency of the free water is unattainably high, and for commonly used field strengths, the contribution of free water to relaxation is independent of resonance frequency. Although free water spends less than 2% of its time in contact with macromolecules, its relaxation properties are significantly affected by these interactions [93]. The relaxation due to water molecules interacting with macromolecules makes a major contribution to the water molecule exchange between free water and protein in specific sites, hydrogen exchange between water and protein ionizable groups and transient collisions of water and macromolecules [23]. These processes slow the rotational motion of the water molecules and generate relaxation in the tissue [93].

At low values of B_0, T_1 and T_2 are similar. At increasing field strengths ($\gtrsim$ 0.5 T), both T_1 and T_2 increase remarkably, but T_1 has greater field dependence [93]. Dynamic dipole-dipole interactions caused by rapid molecular motions around the Larmor frequency contribute to both T_1 and T_2. The slower motions of the system which consists of water and macromolecules are in the frequency range affecting T_2. There are always slow macromolecular motions present in biological tissues, contributing only to the correlation time related to T_2, and consequently $T_2 \leq T_1$. Thus, T_2 is sensitive to mobility and the size of the surrounding molecules. These slow motions are also essential for $T_{1\rho}$ relaxation. In addition to Brownian motion, the mobility of molecules depends on temperature and pH [23].

4.2.5 Measurement of relaxation times

The simplest NMR experiment is a free induction decay (FID) experiment. The net magnetization is tilted 90° to the xy-plane with an RF pulse. Subsequently, the preces-

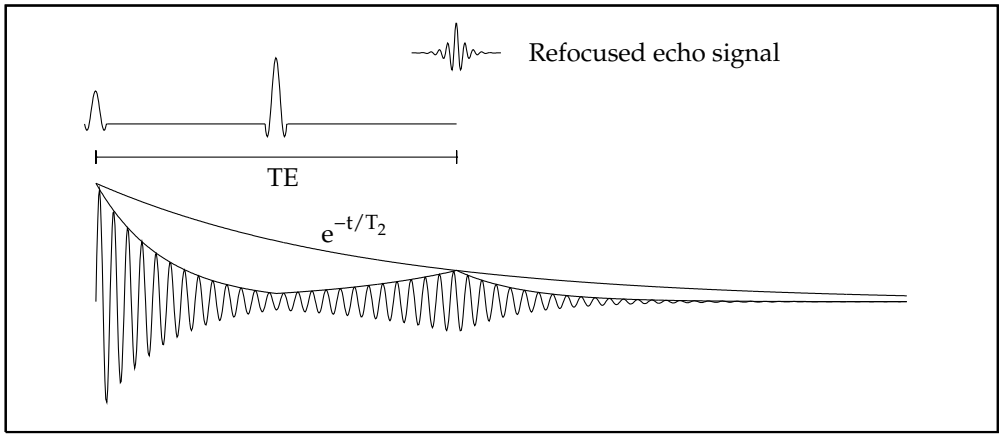

Figure 4.2: Spin echo experiment. The decay due to field inhomogeneities can be recovered but the intrinsic T_2 decay causes the echo signal to be weaker than the original FID. The maximum of the refocused echo signal and thus the time of data acquisition is denoted with a waveform.

sion of spins induce an electromotive force in RF coils near the sample. Under ideal circumstances, the decay of the FID signal amplitude is proportional to e^{-t/T_2}. Because of the nonuniformities in the receiving coil and sample, the Larmor frequency of the sample tends to be a distribution of frequencies instead of a single frequency. As a consequence, dephasing of the net magnetization in the xy-plane causes the FID to decay faster, proportionally to e^{-t/T_2^*} (Figure 4.1). It is possible to eliminate this additional decay. By reversing the phasing of the spins in the transverse plane by applying a 180° RF pulse at time τ after the 90° pulse, a refocused echo builds at time 2τ after the 90° pulse (Figure 4.2). Dephasing due to inhomogeneities is cancelled, but because of the dephasing due to transverse relaxation in tissue, the magnitude of the refocused echo is smaller than the maximum amplitude of FID by the factor e^{-t/T_2}. This is called the spin echo technique, and the time 2τ is called the echo time (TE). By performing several spin echo measurements with different TE's, a magnetization profile can be obtained, and T_2 can be determined by fitting data into the relaxation equation:

$$M_\perp(t) = M_{\perp,0} e^{-\mathrm{TE}/T_2}. \tag{4.21}$$

where $M_{\perp,0}$ is the transverse net magnetization immediately after the 90° pulse.

The dephasing of transverse relaxation due to diffusion of the molecules cannot be recovered in the spin echo experiment. The refocusing of the magnetization is incomplete because of random transport of molecules during the experiment from one location to another with different field inhomogeneities. To suppress the diffusion effect, a series of 180° pulses can be inserted after the 90° pulse (the Carr-Purcell method). The purpose is to prevent the phase accumulation of the diffusing spin by refocusing the magnetization. For example, when four refocusing pulses are applied, the first pulse is inserted at time period τ after the 90° pulse, and the following pulses are inserted at times 3τ, 5τ and 7τ. The echoes will thus occur at 2τ (=TE_1), 4τ (=$2\mathrm{TE}_1$),

6τ (=3TE$_1$) and 8τ (=4TE$_1$) (Figure 4.3). By applying a different number of refocusing pulses at constant intervals, a magnetization profile is obtained and Carr-Purcell-T_2 (CP-T_2) with diffusion compensation can be determined using Equation (4.21).

The effect of field inhomogeneities is cancelled by the refocusing RF pulse. However, the FID signal can be refocused without cancelling T_2' effects by generating a gradient echo (Figure 4.4). The first gradient pulse dephases the magnetization proportionally to its time integral, and second gradient pulse, inserted at opposite direction, rephases the magnetization. The maximum rephasing occurs when the time integral of the first gradient is fully reversed. The decay equation is analogous to (4.21):

$$M_\perp(t) = M_{\perp,0} e^{-\mathrm{TE}/T_2^*}. \tag{4.22}$$

T_1 relaxation time is usually determined using inversion recovery sequence (Figure 4.5). The longitudinal magnetization is inverted with a 180° RF pulse, followed by a 90° excitation pulse after the inversion time (TI). According to (4.12), the time-dependent evolution of longitudinal magnetization obeys

$$M_z(t) = M_0(1 - 2Se^{-\mathrm{TI}/T_1}), \tag{4.23}$$

and by applying multiple TI's, the T_1 can be solved. The inversion recovery experiment is similar to the FID experiment with an additional 180° pulse, and refocusing pulses can be applied to obtain the echo for data acquisition. The factor S depends on the accuracy of the 180° pulse, and ideally S=1.

Repeated spin echo sequence can also be used for T_1 determination. This is called the saturation recovery technique. The longitudinal magnetization recovers as a function of the interval between consecutive acquisitions, i.e. the repetition time (TR). By varying TR, T_1 can be solved from

$$M_z(t) = M_0\left(1 - Se^{-\mathrm{TR}/T_1}\right). \tag{4.24}$$

$T_{1\rho}$ relaxation time at certain B_{1SL} field strength is determined by varying the duration of the spin-lock pulse (TSL). After the spin-lock preparation, the FID signal can be collected with any standard sequence. The decay is described by the exponential equation

$$M = M_0 e^{-\mathrm{TSL}/T_{1\rho}}. \tag{4.25}$$

While measuring $T_{1\rho}$, the so-called adiabatic condition must be fulfilled. In other words, $B_{1\mathrm{SL}}$ fields must be chosen so that the magnetization is able to follow the spin-lock field, i.e. the τ_c related to $T_{1\rho}$ relaxation is close enough to $1/\gamma B_1$. When the adiabatic condition is violated, rapid dephasing occurs causing apparent shortening of measured $T_{1\rho}$. A significant technical problem in the $T_{1\rho}$ determination lies in the high specific absorption rate (SAR) values, indicating the absorption of energy to the tissue, due to the spin-lock pulses.

4.3 Diffusion

Diffusion is Brownian motion, or random transport, of the water molecules in the tissue. The magnetic field experienced by nuclei change rapidly from location to another, and thus the refocusing of the spins is not complete after the 180° pulse,

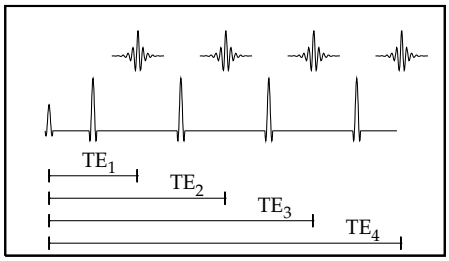

Figure 4.3: Determining T_2 (or CP-T_2) with Carr-Purcell method. The number of the refocusing pulses can be varied.

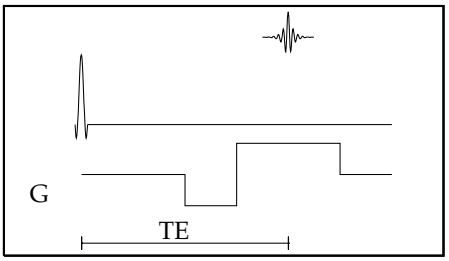

Figure 4.4: Gradient echo sequence. The first negative gradient dephases and second gradient rephases the signal.

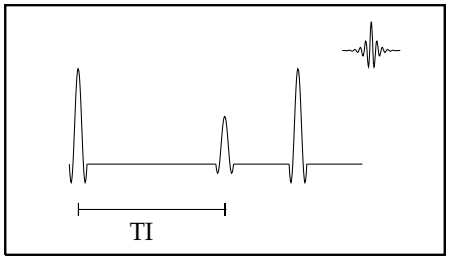

Figure 4.5: Inversion recovery sequence.

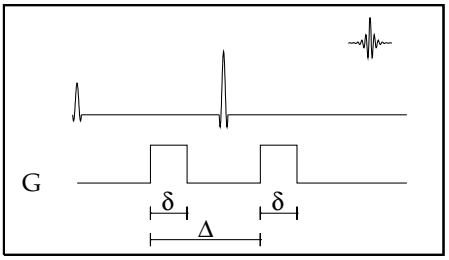

Figure 4.6: Spin echo sequence with diffusion encoding gradients.

and signal loss is observed. The suppression of the dephasing caused by diffusion is described above. The dephasing of transverse magnetization due to diffusion of molecules can be determined by applying additional diffusion encoding gradient pulses (Figure 4.6). If the spin remains at the same location, the dephasing caused by the first gradient pulse will be fully cancelled by the second gradient pulse. If diffusion occurs, then the spins will experience different field strengths as compared to the situation after the first pulse, and rephasing will be incomplete. The decay of the magnetization depends on the strength and duration of the gradients and the diffusion time

$$M = M_0 e^{-bD,}, \quad \text{where} \tag{4.26}$$

$$b = \gamma^2 G^2 (\Delta - \delta/3), \tag{4.27}$$

D is the diffusion coefficient, G and δ are the amplitude and duration of the diffusion gradients, respectively, and Δ is the time difference between the leading edges of these pulses. The term $(\Delta - \delta/3)$ is often referred to as the diffusion time t_D. By applying different b-values by modulating the magnitude of G, the diffusion coefficient can be solved. The diffusion coefficient can be determined in different directions by altering the direction of G.

4.4 Contrast agents

Paramagnetic contrast agents can be introduced to enhance the signal intensity. Paramagnetism of atoms and ions arises from partly filled inner electron shells of certain elements, such as transition elements, rare earth and actinide elements [91]. Free atoms and ions have the strongest paramagnetic effect, and many of the aforementioned elements exhibit paramagnetic properties even when incorporated in solids. Paramagnetic molecules have a magnetic moment many thousands times of those of hydrogen atoms. Thus they produce higher local fields and enhance the relaxation rate of the hydrogen atoms in water molecules bound to them. The continuous water exchange between free and bound water enables the contrast agent to enhance the relaxation throughout all of the water [162].

The relaxation rate is directly proportional to the concentration of the contrast agent (C):

$$R_1(C) = \frac{1}{T_1(C)} = \frac{1}{T_{1,0}} + \alpha_1 C \tag{4.28}$$

where α_1 is called the T_1 relaxivity [(mmol/l)$^{-1}$sec^{-1}], a property specific to the composition of the contrast agent and tissue in question. $T_1(C)$ and $T_{1,0}$ are the T_1 relaxation times in the presence and absence of contrast agent, respectively. The decrease of T_2 relaxation time follows similar behavior [162]. The correlation time of the contrast agent depends on the rotational correlation time, the exchange lifetime of water molecule in the complex and the electron relaxation time [104], thus different contrast agents affect T_1 and T_2 differently. The most important paramagnetic ions are gadolinium (Gd^{3+}), iron (Fe^{2+}), manganese (Mn^{2+} and Mn^{3+}) and chromium (Cr^{2+}). The contrast agents used in NMR studies consist of paramagnetic ions embedded in chelates. For example, gadolinium is often embedded in diethylenetriaminepentaacetic acid (DTPA)[162].

4.5 Imaging and spectroscopy

In order to obtain spatially encoded information of the sample under investigation, the slice selection and frequency- and phase-encoding gradients are applied. The collected FID data, known as the k-space is converted into a magnitude image with two-dimensional finite Fourier transform (FFT).

The different chemical environments of the hydrogen nuclei cause slight shifting in the Larmor frequencies, known as the chemical shift. The mean frequency shift between hydrogen nuclei in water and lipid is 3.35 ppm, corresponding to a Larmor frequency shift of 215 Hz at 1.5 T. By performing a one-dimensional Fourier transform to the FID, the frequency distribution of hydrogen nuclei and, thus the relative abundance of different molecules can be determined. Spectroscopic measurements can be either localized, or the magnetization of the entire sample can be examined.

4.6 MRI applications for articular cartilage

The NMR signal of articular cartilage receives its main contributions from highly organized collagen network and charged hydrophilic PG molecules, the main constituents of the ECM.

The architecture of collagen network in articular cartilage is well-defined with histological methods [12, 132]. The modulation of the NMR signal intensity in cartilage as a function of distance from surface was first suggested to be controlled by the depth-dependent water content of cartilage [102]. Later, the modulation of signal intensity was correlated to the histological layers of cartilage [130]. The relationship between the signal intensity and orientation of collagen fibrils relative to $\vec{B}_0$ field was demonstrated by imaging bovine patellae at different angles in the $\vec{B}_0$ field [164]. The greatest increase of the signal intensity was observed at an angle of 55°, i.e. the magic angle, referring to the association between T_2 contrast and collagen orientation. Later this relationship was confirmed with a correlation to quantitative microscopy [62, 203, 142]. It is suggested that although collagen itself has low water binding ability, it is able to control the orientation of the water molecules within cartilage [164]. It has also been hypothesized that PG side chains oriented to collagen fibrils [62] and water interacting with collagen fibrils [13, 101] can affect the angle-dependence of the contrast. When the articular surface is perpendicular or parallel to $\vec{B}_0$, the T_2 of the superficial zone displays short values. Towards the transitional zone, T_2 increases, and decreases again in the radial zone. When the sample is rotated, the T_2 of the transitional layer with its more random collagen orientation does not vary significantly, whereas the T_2 of superficial and radial zone varies as a function of the angle achieving a maximum at the magic angle, where the dipolar interaction (Equation 4.16) is minimized [201, 202]. The spatial variation of T_2 has also been verified *in vivo* on healthy young adults [37], but the resolution of clinical imaging devices typically prevents the observations of the superficial zone of cartilage.

The variation of T_2 has been studied in several joints on animal and human tissues. Significant relation with collagen content and T_2 has been established [47, 140]. In addition to collagen, T_2 has been shown to depend on PG [154, 193] and water [110] content of cartilage. T_2 relaxation time has been related to the mechanical properties of articular cartilage [193, 139, 143, 97], and the relationship of T_2 and cartilage degeneration has been studied with enzymatic degradation models [140, 193] and spontaneous degeneration [50, 129, 154, 143, 40]. It has also been suggested that T_2 is sensitive to degenerative changes but not to any specific component [126]. Recently, a two-component nature of T_2 of calcified and deep radial cartilage has been reported [86]. It has been suggested that the fast component is governed by orientation-dependent mechanisms, and that the slow component is virtually independent of orientation with respect to B_0. Usually, the TE's used in T_2 measurements are too long to properly display the biexponential nature of the decay curve [173].

T_1 relaxation time of cartilage is usually thought to be relatively constant at all tissue depths [128, 201], and also to be isotropic [70]. However, T_1 has been correlated with water content and degeneration of articular cartilage [123]. There might be issues considering T_1 relaxation mechanisms of articular cartilage not yet completely understood. Delayed gadolinium enhanced MRI of cartilage (dGEMRIC) [26] utilizes the T_1 relaxation time in the presence of the paramagnetic contrast agent, gadolinium, embedded in a diethylene triaminopentaacetate acid (Gd-DTPA) chelate that has a double negative charge [59]. When Gd-DTPA^{2-} diffuses into cartilage, it is assumed to distribute inversely to the negatively charged PG concentration [10, 11]. By measuring T_1 relaxation time with and without Gd-DTPA^{2-}, the spatial contrast agent

distribution can be derived from (4.28) and used as an inverse estimate of the PG distribution in the cartilage. The FCD of cartilage bathed in solution containing Gd-DTPA^{2-} can be assessed with [10]

$$\text{FCD} = 2[Na^+]_b \left(\sqrt{\frac{[\text{Gd-DTPA}^{2-}]_t}{[\text{Gd-DTPA}^{2-}]_b}} - \sqrt{\frac{[\text{Gd-DTPA}^{2-}]_b}{[\text{Gd-DTPA}^{2-}]_t}} \right), \tag{4.29}$$

where t and b refer to tissue and bath, respectively. The method has been validated with biochemical methods [10, 11]. The problem in quantization *in vivo* studies is that the Gd-DTPA^{2-} concentration of the synovial fluid acting as bath is not adequately known.

T_1 relaxation time in the presence of Gd-DTPA^{2-} (dGEMRIC) has been correlated with the mechanical properties of cartilage [139, 143, 97, 165]. Several studies have successfully related the dGEMRIC index or Gd-DTPA^{2-} content of cartilage to the PG content of cartilage as determined by histological methods[141, 143], however the method seems to occasionally overestimate the PG content in deep cartilage [141, 143]. The relationship of dGEMRIC and cartilage degeneration has been confirmed using bovine tissue *in vitro* in enzymatic digestion models [10, 141] and in specimens with spontaneous degeneration [143]. Several *in vivo* studies have been published monitoring the PG content of healthy, degenerated and engineered cartilage [179, 180, 199, 144, 204, 161, 124]. In most of these studies, the T_1 relaxation time in the absence of Gd-DTPA^{2-} has not been measured, simply assumed to be constant. A recent study has reported that there is considerable variation in T_1 without contrast agent and a significant relationship between the GAG concentration and the difference in T_1 measured in the absence and in the presence of Gd-DTPA^{2-} at 1.5 T [192]. Gd-DTPA^{2-} relaxivity has been reported to depend on the macromolecular content of tissue at 1.5 T [177] which complicates the assessment of the PG content.

$T_{1\rho}$ relaxation time of articular cartilage has been related to its PG content [41, 154, 196, 198, 197], mechanical properties [198] and cartilage degeneration [18, 155]. Significant $T_{1\rho}$ dispersion has been observed on the weight-bearing area of the femoral head [156]. It has also been suggested that $T_{1\rho}$ is not sensitive to any particular component but to general changes in the cartilage structure [126], and that the orientation-dependent dipolar interaction arising from the collagen orientation contributes to $T_{1\rho}$ [18].

Magnetization transfer (MT) is a process where two pools of spins are exchanging magnetization at a constant rate [16]. If one of the pools is saturated with RF energy, then exchange occurs until a steady state is achieved. By monitoring the magnetization of the second pool at the steady state, the ratio of magnetization transfer can be determined. In cartilage, the two pools include free water and water molecules associated with macromolecules [88]. It has been suggested that while collagen is the dominant component contributing to the MT in cartilage [88, 168] also PGs have a significant role [57], especially in case with PG depletion as a model for early degenerative changes [191]. A recent study reported that MT is not sensitive enough to be utilized as a follow-up tool for monitoring the repair of the cartilage tissue [146].

The MRI appearance of cartilage under compression has been studied. The collagen fibrils of the transitional zone have been reported to bend along the cartilage surface causing a slight increase in the thickness of superficial zone and randomiza-

tion in the fiber orientation in the radial zone [61, 2]. Enzymatic digestions have been reported to affect the mechanical properties as well as MRI appearance of cartilage under compression [163, 157, 84]. Magnetic resonance elastography is a method for determining the strains in tissue by measuring the shear waves propagating in tissue during cyclic loading [145, 66]. The weight-bearing MRI applications have also been introduced to demonstrate the load distributions *in vivo* [54, 137].

In addition to methods focusing on ^{1}H NMR, MR imaging and spectroscopy of ^{23}Na has been utilized to characterize articular cartilage [171, 18]. Changes in the PG concentration affect the ability of cartilage tissue to attract positively charged sodium ions, and thus the sodium concentration reflects the FCD [172] and the PG concentration [19] of cartilage.

4.7 MRI applications for trabecular bone

The NMR signal of bone tissue is negligible due to the calcified nature of bone. However, quantitative methods utilizing NMR-visibility of bone marrow have been developed to assess the structural and mechanical properties of trabecular bone. Lipids make a major contribution to the MR signal of trabecular bone, in both red and yellow marrow [188].

The significant susceptibility difference between trabecular bone and bone marrow gives rise to strong local inhomogeneities in the magnetic field, affecting the T_2^* relaxation time. The increase in relaxation rate is proportional to the concentration and number of susceptibility discontinuities and the magnitude of the susceptibility difference. This mechanism has been demonstrated with computer simulations [113] and experimental studies [116, 55], relating the T_2^* relaxation time to the density of trabeculae. T_2^* has been successfully related to ash density and the mechanical properties of trabecular bone [33, 75, 20]. BMD measured with DXA has been shown to correlate *in vivo* with T_2^* in calcaneus [63, 81], distal radius [56] and the proximal femur [107, 6, 5]. T_2^* has also been related to the structural parameters of trabecular bone [33, 3, 15].

The structure of three-dimensional trabecular lattice can be determined from MRI images. Structural indices, such as bone volume fraction (BV/TV), trabecular thickness (Tb.Th), trabecular separation (Tb.Sp) and trabecular number (Tb.N) are calculated from binarized images of trabeculae and bone marrow. Images with a resolution sufficient compared to size of the trabeculae can easily be binarized by determining a threshold value of the grayscale to distinguish between the two phases. The typical resolution of the clinical MR image is larger than the trabecular thickness, and additional steps need to be taken to evaluate the structural parameters of bone. The histogram of reverse grayscale image can be utilized to approximate the BV/TV of trabecular bone [114]. The mean intensity of the ROI located in trabecular bone (I_{roi}) is considered to account for the contribution of trabeculae and marrow in the following relation:

$$I_{roi} = \text{app.BV/TV} \cdot I_b + (1 - \text{app.BV/TV}) \cdot I_m, \tag{4.30}$$

where I_b and I_m are the intensities for bone and marrow, respectively, and app.BV/TV

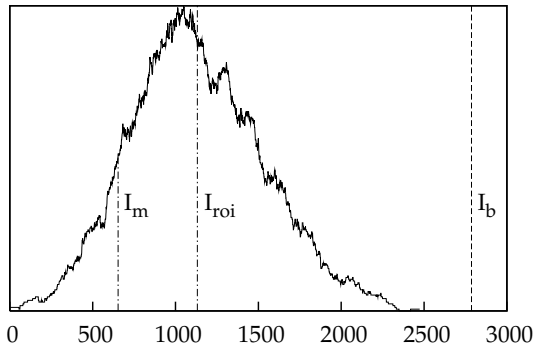

Figure 4.7: Determining the intensities essential to calculation of the apparent bone volume fraction from histogram of reversed grayscale image of region of interest.

is the apparent bone volume fraction. This yields the calculation for app.BV/TV:

$$\text{app.BV/TV} = \frac{\text{I}_{\text{roi}} - \text{I}_{\text{m}}}{\text{I}_{\text{b}} - \text{I}_{\text{m}}}. \tag{4.31}$$

I_{m} is determined as the intensity corresponding to the left-side half maximum of the image histogram (Figure 4.7), and I_{b} is defined as the intensity of the cortical bone. Mean intercept length (MIL), is the ratio of total number of pixels in the bone phase and half the number of transitions between bone and marrow phases at a set of parallel lines across the image [115]. Mean trabecular thickness can be calculated as the average of MILs in different directions.

Another method for determination of the BV/TV involves using an external phantom with a composition corresponding to bone marrow, e.g. oil [45, 96, 181]. The spin density is obtained as a by-product of the determination of T_1 or T_2. The magnetization term M_0 in the decay equation (4.21) is proportional to the spin density of the pixel in question. Assuming that the external phantom has a spin density matching that of bone marrow and that trabeculae make no contribution to the NMR signal, the marrow volume fraction can be calculated as a ratio of spin densities in the regions of interest segmented into trabecular bone and the oil phantom. As this method is not based on binarizing the image, other structural indices cannot be determined.

Strong linear correlations between structural parameters determined with MRI and microCT have been established [167]. Structural indices determined from MR images have been related to mechanical properties [108, 149]. Combining BMD and structural parameters obtained with MRI has improved the assessment of the mechanical properties [108, 109]. Significant differences have been detected between patients with mild and severe osteoarthritis and control group [14].

The relative water and fat content of bone marrow can be determined with NMR spectroscopy from the amplitudes of the corresponding peaks in the spectrum, and the fat content has been linked to the degree of osteoporosis defined by DXA [60]. The water content of mineralized bone is known to correlate negatively with the mechanical properties of trabecular bone [46, 194], and the trabecular size can be determined

by generating a multiple spin echo via the ratio of the amplitudes of consecutive echoes [30]. T_2' measured with an asymmetric spin echo sequence has been related to structural parameters of trabecular bone in human lumbar vertebrae [15].

CHAPTER V

Aims of the present study

Previous studies at high field strengths have shown the feasibility of quantitative MRI parameters to serve as surrogate markers for structure, composition and even for the mechanical properties of articular cartilage. T_2 and dGEMRIC have been applied *in vivo* but the validation of the method in clinically applicable field strength has been partly inadequate. With respect to trabecular bone, methods at clinically applicable field strengths have been utilized for diagnostics of osteoporosis. The main goal of the present study was to detect the changes in articular cartilage and trabecular bone induced by degenerative joint disease. The specific aims of this study were:

1. To determine the similarities and differences between MRI parameters of articular cartilage at 1.5 T and 9.4 T.

2. To test the ability of the quantitative MRI methods to assess the structure, composition and mechanical properties of articular cartilage when applied at 1.5 T.

3. To clarify the ability of T_2 measured in the presence of Gd-DTPA^{2-} to assess the mechanical properties of articular cartilage.

4. To evaluate the changes in MRI parameters during the degeneration of cartilage and their ability to assess the degree of degeneration.

5. To determine the ability of MRI parameters measured at 1.5 T to assess the mechanical properties of trabecular bone.

6. To investigate the interrelations between the structure, composition and mechanical properties of articular cartilage and trabecular bone during degeneration and the ability of quantitative MRI to assess them.

7. To develop and validate spectroscopic methods for evaluation of the structure and composition of trabecular bone.

CHAPTER VI

Materials and methods

The present work consists of four studies (I-IV). Human cadaver patellae from the right knee joint were used for MRI and reference studies of articular cartilage and trabecular bone (studies I-III). For MRS and microCT measurements of trabecular bone (study IV), samples from bovine patellae and femora were used. All materials and methods are summarized in Table 6.1.

6.1 Materials

6.1.1 Human samples

Fourteen pairs of human cadaver knee joints (12 male, 2 female, mean age 55 $\pm$ 18 years) were obtained within 48 h post mortem from the Jyväskylä Central Hospital, Jyväskylä, Finland, with permission from the national authority (National Authority of Medicolegal Affairs, Helsinki, Finland, permission 1781/32/200/01). The right patellae were used for this work. Six topographical locations were assessed to cover the entire articular surface: superolateral (SL), central lateral (CL), inferolateral (IL), superomedial (SM), central medial (CM) and inferomedial (IM) patella (Figure 6.1).

Intact patellae were used for 1.5 T MRI and pQCT measurements. For 9.4 T MRI and mechanical measurements of articular cartilage, cylindrical samples with 4-mm diameter were isolated using a biopsy punch and razor blade. For mechanical testing of trabecular bone, cylindrical samples with 7-mm diameter were isolated using an orthopaedic hollow drill bit. A grinding system was used to parallelize the ends of the cylindrical plugs. The sections cut from the cylindrical samples were used for histological evaluation of cartilage and bone.

The total number of successfully prepared cartilage disks was 75 (for different locations, SL: n=14, CL: n=12, IL: n=12, SM: n=12, CM: n=12, IM: n=13). Five samples were unsuccessfully isolated from the bone, and the cartilage disks with nonuniform thickness could not be mechanically tested. Four samples were too degenerated to be tested mechanically. Mechanical testing of trabecular bone was performed successfully for 46 samples (for different locations, SL: n=7, CL: n=2, IL: n=9, SM: n=8, CM: n=10, IM: n=10). The cylindrical plug required for mechanical testing was not detachable from all sites of interest due to insufficient thickness of trabecular bone. Additionally, the curvature of the bone surface caused overlapping of adjacent medial and lateral plugs from which the other had to be rejected. The remaining 24 bone

Table 6.1: Materials and methods utilized in original studies I-IV.

Tissue	Modality	Sample size	N	Parameters	Study
Articular cartilage (Human)	MRI at 1.5 T	Intact patellae	14(84)*	T_2, dGEMRIC	I, III
	MRI at 9.4 T	∅ 4-mm plugs	76	T_2, dGEMRIC	I, III
	biomechanics	∅ 4-mm plugs	76	$E_{s,c}$, $E_{d,c}$	I, III
	digital densitometry	3-µm Safranin-O-stained sections	76	PG content (OD)	III
				Mankin score	III
	FTIRI	5-µm unstained sections	76	Collagen content (absorption)	III
	polarized light microscopy	5-µm unstained sections	76	orientation, anisotropy, birefringence	unpublished unpublished
Trabecular bone (Human)	MRI at 1.5 T	Intact patellae	14(84)*	T_2^*, BV/TV_{GE}, BV/TV_{SE}	II, III
	pQCT	Intact patellae	14(84)*	BMD, BV/TV_{pQCT}	II, III
	biomechanics	∅ 7-mm plugs	46	$E_{s,b}$, σ_y, σ_u	II, III
	polarized light microscopy	7-µm unstained decalcified sections	24	BV/TV_{REF} orientation, anisotropy	III unpublished
Trabecular bone (Bovine)	NMR at 4.7 T	∅ 22-mm plugs	15	$T_{1\rho}$, T_2, CP-T_2	IV
				$T_{1\rho}$ dispersion	IV
	microCT	∅ 22-mm plugs	15	BV/TV, Tb.Th, Tb.Sp, Tb.N, SMI	IV

* 14 patellae with 6 sample locations on each specimen, altogether 84 samples measured

T_2	T_2 relaxation time	OD	optical density
dGEMRIC	Gd-DTPA^{2-}-enhanced T_1 relaxation time	$E_{s,b}$	elastic modulus of bone
$E_{s,c}$	elastic modulus of cartilage	σ_y	yield stress
$E_{d,c}$	dynamic modulus of cartilage	σ_u	ultimate strength
T_2^*	T_2^* relaxation time	$T_{1\rho}$	$T_{1\rho}$ relaxation time
BMD	bone mineral density	CP-T_2	Carr-Purcell T_2 relaxation time
BV/TV_{GE}	bone volume fraction measured with gradient echo sequence	BV/TV	bone volume fraction
BV/TV_{SE}	bone volume fraction measured with gradient echo sequence	Tb.Th	trabecular thickness
BV/TV_{REF}	bone volume fraction measured with polarized light microscopy	Tb.Sp	trabecular separation
BV/TV_{pQCT}	bone volume fraction measured with pQCT	Tb.N	trabecular number
FTIRI	Fourier transform infrared imaging	SMI	structural model index

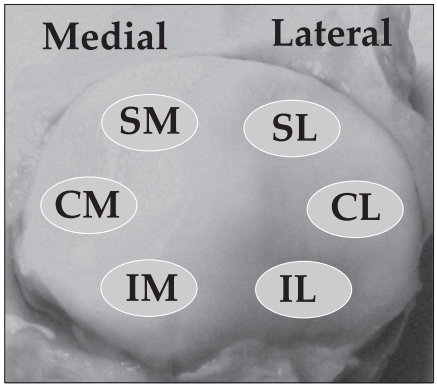

Figure 6.1: The sites of interest on human patellar surface. SM - superomedial, CM - central medial, IM - inferomedial, SL - superolateral, CL - central lateral and IL - inferolateral.

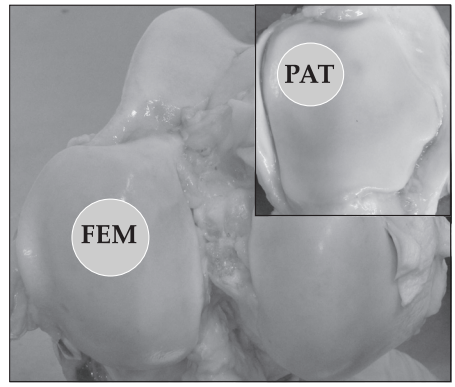

Figure 6.2: The locations used for bovine samples. FEM - medial femoral condyle, and PAT - patella.

cylinders were successfully prepared for polarized light microscopy (for different locations, SL: n=3, CL: n=4, IL: n=2, SM: n=4, CM: n=3, IM: n=8).

6.1.2 Bovine samples and phantoms

Seven bovine knee joints (age 18 months) were obtained from the local slaughterhouse (Atria Oyj, Kuopio, Finland) within a few hours after slaughtering. 22-mm cylindrical osteochondral plugs were isolated from the medial femoral condyle (FEM) and lateral superior facet of patella (PAT) using a hollow drill bit (Figure 6.2).

Test tubes containing glass beads with a diameter of 150-212 µm, 212-300 µm and 425-600 µm (Sigma Aldrich Co.) were used as phantoms emulating a structure with local susceptibility differences inducing local gradient fields. Two sets of phantoms were prepared with the interstitials filled with turnip rape oil or water adulterated with $CuSO_4$ to shorten relaxation times to a range suitable for parameters used in bone measurements.

6.2 NMR measurements

6.2.1 Articular cartilage

MEASUREMENTS AT 1.5 T

The patellae were equilibrated overnight in 0.5 mM Gd-DTPA^{2-} solution (Magnevist, Schering AG, Germany) and wrapped in Parafilm M (Pechiney Plastic Packaging, Chicago, IL) to prevent dehydration. MRI-visible vitamin capsules containing peanut oil (Vitol, Cardinal Health UK 414 Ltd, Wiltshire, UK) were attached at the measurement sites to serve as localization markers. A GE Signa TwinSpeed 1.5 T scanner was used (GE Healthcare, Milwaukee, WI, USA) with a 3" receiving surface coil and the body coil as the transmitting coil. The patellae were oriented the articular surface parallel to the B_0 field to emulate clinical patient positioning. The frequency encoding

direction was oriented perpendicular to the articular surface to minimize the chemical shift artefact. Three slices were measured along the medial-lateral direction, each slice covering two sites of interest (Figure 6.3).

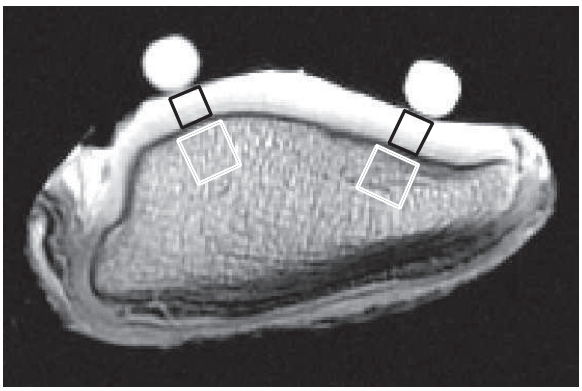

Figure 6.3: The localization of sites of interest in the articular cartilage (black rectangles) and trabecular bone (white squares) with localization markers serving also as oil references at 1.5 T MRI measurements.

T_2 was measured in the presence of the contrast agent because it has been shown to have a minimal effect on T_2 relaxation time at low concentrations such as that used in this study [138]. A multi-slice multi-echo spin echo sequence was used with repetition time (TR) of 1000 ms, eight echo times (TE = 10.3, 20.6, 30.9, 41.2, 51.5, 61.8, 72.1, and 82.4 ms), echo train length (ETL) of 8 and 3-mm slice thickness. A field of view of 8 cm and a 256x256 matrix to yield 0.313 mm in-plane resolution were utilized, with measurements being conducted at room temperature. The slice profile was modified to decrease the contribution of the stimulated echoes to the signal [112]. dGEMRIC was measured using an inversion recovery fast spin echo sequence with TR of 1700 ms, TE of 11 ms and six inversion times (TI = 11 ms, TI = 50, 100, 200, 400, 800, and 1600 ms), ETL of 6 and resolution and localization equal to those on T_2 measurements.

Full-thickness regions of interest (ROI) of a width matching the slice thickness (3 mm or 10 pixels) were segmented at the sites of interest (Figure 6.3). To avoid the partial volume effect, the most superficial pixel which includes cartilage was omitted from the analysis. The MRI parameter maps were fitted into monoexponential relaxation equations ((4.21) for T_2 and (4.23) for dGEMRIC) using an in-house software (MATLAB, Mathworks Inc., Natick, MA). The T_2 maps were calculated using all eight echoes. For some regions of interest, T_2 values were calculated omitting the first echo to determine the potential effect of stimulated echoes, and similar results were obtained. Spatial depth-wise profiles were calculated by averaging the pixels of the region of interest along the direction of the cartilage surface.

MEASUREMENTS AT 9.4 T

Measurements were conducted using a 9.4 T Oxford NMR vertical magnet (Oxford Instruments PLC, Witney, UK), a SMIS console (SMIS Ltd, Surrey, UK), and a 5-mm

high-resolution volume spectroscopy probe (Varian Associates Inc., Palo Alto, CA). The samples were sealed in a test tube (dia.= 5 mm) immersed in Gd-DTPA^{2-} solution. The samples were located axially in the center of the coil, and the sample surface was oriented perpendicular to the B_0 field, as limited by the coil construction. T_2 was determined using a single echo spin echo sequence with a minimized sensitivity to diffusion with TR of 1500 ms, six TE's (14, 20, 28, 40, 56, and 80 ms) and 1-mm slice thickness. A field of view of 1 cm and a 256x64 matrix to yield 0.039 mm resolution across cartilage depth were utilized at temperature of 25°C. dGEMRIC measurements were conducted using a saturation recovery sequence with TE of 14 ms and six TR's (100, 180, 330, 600, 1100, and 2000 ms).

The MRI parameter maps were fitted into monoexponential relaxation equations ((4.21) for T_2 and (4.24) for dGEMRIC). Full-thickness ROIs with widths matching the slice thickness (1 mm or 7 pixels) were segmented. Spatial depth-wise profiles were calculated by averaging the pixels of the region of interest along the direction of the cartilage surface.

Comparison of the results between 1.5 T and 9.4 T

Profiles at 1.5 T were truncated to match the thickness of the 9.4 T measurements, since a thin layer of the deepest tissue typically remained on the bone when the cartilage disks were isolated. The relaxation time profiles of the 9.4 T measurements were downsampled to match the depthwise resolution of the 1.5 T measurements. From the profiles, relaxation times for the approximately 1 mm of the most superficial tissue (three pixels at 1.5 T and 24 pixels at 9.4 T) and bulk values covering the full thickness of uncalcified cartilage were determined. Since the thickness of the superficial cartilage layer was beyond the resolution of 1.5 T measurements, the superficial values of MR parameters refer to the values calculated for the most superficial 1 mm of tissue.

6.2.2 Trabecular bone

T_2^* measurements

All MRI measurements of human trabecular bone were conducted at 1.5 T using a GE Signa TwinSpeed scanner and a 3" receiving surface coil and the body coil as the transmitting coil. The patellae were oriented similarly to the cartilage measurements. T_2^* was measured using a gradient echo sequence with TR of 100 ms, six TE's (4.7, 9.3, 14, 18.7, 23.4, 28 ms) and a flip angle of 30°. The localization and resolution were equal to cartilage measurements at 1.5 T. Square ROIs of 7x7 mm were segmented at the sites localized by the markers (Figure 6.3). The T_2^* maps were determined by fitting into the relaxation equation (4.22), and the mean values were calculated. The R_2^* relaxation rate was calculated as the inverse of each bulk T_2^* value (i.e. $1/T_2^*$).

Morphological evaluation

A fast gradient echo sequence with TR of 30 ms, TE of 4 ms and flip angle = 40° was used. For each patella, 40 consecutive slices with thickness of 1 mm, a field-of-view of 6 cm and a 256x256 matrix yielding a 0.234 mm in-plane resolution were imaged to cover the entire trabecular bone volume in the structural assessment. A

7x7x7 mm volume of interest (VOI) was assessed, having the centremost slice at the location of the T_2^* measurements. The apparent bone volume fraction (BV/TV_{GE}) of each location was calculated based on the histograms of the signal intensities in the selected volumes as described in section 4.7 and [114].

Bone volume fraction was estimated also from T_2 measurement data of articular cartilage by comparing the spin density in selected ROI and localization markers functioning also as an oil reference (Figure 6.3) [45, 96]. Trabeculae were assumed to have negligible NMR signal; thus the spin density of each ROI was assumed to be entirely due to bone marrow. The oil reference was chosen to represent the case of ROI consisting of only bone marrow. The marrow volume fraction in each ROI was calculated by dividing the spin density of each ROI with the spin density of the oil reference in each image. Apparent bone volume fraction (BV/TV_{SE}) was calculated by subtracting the marrow volume fraction from unity.

Spectroscopic NMR measurements

MRS measurements were conducted using a 4.7 T Magnex horizontal magnet (Magnex Scientific Ltd., Abington, UK) and Varian ^{UNITY}INOVA console (Varian Inc., Palo Alto, CA, USA) and an in-house surface coil in the transmit/receive mode. A 5x5x5 mm voxel was localized under the dense subchondral plate.

Localized single voxel spectra were measured using the LASER (Localization by Adiabatic Selective Refocusing, [52]) pulse sequence (TR = 5 s, TE = 23 ms, bandwidth of 2500 Hz covered with 1000 points). $T_{1\rho}$ weighting was obtained with a spin-lock preparation block consisting of an adiabatic half-passage (AHP), variable length spin-lock period and reverse AHP [58] followed by a crusher gradient. Seven spin-lock times (19.5-79.5 ms) were used at ten different B_1 field strengths (0.018-0.18 mT) to determine $T_{1\rho}$ in different spin-lock fields, i.e. $T_{1\rho}$ dispersion. The frequency of the on-resonance spin-lock preparation block was set to either fat ($T_{1\rho,\mathrm{f}}$) or water ($T_{1\rho,\mathrm{w}}$) resonance frequency.

T_2 relaxation time was measured using the same LASER pulse sequence for localization and a double spin echo preparation block consisting of AHP, two hyperbolic secant (HS) adiabatic full passages and reverse AHP (TR = 5 s, 30 TE's between 23 and 143 ms). Carr-Purcell-T_2 (CP-T_2) was determined with two different techniques (Figure 6.4). TE was incremented by increasing either the interval between refocusing pulses (τ_{CP}) or the number of refocusing pulses and keeping τ_{CP} constant. While modulating the number of refocusing pulses, the CP pulse train consisted of 0, 4, 8, 16, 20 and 24 HS pulses (τ_{CP} = 4 ms), yielding TE's between 23 and 117 ms. When multiple pairs of HS pulses were used, they were phase cycled according to the MLEV scheme [105]. To control the influence of $T_{2\rho}$ relaxation during RF pulses, three TE's (39, 70 and 101 ms) were produced modulating the interval between four refocusing pulses (τ_{CP} = 4-23 ms) and the results were compared with measurements with adiabatic 0°pulses, with similar amplitude and phase modulation functions, placed symmetrically between refocusing pulses [127].

Diffusion coefficients were determined using a spectroscopic STEAM sequence (TR = 2.5 s, TE = 19 ms, TM = 6 ms) [148]. Diffusion coefficients were determined for fat and water separately in seven directions with nine b-values between 100 and 900 s/mm^2. The 1/3 trace of the diffusion tensor (D_{av}) was calculated for fat and

water.

Signal values were determined from the resulting magnitude spectra separately for fat and water. The corresponding $T_{1\rho}$, T_2 and diffusion coefficient values were fitted into relaxation/diffusion formulae (4.25), (4.21) and (4.27), respectively. The apparent amplitude of the local susceptibility gradient was calculated from T_2 and CP-T_2 measurements using (4.18) and (4.19) assuming that the contributions of static dephasing and exchange would be constant.

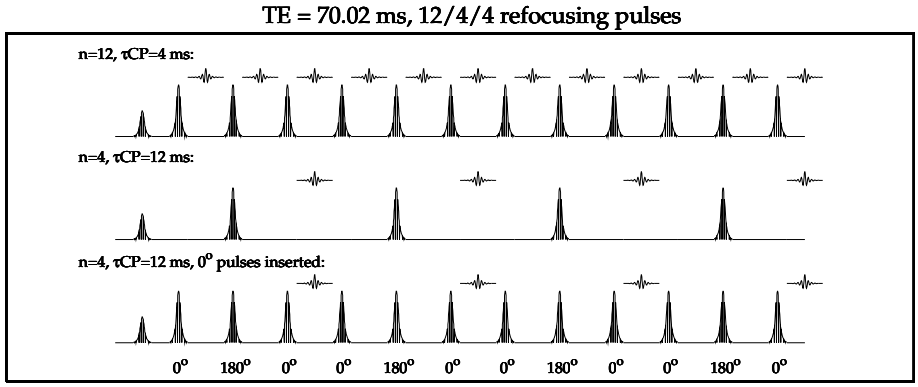

Figure 6.4: Pulse sequences used to obtain the T2 relaxation time in addition to the double spin echo sequence. Top: Carr-Purcell utilizing twelve 180°pulses. Middle: Carr-Purcell utilizing four 180°pulses. Bottom: The same pulse sequence with 0°adiabatic pulses inserted symmetrically around 180°pulses. The echoes forming due to the refocusing of the transverse magnetization are denoted.

6.3 Mechanical testing

6.3.1 Articular cartilage

Samples were re-equilibrated in phosphate-buffered saline solution including enzyme inhibitors (5 mM EDTA and 5 mM benzamide HCl) for at least 2 h to wash out the ionic contrast agent that could possibly affect the swelling pressure of cartilage. Mechanical testing was performed with a custom made high-resolution material testing device including a load cell with resolution of 5 mN (Honeywell Sensotec, Columbus, OH) and a precision motion controller with 0.1 µm resolution (Newport, Irvine, CA) [186]. A stress-relaxation test was performed in unconfined compression geometry. After establishing a proper surface contact, a 10% pre-strain step was applied, followed by a 1-hour relaxation. Subsequently, this was followed by three 2% steps at 1 µm/s ramp velocity and 40 min relaxation after each step. A dynamic test with 1 Hz frequency and 1% strain amplitude was conducted after the stress-relaxation test. Young's modulus ($E_{\mathrm{s,c}}$) and the dynamic modulus ($E_{\mathrm{d,c}}$) were determined from the stress-relaxation and dynamic tests, respectively, as described in Section 3.1. The measurements and analyses were conducted using an in-house Labview program (Labview 6, National Instruments, TX, USA).

6.3.2 Trabecular bone

A hydraulic 25 kN material testing device was used for mechanical testing (Instron FastTrack 8874, Instron, Norwood, MA, USA). The testing protocol included equilibration of the sample under a pre-stress of 10 N for 2 min, five nondestructive dynamic cycles with 0.5% strain and destructive compression to 5% strain with a ramp velocity of 5 µm/s. Young's modulus ($E_{s,b}$), yield stress (σ_y) and ultimate strength (σ_u) were determined as described in Section 3.2. The analysis was conducted with an in-house MATLAB script.

6.4 Computed tomography of trabecular bone

6.4.1 pQCT measurements

Plastic markers were used to localize the measurement sites. BMD was measured from three slices the localization of which corresponded to the slices in T_2^* measurements using a voltage of 58 kV, current of 0.175 mA, exposure time of 3 min 35 s, in-plane resolution of 0.200 mm and 0.5 mm slice thickness (XCT 2000, Stratec Medizintechnik GmbH, Birkenfeld, Germany). A BMD value for a 7x7 mm ROI, localized in the trabecular bone, was calculated. The apparent bone volume fraction (BV/TV_{pQCT}) was determined for each region of interest using the same technique as with MRI gradient echo images [114].

6.4.2 MicroCT measurements

The structural parameters of bovine samples were determined using a high-resolution computed tomography scanner (SkyScan 1172, SkyScan, Artselaar, Belgium). A three-dimensional data set was scanned from all samples with voltage of 100 kV, current of 100 µA, exposure time of 590 ms and nominal voxel size of 11x11x11 μm^3. Rotation between projections was 0.4°, and 10 exposures were averaged for each projection. A cylindrical ROI with diameter of 7 mm and length of 5 mm was binarized, and morphometric parameters (bone volume fraction BV/TV, trabecular thickness Tb.Th, trabecular separation Tb.Sp, trabecular number Tb.N and structural model index (SMI)) were calculated. SMI provides an indication of the relative prevalence of rods and plates in the three-dimensional structure [72, 77]. The image reconstruction and analysis were conducted using NRecon and CTAN software, respectively, provided by the scanner manufacturer.

6.5 Histological methods

6.5.1 Articular cartilage

DIGITAL DENSITOMETRY

The PG content of cartilage matrix was assessed with digital densitometry of 3-µm thick Safranin-O stained sections. When applied under standardized conditions, the cationic Safranin-O stains the cartilage section stoichiometrically with its content of negatively charged GAG [92]. A calibrated digital densitometer was used to measure the optical density of the stained sections to estimate PG content [90]. The measuring

device consisted of a Leitz Othoplan microscope (Leitz Messtechnik GmbH, Wetzlar, Germany) and a Peltier-cooled 12-bit Photometrics CH-250-A CCD-camera (Roper Scientific Inc., Tucson, AZ, USA). Data analysis was conducted with the IP-Lab program (version 3.55., Scananalytics Inc., Fairfax, VA, USA). Three sections were analyzed and the results were averaged to minimize the error due to variations in section thickness, and the average value for the whole section was calculated to represent the mean value of proteoglycan content in the sample.

Fourier transform infrared imaging microscopy

The collagen content was estimated from unstained 5 µm thick sections with spectroscopic Fourier Transformed Infrared Imaging (FTIRI) technique [150, 28]. Integrated absorbance of amide I peak was used [159]. Measurements were conducted using a PerkinElmer Spotlight 300 imaging system (PerkinElmer Inc., Wellesley, MA, USA). Three sections were averaged to minimize the error due to section thickness, and the average value for the whole section was calculated to represent the mean value of the collagen content in the sample.

Polarized light microscopy

The orientation of collagen fibrils was estimated using polarized light microscopy of the unstained sections with a thickness of 5 µm. A cross-polarized light microscope with computer controlled rotating strain-free polarizers was used to capture seven background corrected images from each section at 15° intervals with a high-performance Peltier-cooled CCD camera. By determining the signal intensity in each pixel of the image, spatial maps of orientation-independent birefringence, collagen fiber orientation compared to cartilage surface and anisotropy could be calculated to evaluate the collagen fibril network organization [158].

Mankin Score

The histological Mankin score of the samples was independently evaluated by three trained observers from blind-coded Safranin-O stained sections. The Mankin score is a subjective score of cartilage degeneration that takes into account the cartilage structure, amount of cells, order of Safranin-O staining and the integrity of the tidemark (Table 6.2) [117]. Since the samples were detached from subchondral bone, the integrity of the tidemark could not be evaluated.

The samples were divided into three groups according to their Mankin score: samples with no or minimal degeneration (group I, Mankin score < 4), moderate degeneration (group II, $4 \leq$ Mankin score < 8) and advanced degeneration (group III, Mankin score ≥ 8) (Figure 6.5).

6.5.2 Trabecular bone

Unstained, decalcified sections with a thickness of 7 µm were prepared for polarized light microscopy from bone cylinders too short for biomechanical testing (specimen length less than 7 mm, see Section 3.2) [92, 89]. Microscopic collagen network of the bone matrix was visualized with the same technique as articular cartilage. The method is insensitive to cells as well as to loose connective and adipose tissue in the

Table 6.2: Criteria for evaluating the Mankin score of cartilage sample [117]. The integrity of the tidemark could not be evaluated in the absence of subchondral bone. The Mankin score is obtained as a sum of grades of properties I-III.

	Grade		Grade
I. Structure		**III. Safranin-O staining**	
Normal	0	Normal	0
Surface irregularities	1	Slight reduction	1
Pannus and surface irregularities	2	Moderate reduction	2
Clefts to transitional zone	3	Severe reduction	3
Clefts to radial zone	4	No dye noted	4
Clefts to calcified zone	5		
Complete disorganization	6		
II. Cells			
Normal	0	**IV. Tidemark integrity**	
Diffuse hypercellularity	1	Intact	0
Cloning	2	Crossed by blood vesels	1
Hypocellularity	3		

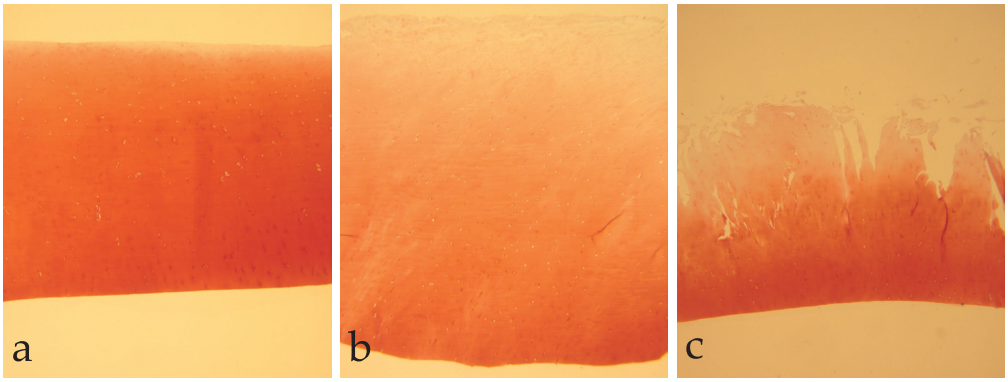

Figure 6.5: Safranin-O stained sections representing three groups of degeneration: (a) no or minimal degeneration (group I, Mankin score < 4), (b) moderate degeneration (group II, 4 $\leq$ Mankin score < 8) and (c) advanced degeneration (group III, Mankin score $\geq$ 8) classified by Mankin score of the samples. The cartilage surface is towards the top of the page.

bone marrow space since these structures do not reveal any regular organization as detected by polarized light microscopy. The areal fraction of the bone collagen matrix was calculated from the binarized, background corrected birefringence images using a 9.26 µm spatial pixel size, and used as an estimate for bone volume in the three-dimensional space (BV/TV_{REF}).

6.6 Statistical analyses

Pearson correlation coefficient was calculated to determine linear associations between different variables. The ability of MRI and pQCT variables to assess the mechanical properties of trabecular bone was studied using step-wise linear regression. The linear mixed model test was applied to test the statistical significance of topographical variation of parameters. The linear mixed model provides an accurate comparison of data with missing values by also modeling variances and covariances of data [21]. Further, the possible sample interdependencies are acceptable, for example, the dependency between the samples at different locations obtained from the same patella. The statistical differences between different stages of degeneration were tested using Kruskal-Wallis test and Mann-Whitney U-test. The statistical differences between MRI variables obtained at different field strengths and between bone volume fractions obtained with different techniques were tested with paired-samples T-test. The significance of the difference between two correlation coefficients was tested by using the standard Fisher Z-score test [205]. Statistical analyses were conducted by using the SPSS software (version 11.5, SPSS Inc, Chicago, IL).

CHAPTER VII

Results

7.1 Articular cartilage

7.1.1 Differences between MRI parameters measured at 1.5 T and 9.4 T

The relaxation time maps of T_2 and dGEMRIC displayed a similar pattern at different field strengths (Figure 7.1). Depth-wise T_2 profiles revealed a similar shape at 1.5 T and 9.4 T, with longer values in the more superficial tissue and shorter values in the deeper cartilage (Figure 7.2), despite the 90-degree orientation difference in the B_0 field. However, an offset of about 20 ms was present. The variation of T_2 and dGEMRIC at both field strengths is shown in Table 7.1. T_2 relaxation times measured at different field strengths were linearly correlated by r=0.36 (p<0.01) and r=0.35 (p<0.01), and dGEMRIC values by r=0.25 (p<0.05) and r=0.26 (p<0.05) for superficial and bulk tissue, respectively. All superficial and bulk variables showed a statistically significant difference between the field strengths.

7.1.2 MRI and mechanical properties

Young's modulus at equilibrium ($E_{\mathrm{s,c}}$) and dynamic modulus ($E_{\mathrm{d,c}}$) of articular cartilage reflected the considerable variation within samples (Table 7.2). $E_{\mathrm{s,c}}$ and $E_{\mathrm{d,c}}$

Table 7.1: Mean, SD, minimum and maximum values for MRI variables of articular cartilage at 1.5 T and 9.4 T. s - superficial region, b - bulk region.

	Variable	Mean	SD	Minimum	Maximum
1.5 T	$\mathrm{dGEMRIC_s}$	297	48	188	392
	$\mathrm{dGEMRIC_b}$	303	50	187	398
	$T_{2,\mathrm{s}}$	63	17	29	105
	$T_{2,\mathrm{b}}$	52	15	32	116
9.4 T	$\mathrm{dGEMRIC_s}$	593	125	392	1082
	$\mathrm{dGEMRIC_b}$	645	124	407	1083
	$T_{2,\mathrm{s}}$	40	10	22	62
	$T_{2,\mathrm{b}}$	28	7	17	50

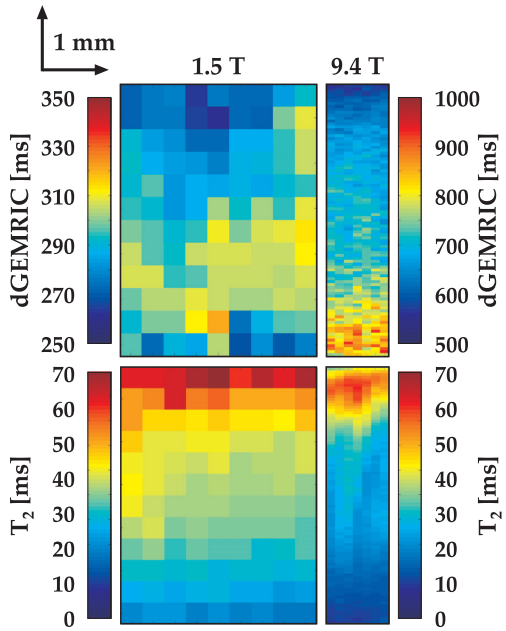

Figure 7.1: Relaxation maps at 1.5 T and 9.4 T calculated for a representative sample without the subchondral bone. 1.5 T maps were truncated to match the thickness of the isolated cartilage sample measured at 9.4 T. The articular surface is directed towards the top of the page.

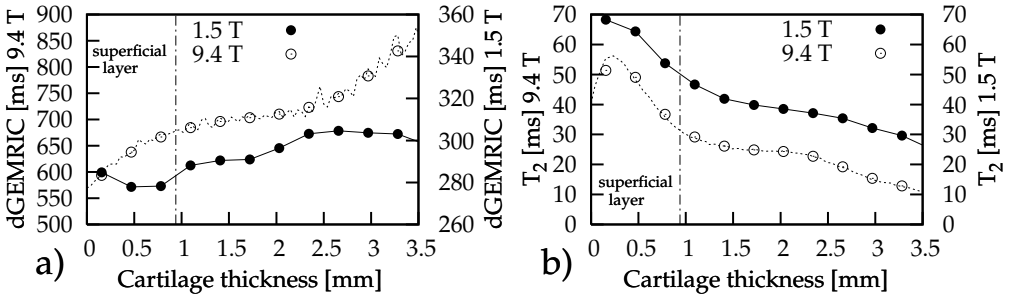

Figure 7.2: Depth-wise relaxation profiles at 1.5 T and 9.4 T calculated for a representative sample. Dashed line displays profile measured at 9.4 T at original resolution. The superficial layer denoted here is wider than the superficial layer defined by collagen orientation.

Table 7.2: Mean, SD, minimum and maximum values for mechanical variables of cartilage.

Variable	Mean	SD	Minimum	Maximum
$E_{s,c}$	0.53	0.42	0.02	2.56
$E_{d,c}$	3.87	2.70	0.18	12.29

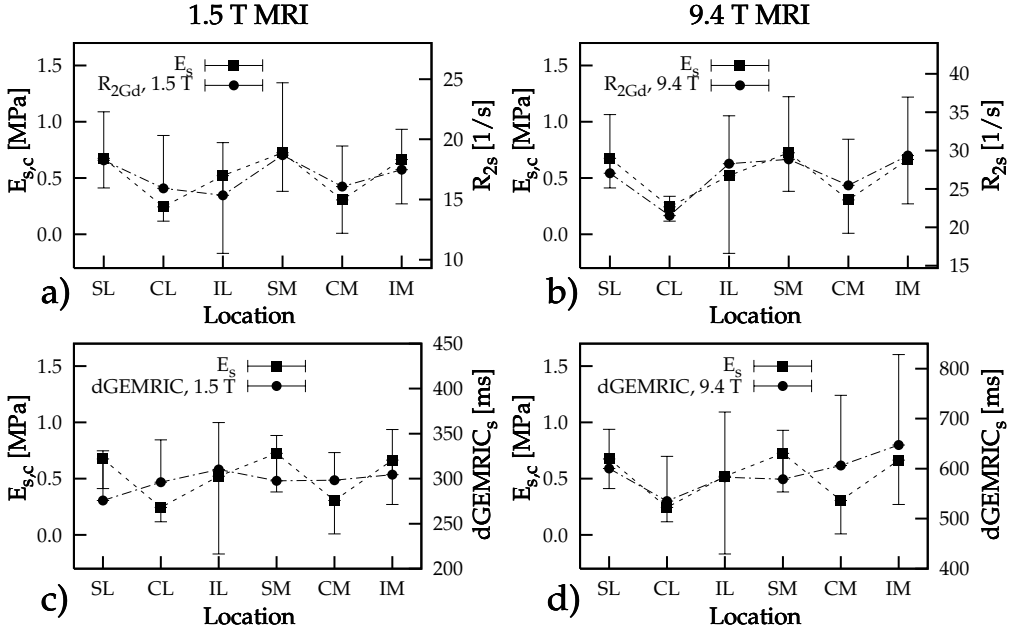

Figure 7.3: Topographical variation of MRI parameters and $E_{s,c}$ of articular cartilage. Mean and SD values for six measurement locations are shown. The variation of $E_{d,c}$ is similar to that of $E_{s,c}$. R_2 (i.e. $1/T_2$) is used for visualization purposes.

showed a strong linear correlation with each other (r=0.92, p<0.01, N=75).

Significant linear correlations between the MRI parameters and the mechanical moduli were observed at both field strengths (Table 7.3); at 1.5 T, the highest linear correlations were observed between T_2 and mechanical parameters (T_{2s} vs. $E_{d,c}$, r=-0.62, p<0.01), whereas at 9.4 T dGEMRIC showed the highest linear correlations with mechanical moduli (dGEMRIC$_s$ vs. $E_{s,c}$, r=0.47, p<0.01). The difference in correlation coefficients at different field strengths was statistically significant between superficial T_2 and $E_{s,c}$ (p = 0.02) and between superficial T_2 and $E_{d,c}$ (p < 0.01).

The linear correlations between MRI parameters and mechanical properties calculated for medial and lateral facets and all six locations showed remarkable variation (see study I, Tables 4-5). At the medial facet, T_2 values at 1.5 T revealed the strongest linear correlations with mechanical parameters (T_2 vs. $E_{s,c}$, r=-0.75, p<0.01), while at the lateral facet, dGEMRIC values at 9.4 T showed the highest correlations (dGEMRIC$_s$ vs. $E_{s,c}$, r=0.62, p<0.01).

The topographical variation of superficial T_2 (or $1/T_2$, i.e., relaxation rate R_2) and mechanical parameters showed similar trends at both field strengths, whereas dGEMRIC showed only a weak association (Figure 7.3). The topographical variation of $E_{s,c}$ and $E_{d,c}$ revealed statistically significant (p<0.05) differences between the locations SL-CL, SL-SM, CL-SM, CL-IM, SM-CM, and CM-IM. Additionally, variation of $E_{d,c}$ was significant between sites SL-IL and IL-SM. For superficial T_2 at 9.4 T, the variation was significant between sites SL-CL, CL-IL, CL-CM, and CL-IM.

Table 7.3: Linear correlations between MRI, mechanical and histological parameters of articular cartilage.

		PG	Collagen	$E_{s,c}$	$E_{d,c}$
1.5 T	dGEMRIC$_s$	NS	NS	0.30*	NS
	dGEMRIC$_b$	NS	NS	NS	NS
	$T_{2,s}$	-0.53**	-0.57**	-0.54**	-0.62**
	$T_{2,b}$	-0.39**	-0.43**	-0.40**	-0.46**
9.4 T	dGEMRIC$_s$	0.41**	0.32**	0.35**	0.39**
	dGEMRIC$_b$	0.45**	0.30**	0.31**	0.35**
	$T_{2,s}$	-0.28*	-0.54**	NS	-0.24*
	$T_{2,b}$	-0.47**	-0.50**	NS	-0.28**

** $p < 0.01$; * $p < 0.05$; NS - not significant

7.1.3 MRI and histology

PG content (optical density) and collagen content (absorbance) varied between 0.18 and 1.97 and between 0.02 and 0.39, respectively. The mean$\pm$SD values were 1.16$\pm$0.42 and 0.24$\pm$0.05 for PG and collagen contents, respectively. There were significant linear correlations between MRI and the histological parameters (Table 7.3). The difference in correlation coefficients at different field strengths was statistically significant between superficial T_2 and PG content (p = 0.06). The PG content correlated significantly with $E_{s,c}$ and $E_{d,c}$ (r = 0.55 and 0.62, respectively, $p < 0.01$). The collagen content correlated similarly with $E_{s,c}$ and $E_{d,c}$ (r = 0.58 and 0.68, respectively, $p < 0.01$).

7.1.4 Degeneration-related changes

Both bulk and superficial dGEMRIC at 1.5 T and 9.4 T exhibited a similar trend of decreased values in group III indicating loss of PGs (Figure 7.4). The difference between groups was statistically significant at 9.4 T but insignificant at 1.5 T. There was an increasing trend in the T_2 relaxation time in line with the progression of cartilage degeneration. Superficial T_2 relaxation time at 1.5 T revealed statistically significant differences between group III and the other groups, and bulk T_2 differentiated even between groups I and II. There were no significant differences in T_2 between groups at 9.4 T; however a trend with slightly increasing values towards the advanced degeneration was evident. Mechanical properties and PG content differentiated all groups, and collagen content separated group III from other groups, all three showing a systematic trend with decreasing values along advancing degeneration.

Depth-wise profiles of angle of main orientation calculated from polarized light microscopic images were used to extract a subgroup of samples with a visible superficial collagenous zone present. The samples were divided into three groups according to their Mankin score (group A, 0 < Mankin Score < 3.3, n=12; group B, 3.3 < Mankin Score < 6.7, n=20; and group C, 6.7 < Mankin Score < 9, n=10). The thicknesses of the profiles were normalized to unity by interpolation, and averaged depth-wise T_2 profiles were calculated for each group.

As compared to the group with the least degeneration (group A), group B showed

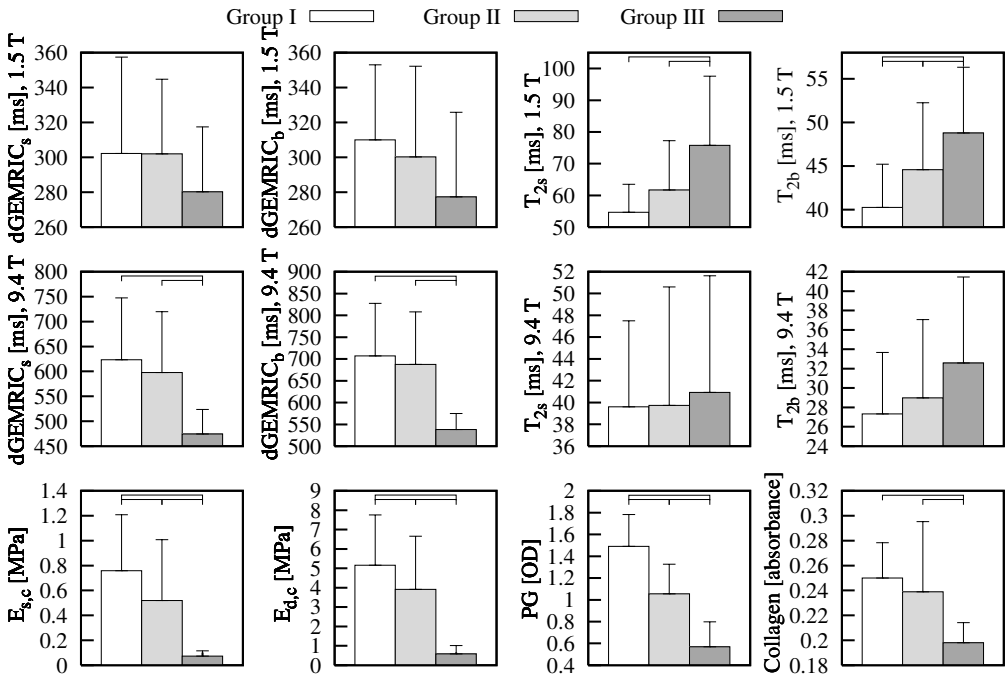

Figure 7.4: Mean ± SD values for cartilage variables divided into three groups according to their Mankin Score. Statistical difference between groups ($p < 0.05$) is denoted with brackets.

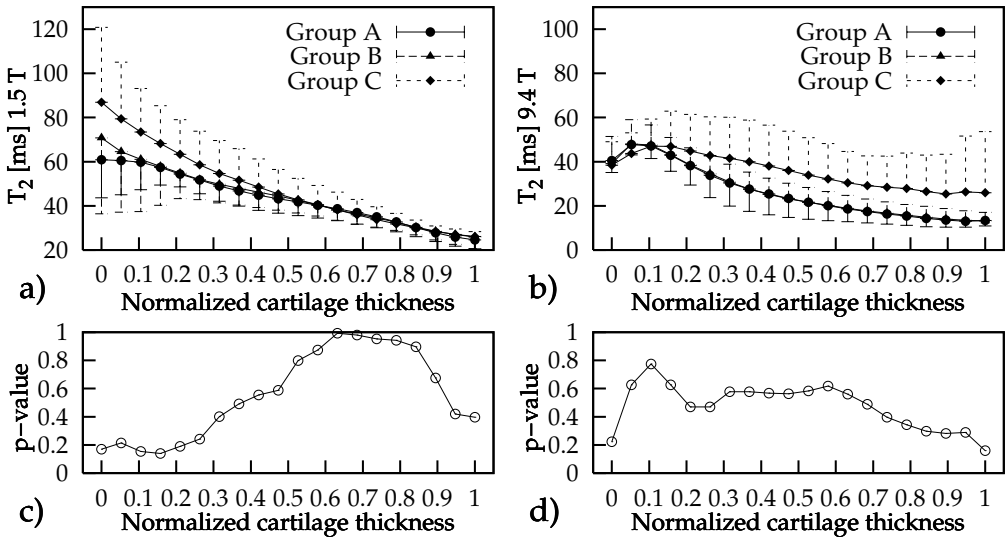

Figure 7.5: Depth-wise T_2 relaxation time profiles, (a) and (b), and depth-wise p-values of differences of T_2 values of three degeneration groups, (c) and (d), calculated for groups with different degrees of degeneration at 1.5 T and 9.4 T, respectively.

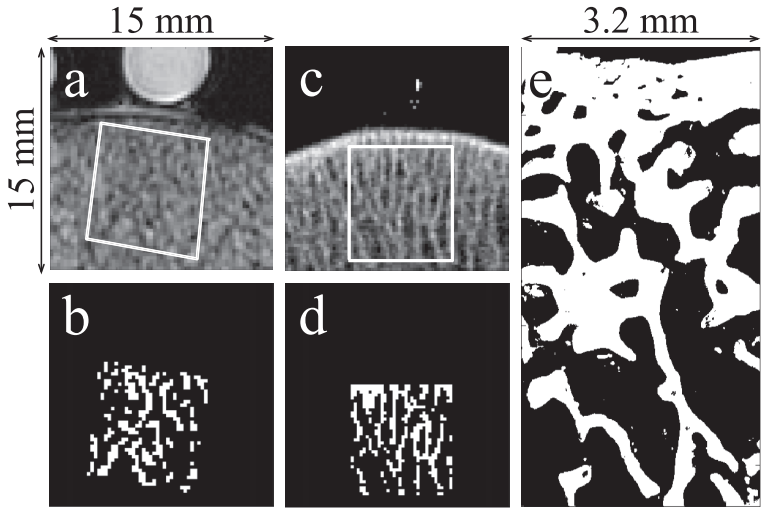

Figure 7.6: Binarized images obtained with MRI (a,b), pQCT (c,d) and microscopy (e). The MRI and pQCT images are on the same scale whereas the microscopic image is more magnified.

a trend toward prolonged T_2 values to approximately 10% of tissue thickness at 1.5 T (Figure 7.5a). Group C showed a significant increase in the T_2 value to approximately 50% of tissue thickness as compared to groups A and B. For the remaining 50%, the depth-wise profiles for the three groups exhibited similar T_2 values. The most superficial layer of articular cartilage was not visible in the T_2 profiles at 1.5 T because its thickness is typically beyond the resolution of clinical MRI devices.

The orientation of the samples with respect to the B_0 field differed 90° between 1.5 T and 9.4 T. At 9.4 T, an increase in T_2 was observed for the group with most degeneration (Group C) in the radial zone (Figure 7.5b). Groups A and B showed similar profiles throughout the cartilage thickness. At both field strengths, the increase in T_2 was observed in the cartilage layer with the collagen orientation parallel to the B_0 field.

Due to the extensive variation and the relatively small number of samples in each group, there were no statistically significant differences between the groups at any point along the depth-wise profile, however the p-values were considerably smaller near the surface for T_2 measured at 1.5 T (Figure 7.5c). For 9.4 T, the smallest p-values were detected from the most superficial and deep values.

7.2 Trabecular bone

7.2.1 MRI and pQCT measurements

The bone volume fraction was determined with a gradient echo (BV/TV_{GE}) and spin echo (BV/TV_{SE}) MRI sequences, pQCT (BV/TV_{pQCT}) and polarized light microscopy (BV/TV_{REF}). The determinations of BV/TV_{GE}, BV/TV_{pQCT} and BV/TV_{REF} were based on binarized images whereas BV/TV_{SE} was based on spin densities of regions of in-

Table 7.4: Mean, SD, minimum and maximum values of bone volume fractions measured with different methods and bone mineral density.

	Mean	SD	Minimum	Maximum
BV/TV_{GE}	0.32	0.08	0.13	0.54
BV/TV_{SE}	0.46	0.10	0.22	0.69
BV/TV_{pQCT}	0.28	0.07	0.18	0.53
BV/TV_{REF}	0.37	0.12	0.12	0.57
BMD [mg/cm^3]	388	102	192	666

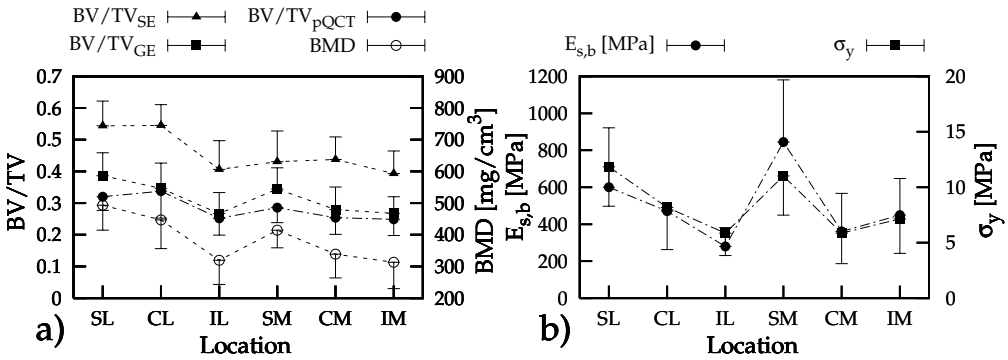

Figure 7.7: Topographical variation of a) parameters measured with MRI and pQCT and b) mechanical properties of trabecular bone. Mean and SD values for six measurement locations are displayed. The variation of σ_u is similar to that of σ_y.

terest and oil reference regions (Section 6.2.2). The binarized images obtained with MRI, pQCT and microscopy are shown in Figure 7.6.

Bone volume fractions measured with different methods showed different values (Table 7.4). All bone volume fractions displayed statistically significant difference between each other except for BV/TV_{GE} and BV/TV_{REF}. However, the topographical variation of BMD and MRI-derived bone parameters showed similar trends (Figure 7.7a). The topographical variation of BMD and BV/TV_{GE} is very similar.

The linear correlations between variables measured with different modalities and the linear correlations between the mechanical, MRI and pQCT variables were statistically significant (Table 7.5). By combining R_2^* and BV/TV_{SE} into a linear regression model, the assessment of BMD and BV/TV_{pQCT} was slightly improved from that obtained with the individual MRI parameters. The BV/TV_{SE} displayed a trend towards higher correlation with BV/TV_{pQCT} as compared to BV/TV_{GE}; however the difference was not statistically significant. The linear correlation coefficient between BV/TV_{GE} and BV/TV_{SE} was 0.38 ($p < 0.01$). When samples only with a Mankin score < 4 were analyzed, the correlation coefficient between BV/TV_{REF} and T_2^* and between BV/TV_{REF} and BMD increased from 0.09 (not significant) to -0.86 ($p < 0.05$) and from 0.58 ($p < 0.01$) to 0.91 ($p < 0.01$), respectively. Despite the small number of samples, the increase is statistically significant ($p < 0.05$) in both cases.

Table 7.5: Correlation coefficients between MRI, pQCT and mechanical variables of trabecular bone.

	$E_{s,b}$	σ_y	σ_u	BV/TV_{pQCT}	BMD
BV/TV_{GE}	0.32^{*}	0.40^{**}	0.46^{**}	0.51^{**}	0.56^{**}
BV/TV_{SE}	NS	NS	NS	0.55^{**}	0.66^{**}
R_2^*	NS	0.37^{*}	0.36^{*}	0.25^{*}	0.34^{*}
MRI model 1	NS	0.50^{**}	0.54^{**}	0.60^{**}	0.52^{**}
MRI model 2	NS	0.39^{**}	0.39^{**}	0.57^{**}	0.68^{**}
BV/TV_{pQCT}	0.36^{*}	0.44^{**}	0.49^{**}	-	0.82^{**}
BMD	0.44^{**}	0.61^{**}	0.64^{**}	0.82^{**}	-
pQCT model	0.44^{**}	0.62^{**}	0.65^{**}	-	-

** $p < 0.01$; * $p < 0.05$; NS - not significant
MRI model 1 - linear combination of BV/TV_{GE} and R_2^*
MRI model 2 - linear combination of BV/TV_{SE} and R_2^*
pQCT model - linear combination of BV/TV_{pQCT} and BMD

7.2.2 MRI and mechanical properties

(BV/TV_{GE}) and (BV/TV_{pQCT}) displayed statistically similar associations with $E_{s,b}$. In addition, (BV/TV_{GE}), (BV/TV_{pQCT}) and BMD correlated better with ultimate strength (σ_u) and yield stress (σ_y) than with $E_{s,b}$; however the difference in correlation coefficients was not statistically significant. BV/TV_{SE} did not correlate with the mechanical properties.

The assessment of σ_y and σ_u was improved by combining R_2^* and MRI-derived apparent bone volume fractions into different linear regression models (Table 7.5). No further improvement in assessment of σ_y and σ_u was obtained by combining pQCT variables. Although BMD showed a trend towards a more accurate assessment of mechanical properties compared to MRI models, there was no statistically significant difference between the correlation coefficients. The optimal linear regression model was calculated separately for each variable to be assessed. $E_{s,b}$ correlated significantly with yield strength and ultimate strength ($r = 0.83$ and 0.87, respectively, $p < 0.01$), and a significant correlation was established between σ_y and σ_u ($r = 0.98$, $p < 0.01$). $E_{s,b}$ of the superomedial location (SM) was relatively high compared to other locations (Figure 7.7b); however other variables did not replicate this improvement.

7.2.3 Degeneration-related changes

For bone variables, BMD and BV/TV_{pQCT} indicated significant difference between groups I and III with decreasing values along cartilage degeneration (Figure 7.8). The mechanical properties of trabecular bone exhibited a significant difference between groups I and II but not between groups I and III despite a similar difference in their mean values. This is likely due to the small number of samples in group III ($n = 3$). MRI variables of trabecular bone did not show any significant differences between groups divided by the degree of cartilage degeneration.

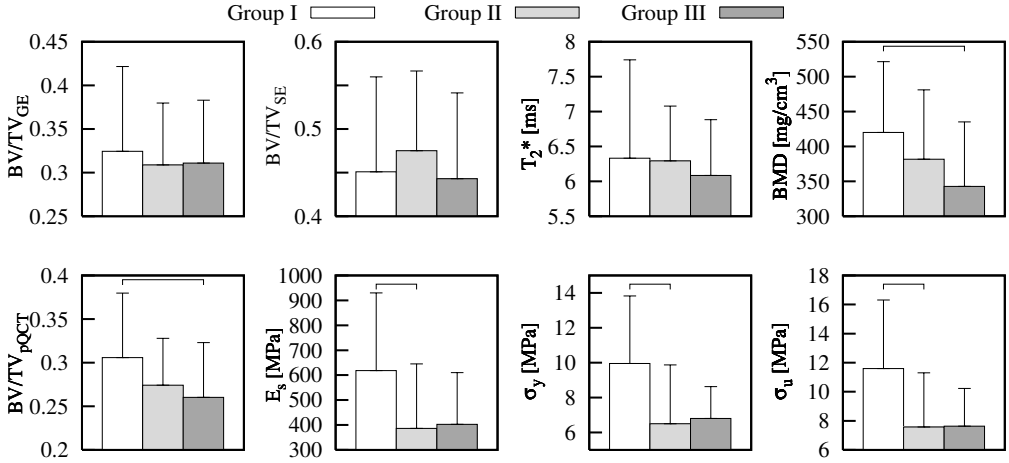

Figure 7.8: Mean ± SD values for bone variables divided into three groups according to their Mankin Score. Statistical difference between groups ($p < 0.05$) is denoted with brackets.

7.3 Interrelations of bone and cartilage properties

The mechanical properties of cartilage and bone did not correlate significantly with each other despite a similar trend in line with the extent of cartilage degeneration. The correlation coefficient between T_2^* of bone and dGEMRIC was significant at both field strengths for superficial tissue ($r = 0.32$, $p < 0.01$ at 1.5 T and $r = 0.46$, $p < 0.01$ at 9.4 T) as well as for bulk tissue ($r = 0.27$, $p < 0.05$ at 1.5 T and $r = 0.44$, $p < 0.01$ at 9.4 T). T_2^* also correlated significantly with superficial T_2 at 1.5 T ($r = -0.31$, $p < 0.01$). Superficial dGEMRIC at 1.5 T correlated significantly also with BMD ($r = -0.32$, $p < 0.01$). Correlation coefficients within group I were significantly higher than within all samples between superficial dGEMRIC at 1.5 T and BMD ($p < 0.01$), Young's modulus of cartilage and BMD ($p < 0.05$) and $E_{s,c}$ and T_2^* ($p < 0.05$).

7.4 Spectroscopic NMR measurements

7.4.1 Spectroscopic T_2, CP-T_2 and $T_{1\rho}$ of trabecular bone

R_2 (i.e. $1/T_2$) varied between 10 and 17 s^{-1} (mean±SD 14±2 s^{-1}) for fat and between 24 and 31 s^{-1} (28±2 s^{-1}) for water (Figure 7.9a). Compared to R_2, CP-R_2 was significantly lower for both fat and water. For water, the difference between CP-R_2 and R_2 was significantly higher than for fat. These findings are consistent with the significant contribution made by diffusion in the local susceptibility field gradients to T_2 measurements. R_2 values measured with varying τ_{CP} and four 180°pulses (4P-R_2), and with 0°pulses (DP-R_2) were not significantly different from R_2 measured with double spin echo (SE-R_2), indicating that there is no significant $T_{2\rho}$ contribution to the signal during the pulse sequence. Mean diffusivity was (6.8±2.2)·10^{-6} mm^2/s for fat, and (1.4±0.8)·10^{-4} mm^2/s for water, and mean magnitudes of gradient fields calculated using (4.19) were (7.4±0.9)·10^{-5} T/m and (6.6±0.3)·10^{-6} T/m for fat and

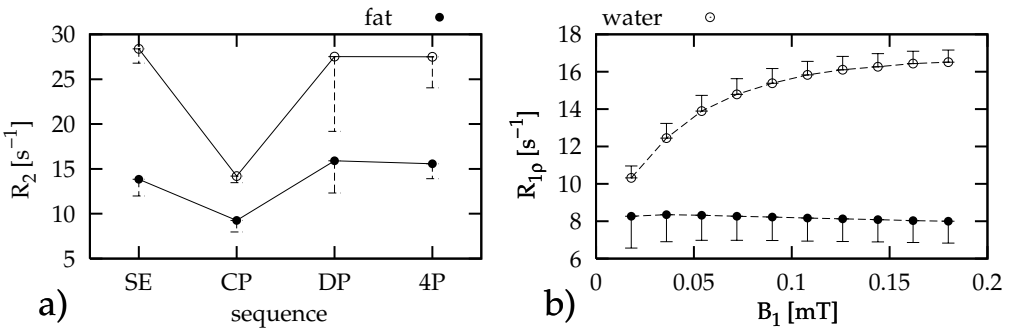

Figure 7.9: (a) R_2 of fat and water components of bone marrow obtained with different pulse sequences. SE-spin echo, CP-Carr-Purcell, DP-dummy (0°) pulses inserted (see Fig. 2), 4P-four 180°pulses with different intervals. (b) $T_{1\rho}$ dispersion for fat and water at on-resonance frequencies.

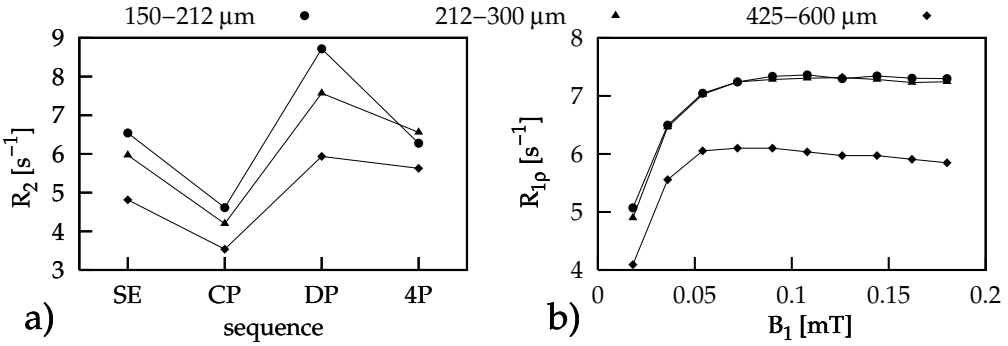

Figure 7.10: Results for glass-bead phantoms with interstitials filled with turnip rape oil. (a) Mean R_2 values of the phantoms obtained with different pulse sequences. (b) $T_{1\rho}$ dispersion.

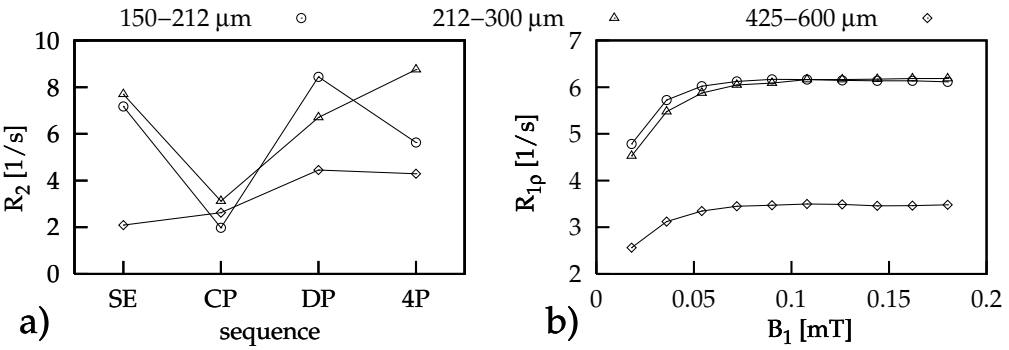

Figure 7.11: Results for glass-bead phantoms with interstitials filled with $CuSO_4$-adulterated water. (a) Mean R_2 values of the phantoms obtained with different pulse sequences. (b) $T_{1\rho}$ dispersion.

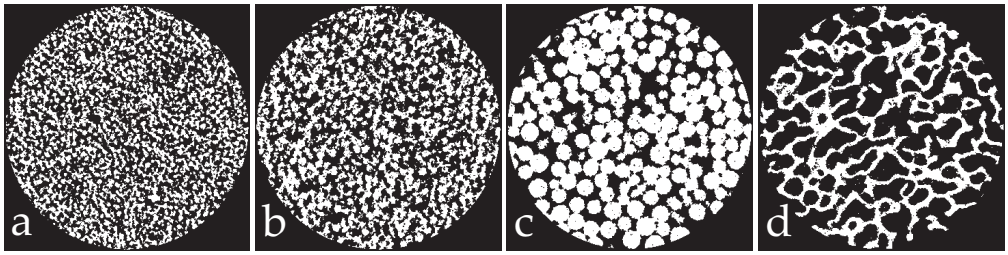

Figure 7.12: Binarized microCT images of phantoms of glass beads with diameters of (a) 150-212 µm, (b) 212-300 µm and (c) 425-600 µm, and (d) bovine trabecular bone (mean trabecular thickness 138 µm).

Table 7.6: MicroCT parameters calculated for glass bead phantoms and mean±SD values for the bone samples.

	BV/TV [%]	Tb.Th [µm]	Tb.Sp [µm]	Tb.N [1/µm]	SMI
150-212 µm	35.0	104.3	593.5	$3.7{\cdot}10^{-3}$	0.419
212-300 µm	33.5	128.1	635.6	$3.1{\cdot}10^{-3}$	0.662
425-600 µm	46.7	418.9	867.7	$1.9{\cdot}10^{-3}$	-0.421
bone	30.8±3.6	163.8±28.7	814.0±58.5	$(1.9\pm0.3){\cdot}10^{-3}$	-1.502±1.795

water, respectively. $R_{1\rho,\mathrm{f}}$ did not vary significantly as a function of B_1, whereas $R_{1\rho,\mathrm{w}}$ revealed an increasing trend (Figure 7.9b).

For glass bead phantoms, the trend of R_2 for oil was similar to that of the fat component of bone marrow but the absolute values were lower, and the relative values of 4P-R_2 were smaller (Figure 7.10a). $R_{1\rho}$ showed an increasing trend as a function of B_1 for all bead sizes, with the smallest values for the largest beads which had a diameter of 425-600 µm (Figure 7.10b). The results were similar for water (Figure 7.11).

7.4.2 Spectroscopic NMR parameters and structural properties

Binarized images of glass bead phantoms and trabecular bone are shown in Figure 7.12. All phantoms had greater BV/TV than the mean value of bone samples (Table 7.6). The thickness of the trabeculae of bone samples was between that of the middle size and largest beads, and trabecular separation of bone samples was greater than in the phantoms except for the largest beads. SMI of phantoms was quite different from that of bone, and the SMI of bone displayed considerable variation. The closest possible packing scheme, namely hexagonal close packing, of identical spheres provides the volume fraction of 74 % [91]. In the case of the phantoms, the variation in glass bead diameters and the interstitial fluid decreased the volume fraction.

For fat, significant linear correlations ($p<0.01$) were established between SE-R_2 and SMI ($r = 0.83$), and between CP-R_2 and Tb.Th ($r = 0.77$) (see study IV, Table 2). The magnitude of the susceptibility gradients correlated significantly ($p<0.01$) with SMI ($r = 0.83$ for fat and $r = 0.64$ for water). $R_{1\rho,\mathrm{f}}$ correlated significantly with Tb.Th, Tb.N. and SMI at all B_1 strengths, whereas linear correlations were established between

$R_{1\rho,\mathrm{w}}$ and Tb.Th at the five smallest B_1 strengths, and between $R_{1\rho,\mathrm{w}}$ and Tb.Sp for all B_1 strengths except for 0.18 mT. The strongest correlations were found between $R_{1\rho,\mathrm{f}}$ and SMI. In the fat specimens, the correlation coefficients did not vary significantly as a function of B_1 strength.

CHAPTER VIII

Discussion

8.1 Quantitative MRI and articular cartilage

A significant difference in T_2 between the two field strengths was observed, however the depth-wise profiles displayed a similar shape, with an offset of about 20 ms. This probably relates to the different orientation of the sample, in particular to the collagen network, which is known to affect significantly the T_2 relaxation time via the dipolar interaction [201, 202]. When cartilage surface is oriented parallel to the B_0 field, the collagen fibers of radial zone are perpendicular to the B_0, which considerably diminishes the nuclear dipolar interaction compared to the orientation with the articular surface perpendicular to the B_0, increasing the signal detected from the deep cartilage. Since the radial zone is the thickest layer in cartilage, this may partly explain the difference in T_2 between the field strengths. The thickness of the superficial layer is smaller than the pixel size applied at 1.5 T, thus the effect of the most superficial collagen fibers parallel to the B_0 is limited. Formerly, the dependence of T_2 on collagen orientation has been confirmed by polarized light microscopy [203, 142], and the collagen-related role of T_2 has been shown by enzymatic digestions [140]. T_2 at 1.5 T was measured using a multiecho sequence, which has been reported to increase the measured T_2 relaxation time [112, 125].

Also dGEMRIC showed a significant difference between the field strengths but the depth-wise profiles were not as similar as T_2 profiles. T_1 of cartilage is considered to be insensitive to B_0 direction [70], thus the different sample orientation should not significantly affect the results. Measurements at 9.4 T were conducted using detached cartilage plugs, thus the diffusion of the contrast agent into deep cartilage may have been more efficient than for intact patellae measured at 1.5 T. The correlation times associated to T_1 at 1.5 T and 9.4 T are significantly different [48], which may partly explain the different behavior of Gd-DTPA^{2-}-enhanced T_1 at different field strengths.

The correlation of the mechanical properties with MRI parameters varied from poor to excellent among the test locations and parameters, with dGEMRIC showing the highest correlation coefficient at 9.4 T, whereas T_2 yielded higher correlations at 1.5 T. These results suggest that the dynamic mechanical properties of cartilage, related to the collagen network, may be assessed also at clinically relevant field strengths, whereas the static compressive strength, primarily modulated by PGs, can be more closely evaluated by dGEMRIC at higher field strengths. This may partially be due

to the different effects of relaxivity at different field strengths. At 8.5 T, the relaxivity of articular cartilage has been reported to be similar to that of saline and to be insensitive to compression or trypsinization [39]. The present results suggest that the contribution of relaxivity varying as a function of macromolecular content [177] is more significant at lower field strengths.

The linear correlation coefficients between MRI and mechanical parameters were not as high as reported earlier for animal tissue at high field strengths [139, 143]. This may be due in part to the heterogeneous sample population, but also suggests that the mechanical properties of degenerated cartilage cannot satisfactorily be explained by only one MRI parameter. It seems that enzymatic digestion of a single structural component can significantly modulate the mechanical properties of normal cartilage, but in degenerated tissue, the interaction between different constituents and the mechanical properties is much more complex. T_2 relaxation time was measured in the presence of Gd-DTPA^{2-} for a consecutive measurement of T_2 and dGEMRIC. The contrast agent, however, has a minimal effect on T_2 relaxation time at low equilibrating concentrations, such as the one used in this work [138]. The present results also show that T_2 in the presence of Gd-DTPA^{2-} is able to assess the mechanical properties of cartilage.

Mechanical properties of articular cartilage demonstrate significant topographical variation [79, 98]. The topographical variation of T_2 at both field strengths was similar to that of $E_{s,c}$, and the linear correlations between T_2 and $E_{s,c}$ were significant both at 1.5 T and 9.4 T. dGEMRIC showed a very weak topographical variation that did not follow the variation in the mechanical moduli. The PG content has been reported to decrease with cartilage degeneration [189, 119] and vary as a function of the loading conditions [190]. The variation in loading conditions between different joint surfaces or topographical locations and differently adapted macromolecular composition can further complicate the use of a single MRI parameter as a surrogate marker for mechanical properties [165]. However, linear correlations within some of the individual test sites were high and significant, while at some sites no significant correlations existed. Similar results on human knee cartilage have been previously reported [97].

The correlation between T_2 and collagen content was weaker than reported earlier [140]. This may also be related to different sample orientations, as discussed above. T_2 has been reported to be sensitive also to PG changes in porcine articular cartilage at 2.35 T with articular surface oriented along the direction of the B_0 field [193]. When applying this orientation, the collagen fibers in deep layer of articular cartilage, the thickest layer, are perpendicular to the B_0 field which considerably diminishes the nuclear dipolar interaction compared to the orientation with articular surface perpendicular to the B_0 field. Such an orientation may lead to a diminished contribution of collagen-related relaxation mechanisms and other, PG-related mechanisms may play a more important role. Hence, this might partially explain the association between T_2 at 1.5 T and PG content.

At 1.5 T, T_2 relaxation time of cartilage increased significantly as the extent of degeneration, whereas T_2 measured at 9.4 T showed a similar trend, but it was statistically insignificant. On the other hand, dGEMRIC at both field strengths showed a decreasing trend with degeneration but changes were significant only at 9.4 T. Increased T_2 values have been earlier related to advanced degeneration in human cartilage [155, 38, 40] and rhesus macaque [50], however, both increase [140] and decrease

[126] in T_2 has been reported in a study utilizing enzymatic digestion.

As far as is known, this study is the first histological verification of relationship between dGEMRIC and OA-related changes in human articular cartilage. While dGEMRIC revealed a decreasing trend with degeneration, these differences were not statistically significant between groups with no or minimal and moderate degeneration at either field strength. This suggests that dGEMRIC, unlike T_2 relaxation time, may not be sensitive enough to detect the earliest degenerative changes. However, the histological results show that PG content is significantly different between all groups but the difference in collagen content is not significant between sample groups with no or minimal degeneration and moderate degeneration. This is in disagreement with the current understanding of the relation of the present quantitative MRI techniques and cartilage composition and structure, and implies that the relaxation processes in cartilage are more complicated than currently understood.

The 1.5 T MRI measurements were conducted using intact patellae, whereas for the 9.4 T experiments and biomechanical testing, cartilage disks without subchondral bone were prepared. After isolation from bone and surrounding cartilage, samples occasionally experience swelling and curling [170], which may alter the macromolecular density and other material properties and thus affect the results, especially in the degenerated samples. Previous results also indicate that while the orientation of the collagen fibers is preserved also in detached cartilage disks, the collagen network density may be considerably decreased [85]. Mechanical testing of the deformed cartilage samples under unconfined conditions increases the measurement uncertainty, and some of the samples had to be excluded for this reason. Further, a thin layer of the deepest cartilage may have been left attached to the bone surface during sample preparation, which could bias the biomechanical measurements. Although the collagen network and thus the mechanical properties of cartilage may have been altered while detaching the disks, unconfined compression is considered to provide an accurate technique to measure intrinsic tissue properties. The only measurement geometry applicable for intact articular surface, namely indentation, necessitates more complex modeling approaches to extract material parameters. Moreover, the size of 9.4 T magnet bore required small sample size.

All the samples were pooled for most of the correlation analysis. This may affect the results via interdependencies between the samples originating from the same patella. While calculating the correlation coefficients for individual measurement sites, varying results were obtained for different sites. Statistical analyses also revealed significant differences in T_2 and elastic moduli of cartilage between different sites.

8.2 Quantitative NMR and trabecular bone

Quantitative MRI of trabecular bone

The correlation coefficients between BMD and MRI-derived bone volume fractions were modest but similar to those reported in previous works [107, 109]. It has been previously reported that correlation coefficients between R_2^* and BMD differ considerably at different anatomical locations [81, 107]. In addition, R_2^* is reported to depend also on trabecular orientation [33, 75].

Bone mineral density seemed to assess the mechanical properties of trabecular bone more accurately than R_2^*. It has been shown that due to the anisotropic trabecular architecture, there is a variable relationship between elastic modulus and bone density over different anatomical locations [131]. It has also been shown that there is no uniform trabecular orientation over the entire human patella [153, 182], the tissue of interest in the present study. The σ_y is suggested to be less dependent on trabecular orientation [183], and both R_2^* and BMD correlated indeed more strongly with σ_y than with $E_{s,b}$. However, based on these reports, the results of the current study cannot be directly generalized to other anatomical sites.

The assessment of mechanical properties was improved when BV/TV_{GE} and R_2^* relaxation rate were combined into a linear regression model, compared to those of BV/TV_{SE}, BV/TV_{GE} and R_2^* alone, as also reported in earlier studies [75, 149]. Contrary to the MRI results, combining BMD and BV/TV_{pQCT} into a linear model did not improve the correlation with mechanical properties. The highest correlation with the mechanical properties was achieved with BV/TV_{pQCT}, but the differences between imaging modalities were not statistically significant. This is evidence of the feasibility of using MRI-derived variables in the assessment of the mechanical and structural properties of human trabecular bone. Further work is needed to determine the optimal combination of different variables and to analyse the effect of trabecular anisotropy at different anatomical locations.

Bone mineral density decreased along with osteoarthritic degeneration of cartilage. This is contradictory to previous results from histological evaluation of human samples [17, 122]. This may be due to a different choice of region of interest. In the present study, dense subchondral bone was omitted from analyzed regions since it provides a negligible NMR signal, and this might have excluded a possible sclerosis. Some samples showed sclerotic changes near the subchondral plate in pQCT images. The decrease in mineral density of trabecular bone may partially be explained by age-related changes, such as osteoporosis.

Mechanical properties of articular cartilage and trabecular bone revealed a similar decreasing trend as the extent of cartilage degeneration increased but there were no significant linear correlations between these two parameters. Nonetheless, the MRI parameters of cartilage and bone were correlated. This suggests that the chain of degenerative changes is complex and will require further evaluation. Some of the linear associations were higher when only the samples with no or minimal degeneration were included. This result, together with the findings of earlier studies using enzymatic digestion, suggests that quantitative MR parameters reflect the mechanical properties of healthy tissue but the actual degeneration affects the tissue in a complex way. Additionally, there might be several subprocesses in OA development and thus quantitative parameters sensitive to single joint tissue component cannot detect all degenerative changes.

The difference in the in-plane resolutions between different imaging modalities has only minor significance in bone mineral density and R_2^* measurements as bulk values were calculated by averaging the values over the entire region of interest. However, the accuracy of the determination of bone volume fraction may be affected by limited resolution. The nominal resolutions of pQCT and MRI resolution were similar (200 µm and 234 µm, respectively), both being over twice the average trabecular thickness. The resolution in the third direction is dictated by the slice thickness. For

pQCT and MRI, the slice thicknesses were 0.5 mm and 1 mm, respectively. This difference may affect the accuracy of the calculations. BV/TV_{pQCT} was determined using a single slice, whereas BV/TV_{GE} was calculated from VOI consisting of ROIs in seven consecutive slices. It has been shown that the bone volume fraction measured by microCT with a pixel size considerably smaller than the size of the trabeculae is able to assess the mechanical properties accurately [187], but that also a more coarse resolution can be used for assessing the bone volume fraction [100]. As the spin densities are averaged over a larger volume of interest, the calculation of bone volume fraction using the spin echo technique is quite independent of the resolution. This might be a feasible method; however the lack of a significant correlation with mechanical properties is a considerable drawback. The use of an oil phantom with properties as close to those of human fat tissue as possible might improve the correlation. In addition to resolution issues, images acquired using the traditional gradient echo sequence may not be ideal for calculation of the structural parameters of trabecular bone. Better results have recently been obtained using steady-state free precession (SSFP) [9, 195] and fast large-angle spin echo (FLASE) [111, 195] sequences.

The ideal specimen length-diameter ratio for mechanical testing would be much larger than 1:1 to reduce boundary effects occurring at the ends of the specimen [185]. However, the physical dimensions of the patellae did not allow the isolation of longer samples from the predefined locations and the diameter of the cylinders could not be diminished because the integrity of the trabecular grid would have been excessively decreased. These boundary effects may in part account for the weaker linear correlations between the mechanical properties and BMD and partly between mechanical properties and MRI variables than previously reported [20, 75, 107].

Spectroscopic NMR of trabecular bone

Diffusion in local field gradients generated by magnetic susceptibility difference between bone and bone marrow is the evident explanation for the correlation between T_2 relaxation and structural parameters of bone. This is supported by the fact that R_2 was significantly decreased when the delay between refocusing pulses was decreased, and that this decrease was much more pronounced for water than for lipids, reflecting their different diffusion properties. Interestingly, water and lipids probe a clearly different diffusion regime. Fat T_2 showed significant correlation with Tb.Th, while water T_2 did not. This is likely because of higher motional averaging for water than for fat. The apparent magnitude of local gradient field calculated from T_2 measurements with different τ_{CP} was smaller for water than for fat. This might also be explained by motional averaging. The assumption that there is a linear field gradient may also influence the result, as in reality, the gradient shape is more complex. Also, strong background gradients in the sample may cause bias to the measured diffusion values.

Theoretical models for $T_{1\rho}$ relaxation are discussed in study IV. The present data reveal a significant correlation between both lipid and water $T_{1\rho}$ values and structural bone parameters, evidence of a possible contribution of diffusion to the macroscopic field gradients. Decreased $R_{1\rho}$ with low B_1 values was observed for water. It should be noted that this kind of $T_{1\rho}$ dispersion is opposite to that usually obtained from soft tissue where the dipolar interaction is the governing relaxation mechanism. While

the presented description of observed $T_{1\rho}$ changes remains speculative, it provides some insight into possible mechanisms. However, more complete theoretical formalism with simulations is required to better understand the behaviour of $T_{1\rho}$ relaxation under this kind of experimental conditions.

The current measurements were performed at room temperature. At body temperature, diffusion is faster which will influence relaxation and averaging effects. On the other hand, local field gradients are reduced in the lower magnetic field strengths (1.5-3 T) currently used in hospitals. These two effects may partially compensate for each other, and considering the different diffusion regime probed by water and fat, it is likely that an optimal combination of local field gradient strength, diffusional displacement and experimental parameters (B_1, τ_{CP}) can be found. At birth, nearly 100% of bone marrow is red marrow, but the proportion of yellow marrow increases with aging [35]. Therefore, it is essential to perform validation using cadaver samples with different ages and osteoporotic stages. Compared to the current morphometric methods, the acquisition of spectroscopic data is fast, and its further analysis is simpler since no binarization or complex post-processing is required. In general, there are no obstacles to implement this method clinically, since spectroscopic sequences are available for clinical scanners, and $T_{1\rho}$ measurements have been conducted for joints within acceptable SAR levels [156]. However it may be difficult to find a coil suitable for $T_{1\rho}$ measurements in locations relevant to osteoarthritis or osteoporosis, such as the hip.

8.3 Quantitative MRI in OA detection

T_2 appears to provide feasible tools for assessing cartilage properties also at clinical field strengths, although it cannot fully characterize the mechanical properties of cartilage. T_2 mapping can reflect some of the topographical variation in mechanical properties of human cartilage at both field strengths, while dGEMRIC exhibits significant correlations with mechanical parameters within individual topographical locations at high field strengths. These results will likely have relevance when interpreting quantitative MRI measurements in vivo.

Based on the present results, the characteristic changes during osteoarthritis include a decrease in elastic moduli of bone and cartilage, a reduction in the PG and collagen contents of cartilage and bone mineral density and a decrease in volume fraction of trabecular bone. The current results suggest that parallel changes in cartilage and bone in degenerative joint disease can be detected with quantitative MRI techniques, particularly T_2 of articular cartilage and linear combination of R_2^* and $\mathrm{BV/TV_{GE}}$ of trabecular bone. Even though previous and present results suggest that T_2 is sensitive to more than one structural component of articular cartilage, it does seem that T_2 can detect the different stages of osteoarthritis.

It is noteworthy that human OA is considered to be more complex than any digestion model selectively affecting specific cartilage components and that many tissues are involved in the degenerative processes. The results from these and earlier studies suggest that the relaxation mechanisms in articular cartilage are complex and may be different at different field strengths, warranting further studies.

8.4 Future objectives

Based on the present results, several issues are proposed for aims of the further studies:

The present results were obtained by investigating human patellae. Due to the different structure, composition and loading conditions, these results may not be generalized to other sites. Similar studies should be performed using other articular surfaces that are subject to osteoarthritic changes to evaluate topographical variations and interrelationships of different parameters.

The relation of T_2 and different degeneration mechanisms needs to be clarified to find an explanation for the increasing and decreasing T_2 values seen during degeneration and the correlation between T_2 and different cartilage constituents.

The relaxation mechanisms behind the dGEMRIC technique seem to be dependent on field strength, and the method needs further validation in clinically applied field strengths. In addition, the diffusion of the contrast agent into cartilage also requires further study, particularly in the in vivo situation to improve the estimation of contrast agent concentration in cartilage.

The spectroscopic method for assessment of the trabecular structure is introduced here with the first results obtained in vitro using bovine specimens. The method still needs further study with appropriate modeling and validation, first in vitro and finally in vivo in a clinical setup.

CHAPTER IX

Summary and conclusions

In the present study, quantitative MRI and MRS methods for characterizing the structure and mechanical properties of trabecular bone were validated against established reference methods, such as mechanical testing, histological methods, peripheral quantitative computed tomography and microCT measurements. The main conclusions from the present study are summarized as follows:

1. T_2 relaxation times of articular cartilage display similar trends at different field strengths, whereas the trends of dGEMRIC at different field strengths are partly contradictory.

2. T_2 provides the best correlation with compressive stiffness of articular cartilage at 1.5 T, whereas dGEMRIC offers the best correlation at 9.4 T.

3. T_2 relaxation time is able to assess the compressive stiffness of articular cartilage also in the presence of Gd-DTPA^{2-} contrast agent.

4. At 1.5 T, T_2 relaxation time can discern different stages of cartilage degeneration, while dGEMRIC seems to be too insensitive to detect the earliest degenerative changes in the composition of cartilage. At 9.4 T, dGEMRIC is able to detect advanced degeneration of cartilage, whereas T_2 reveals no significant differences between samples with different degrees of degeneration.

5. Combination of R_2^* and bone volume fraction as determined by MRI provides a more accurate assessment of both the mechanical properties and BMD of trabecular bone than R_2^*, BV/TV$_{\mathrm{SE}}$ or BV/TV$_{\mathrm{GE}}$ alone.

6. There are significant relations between MRI variables of bone and cartilage indicating parallel changes during degeneration. The degenerative changes during OA seem to be complex, and no single MR parameter seems to be adequate in characterizing them.

7. Spectroscopically determined T_2, Carr-Purcell T_2 and $T_{1\rho}$ for water and fat may be feasible for the assessment of the trabecular structure.

[1] *Osteoarthritis. NIH publication No. 06-4617*. National Institute of Health, 2002.

[2] H. A. Alhadlaq and Y. Xia. Modifications of orientational dependence of microscopic magnetic resonance imaging T_2 anisotropy in compressed articular cartilage. *J Magn Reson Imaging*, 22(5):665–673, 2005.

[3] S. Allein, S. Majumdar, E. De Bisschop, D. C. Newitt, R. Luypaert, and H. Eisendrath. In vivo comparison of MR phase distribution and $1/T_2^*$ with morphologic parameters in the distal radius. *J Magn Reson Imaging*, 7(2):389–393, 1997.

[4] Anonymous. Consensus development conference: diagnosis, prophylaxis and treatment of osteoporosis. *Am J Med*, 94:646–650, 1993.

[5] J. P. Arokoski, M. H. Arokoski, P. Vainio, H. Kröger, and J. S. Jurvelin. Estimation of femoral head bone density using magnetic resonance imaging: comparison between men with and without hip osteoarthritis. *J Clin Densitom*, 7(2):183–191, 2004.

[6] M. H. Arokoski, J. P. Arokoski, P. Vainio, L. H. Niemitukia, H. Kröger, and J. S. Jurvelin. Comparison of DXA and MRI methods for interpreting femoral neck bone mineral density. *J Clin Densitom*, 5(3):289–296, 2002.

[7] A. Aromaa and S. Koskinen (Ed.). *Health and functional capacity in Finland. Baseline results of the Health 2000 health examination survey.*, volume B3/2002 of *Publications of the National Public Health Institute*. Helsinki, 2002.

[8] D. L. Bader and G. E. Kempson. The short-term compressive properties of adult human articular cartilage. *Biomed Mater Eng*, 4(3):245–256, 1994.

[9] S. Banerjee, E. T. Han, R. Krug, D. C. Newitt, and S. Majumdar. Application of refocused steady-state free-precession methods at 1.5 and 3 T to in vivo high-resolution MRI of trabecular bone: simulations and experiments. *J Magn Reson Imaging*, 21(6):818–825, 2005.

[10] A. Bashir, M. L. Gray, and D. Burstein. Gd-DTPA^{2-} as a measure of cartilage degradation. *Magn Reson Med*, 36(5):665–673, 1996.

[11] A. Bashir, M. L. Gray, J. Hartke, and D. Burstein. Nondestructive imaging of human cartilage glycosaminoglycan concentration by MRI. *Magn Reson Med*, 41(5):857–865, 1999.

[12] A. Benninghoff. Form und Bau der Gelenkknorpel in ihren Beziehungen zur Function. erste Mitteilung: die modellierenden und formerhaltenden Faktoren

des Knorpelreliefs. *Z Anat*, 76:43–63, 1925.

[13] H.J.C. Berendsen. Nuclear magnetic resonance study of collagen hydration. *J Chem Phys*, 36(12):3297–3305, 1962.

[14] O. Beuf, S. Ghosh, D. C. Newitt, T. M. Link, L. Steinbach, M. Ries, N. Lane, and S. Majumdar. Magnetic resonance imaging of normal and osteoarthritic trabecular bone structure in the human knee. *Arthritis Rheum*, 46(2):385–393, 2002.

[15] O. Beuf, D. C. Newitt, L. Mosekilde, and S. Majumdar. Trabecular structure assessment in lumbar vertebrae specimens using quantitative magnetic resonance imaging and relationship with mechanical competence. *J Bone Miner Res*, 16(8):1511–1519, 2001.

[16] S. J. Blackband and E. Hsu. Magnetization transfer contrast magnetic resonance imaging. In R. J. Gillies, editor, *NMR in physiology and biomedicine*, pages 119–135. Academic Press, Inc., 1994.

[17] D. Bobinac, J. Spanjol, S. Zoricic, and I. Maric. Changes in articular cartilage and subchondral bone histomorphometry in osteoarthritic knee joints in humans. *Bone*, 32(3):284–290, 2003.

[18] A. Borthakur, E. Mellon, S. Niyogi, W. Witschey, J. B. Kneeland, and R. Reddy. Sodium and $T_{1\rho}$ MRI for molecular and diagnostic imaging of articular cartilage. *NMR Biomed*, 19(7):781–821, 2006.

[19] A. Borthakur, E. M. Shapiro, J. Beers, S. Kudchodkar, J. B. Kneeland, and R. Reddy. Sensitivity of MRI to proteoglycan depletion in cartilage: comparison of sodium and proton MRI. *Osteoarthritis Cartilage*, 8(4):288–293, 2000.

[20] T. B. Brismar, T. Hindmarsh, and H. Ringertz. Experimental correlation between T_2^* and ultimate compressive strength in lumbar porcine vertebrae. *Acad Radiol*, 4(6):426–430, 1997.

[21] H. Brown and R. Prescott. *Applied Mixed Models in Medicine*. John Wiley & Sons, Inc., New York, 2001.

[22] M.A. Brown and R.C. Semelka. *MRI. Basic principles and applications*. Wiley-Liss, Inc., New York, 1995.

[23] R.G. Bryant. The dynamics of water-protein interactions. *Annu. Rev. Biophys. Biomol. Struct.*, 25:29–53, 1996.

[24] J.A. Buckwalter and H.J. Mankin. Articular cartilage, Part II: Degeneration and osteoarthrosis, repair, regeneration, and transplantation. *J Bone Joint Surg Am*, 79(4):612–632, 1997.

[25] D. B. Burr. The contribution of the organic matrix to bone's material properties. *Bone*, 31(1):8–11, 2002.

[26] D. Burstein, J. Velyvis, K. T. Scott, K. W. Stock, Y. J. Kim, D. Jaramillo, R. D. Boutin, and M. L. Gray. Protocol issues for delayed Gd(DTPA)$^{2-}$-enhanced MRI (dGEMRIC) for clinical evaluation of articular cartilage. *Magn Reson Med*, 45(1):36–41., 2001.

[27] M. D. Buschmann, J. Soulhat, A. Shirazi-Adl, J. S. Jurvelin, and E. B. Hunziker. Confined compression of articular cartilage: linearity in ramp and sinusoidal tests and the importance of interdigitation and incomplete confinement. *J Biomech*, 31(2):171–178., 1998.

[28] N. P. Camacho, P. West, P. A. Torzilli, and R. Mendelsohn. FTIR microscopic imaging of collagen and proteoglycan in bovine cartilage. *Biopolymers*, 62(1):1–

8, 2001.

[29] C. E. Cann. Quantitative CT for determination of bone mineral density: a review. *Radiology*, 166(2):509–522, 1988.

[30] S. Capuani, F. Curzi, F. M. Alessandri, B. Maraviglia, and A. Bifone. Characterization of trabecular bone by dipolar demagnetizing field MRI. *Magn Reson Med*, 46(4):683–689, 2001.

[31] H.Y. Carr and E.M. Purcell. Effects of diffusion on free precession in nuclear magnetic resonance experiments. *Phys Rev*, 94(3):630–638, 1954.

[32] D. R. Carter and W. C. Hayes. The compressive behavior of bone as a two-phase porous structure. *J Bone Joint Surg Am*, 59(7):954–962, 1977.

[33] H. Chung, F. W. Wehrli, J. L. Williams, and S. D. Kugelmass. Relationship between NMR transverse relaxation, trabecular bone architecture, and strength. *Proc Natl Acad Sci USA*, 90(21):10250–10254, 1993.

[34] D. H. Collins and T. F. McElligot. Sulphate ($^{35}SO_4$) uptake by chondrocytes in relation to histological changes in osteoarthritic human articular cartilage. *Ann Rheum Dis*, 19:318–330, 1960.

[35] J. E. Compston. Bone marrow and bone: a functional unit. *J Endocrinol*, 173(3):387–394, 2002.

[36] B. Cowan. *Nuclear magnetic resonance and relaxation*. Cambridge University Press, Cambridge, 1997.

[37] B. J. Dardzinski, T. J. Mosher, S. Li, M. A. Van Slyke, and M. B. Smith. Spatial variation of T_2 in human articular cartilage. *Radiology*, 205(2):546–550, 1997.

[38] E David-Vaudey, S. Ghosh, M. Ries, and S. Majumdar. T_2 relaxation time measurements in osteoarthritis. *Magn Reson Imaging*, 22:673–682, 2004.

[39] K. M. Donahue, D. Burstein, W. J. Manning, and M. L. Gray. Studies of Gd-DTPA relaxivity and proton exchange rates in tissue. *Magn Reson Med*, 32(1):66–76, 1994.

[40] T.C. Dunn, Y. Lu, H. Jin, M. Ries, and S. Majumdar. T_2 relaxation time of cartilage at MR imaging: Comparison with severity of knee osteoarthritis. *Radiology*, 232(2):592–598, 2004.

[41] U. Duvvuri, R. Reddy, S. D. Patel, J. H. Kaufman, J. B. Kneeland, and J. S. Leigh. $T_{1\rho}$-relaxation in articular cartilage: effects of enzymatic degradation. *Magn Reson Med*, 38(6):863–867, 1997.

[42] F. Eckstein, D. Burstein, and T. M. Link. Quantitative MRI of cartilage and bone: degenerative changes in osteoarthritis. *NMR Biomed*, 19(7):822–854, 2006.

[43] S. J. Erickson, R. W. Prost, and M. E. Timins. The "magic angle" effect: background physics and clinical relevance. *Radiology*, 188(1):23–25, 1993.

[44] D.R. Eyre, M. A. Weis, and J-J. Wu. Articular cartilage collagen: an irreplaceable framework? *Eur Cell Mater*, 12:57–63, 2006.

[45] M. A. Fernandez-Seara, H. K. Song, and F. W. Wehrli. Trabecular bone volume fraction mapping by low-resolution MRI. *Magn Reson Med*, 46(1):103–113, 2001.

[46] M. A. Fernandez-Seara, S. L. Wehrli, M. Takahashi, and F. W. Wehrli. Water content measured by proton-deuteron exchange NMR predicts bone mineral density and mechanical properties. *J Bone Miner Res*, 19(2):289–296, 2004.

[47] E. Fragonas, V. Mlynarik, V. Jellus, F. Micali, A. Piras, R. Toffanin, R. Rizzo, and F. Vittur. Correlation between biochemical composition and magnetic resonance appearance of articular cartilage. *Osteoarthritis Cartilage*, 6(1):24–32, 1998.

[48] G.D. Fullerton. Physiologic basis of magnetic relaxation. In D.D. Stark and W.G. Bradley, editors, *Magnetic resonance imaging*, pages 36–54. Bradley, Baltimore, 1992.

[49] D.G. Gadian. *NMR and its applications to living systems*. Oxford University Press Inc., New York, 1995.

[50] H. K. Gahunia, C. Lemaire, P. S. Babyn, A. R. Cross, M. J. Kessler, and K. P. Pritzker. Osteoarthritis in rhesus macaque knee joint: quantitative magnetic resonance imaging tissue characterization of articular cartilage. *J Rheumatol*, 22(9):1747–1756, 1995.

[51] L.P. Gartner and J.L. Hiatt. *Color book of histology, 2nd edition*. W.B. Saunders Comp., Philadelphia, 2001.

[52] M. Garwood and L. DelaBarre. The return of the frequency sweep: designing adiabatic pulses for contemporary NMR. *J Magn Reson*, 153(2):155–177, 2001.

[53] K. Gelse, S. Soder, W. Eger, T. Diemtar, and T. Aigner. Osteophyte development–molecular characterization of differentiation stages. *Osteoarthritis Cartilage*, 11(2):141–148, 2003.

[54] G. E. Gold, T. F. Besier, C. E. Draper, D. S. Asakawa, S. L. Delp, and G. S. Beaupre. Weight-bearing MRI of patellofemoral joint cartilage contact area. *J Magn Reson Imaging*, 20(3):526–530, 2004.

[55] S. Grampp, S. Majumdar, M. Jergas, P. Lang, A. Gies, and H. K. Genant. MRI of bone marrow in the distal radius: in vivo precision of effective transverse relaxation times. *Eur Radiol*, 5(1):43–48, 1995.

[56] S. Grampp, S. Majumdar, M. Jergas, D. Newitt, P. Lang, and H. K. Genant. Distal radius: in vivo assessment with quantitative MR imaging, peripheral quantitative CT, and dual X-ray absorptiometry. *Radiology*, 198(1):213–218, 1996.

[57] M. L. Gray, D. Burstein, L. M. Lesperance, and Gehrke Lee. Magnetization transfer in cartilage and its constituent macromolecules. *Magn Reson Med*, 34(3):319–325, 1995.

[58] H. I. Gröhn, S. Michaeli, M. Garwood, R. A. Kauppinen, and O. H. Grohn. Quantitative $T_{1\rho}$ and adiabatic Carr-Purcell T_2 magnetic resonance imaging of human occipital lobe at 4 T. *Magn Reson Med*, 54(1):14–19, 2005.

[59] H. Gries and H. Miklautz. Some physicochemical properties of the gadolinium-DTPA complex, a contrast agent for MRI. *Physiol Chem Phys Med NMR*, 16(2):105–112, 1984.

[60] J. F. Griffith, D. K. Yeung, G. E. Antonio, S. Y. Wong, T. C. Kwok, J. Woo, and P. C. Leung. Vertebral marrow fat content and diffusion and perfusion indexes in women with varying bone density: MR evaluation. *Radiology*, 241(3):831–838, 2006.

[61] W. Grunder, M. Kanowski, M. Wagner, and A. Werner. Visualization of pressure distribution within loaded joint cartilage by application of angle-sensitive NMR microscopy. *Magn Reson Med*, 43(6):884–891, 2000.

[62] W. Grunder, M. Wagner, and A. Werner. MR-microscopic visualization of anisotropic internal cartilage structures using the magic angle technique. *Magn Reson Med*, 39(3):376–382, 1998.

[63] G. Guglielmi, K. Selby, B. A. Blunt, M. Jergas, D. C. Newitt, H. K. Genant, and S. Majumdar. Magnetic resonance imaging of the calcaneus: preliminary assessment of trabecular bone-dependent regional variations in marrow relaxation

time compared with dual X-ray absorptiometry. *Acad Radiol*, 3(4):336–343, 1996.

[64] E.M. Haacke, R.W. Brown, M.R. Thompson, and R. Venkatesan. *Magnetic resonance imaging. Physical principles and sequence design*. John Wiley & Sons, New York, 1999.

[65] E.L. Hahn. Spin echoes. *Phys Rev*, 80(4):580–594, 1950.

[66] P. A. Hardy, A. C. Ridler, C. B. Chiarot, D. B. Plewes, and R. M. Henkelman. Imaging articular cartilage under compression–cartilage elastography. *Magn Reson Med*, 53(5):1065–1073, 2005.

[67] T. Hayami, M. Pickarski, G. A. Wesolowski, J. McLane, A. Bone, J. Destefano, G. A. Rodan, and T. Duong le. The role of subchondral bone remodeling in osteoarthritis: reduction of cartilage degeneration and prevention of osteophyte formation by alendronate in the rat anterior cruciate ligament transection model. *Arthritis Rheum*, 50(4):1193–1206, 2004.

[68] W. C. Hayes and A. J. Bodine. Flow-independent viscoelastic properties of articular cartilage matrix. *J Biomech*, 11(8-9):407–419, 1978.

[69] W. C. Hayes, L. M. Keer, G. Herrmann, and L. F. Mockros. A mathematical analysis for indentation tests of articular cartilage. *J Biomech*, 5(5):541–551, 1972.

[70] R. M. Henkelman, G. J. Stanisz, J. K. Kim, and M. J. Bronskill. Anisotropy of NMR properties of tissues. *Magn Reson Med*, 32(5):592–601, 1994.

[71] W. Herzog and S. Federico. Considerations on joint and articular cartilage mechanics. *Biomech Model Mechanobiol*, 5(2-3):64–81, 2006.

[72] T. Hildebrand and P. Ruegsegger. Quantification of bone microarchitecture with the structure model index. *Comput Methods Biomech Biomed Engin*, 1(1):15–23, 1997.

[73] D. J. Hunter, Y. Q. Zhang, X. Tu, M. Lavalley, J. B. Niu, S. Amin, A. Guermazi, H. Genant, D. Gale, and D. T. Felson. Change in joint space width: hyaline articular cartilage loss or alteration in meniscus? *Arthritis Rheum*, 54(8):2488–2495, 2006.

[74] A. K. Jeffery. Osteophytes and the osteoarthritic femoral head. *J Bone Joint Surg Br*, 57(3):314–324, 1975.

[75] M. D. Jergas, S. Majumdar, J. H. Keyak, I. Y. Lee, D. C. Newitt, S. Grampp, H. B. Skinner, and H. K. Genant. Relationships between young modulus of elasticity, ash density, and MRI derived effective transverse relaxation T_2* in tibial specimens. *J Comput Assist Tomogr*, 19(3):472–479, 1995.

[76] Y. Jiang, J. Zhao, P. Augat, X. Ouyang, Y. Lu, S. Majumdar, and H. K. Genant. Trabecular bone mineral and calculated structure of human bone specimens scanned by peripheral quantitative computed tomography: relation to biomechanical properties. *J Bone Miner Res*, 13(11):1783–1790, 1998.

[77] H. Jinnai, H. Watashiba, T. Kajihara, Y. Nishikawa, M. Takahashi, and M. Ito. Surface curvatures of trabecular bone microarchitecture. *Bone*, 30(1):191–194, 2002.

[78] L.C. Junqueira, J. Carneiro, and R.O. Kelley. *Basic histology, 7th edition*. Appleton & Lange, Norwalk, 1992.

[79] J. S. Jurvelin, J. P. Arokoski, E. B. Hunziker, and H. J. Helminen. Topographical variation of the elastic properties of articular cartilage in the canine knee. *J Biomech*, 33(6):669–675, 2000.

[80] J. S. Jurvelin, M. D. Buschmann, and E. B. Hunziker. Optical and mechanical

determination of Poisson's ratio of adult bovine humeral articular cartilage. *J Biomech*, 30(3):235–241, 1997.

[81] C. Kang, M. Paley, R. Ordidge, and R. Speller. In vivo MRI measurements of bone quality in the calcaneus: a comparison with DXA and ultrasound. *Osteoporos Int*, 9:65–74, 1999.

[82] J. A. Kanis. Diagnosis of osteoporosis and assessment of fracture risk. *Lancet*, 359(9321):1929–1936, 2002.

[83] J. A. Kanis and C. C. Gluer. An update on the diagnosis and assessment of osteoporosis with densitometry. committee of scientific advisors, International Osteoporosis Foundation. *Osteoporos Int*, 11(3):192–202, 2000.

[84] J. H. Kaufman, R. R. Regatte, L. Bolinger, J. B. Kneeland, R. Reddy, and J. S. Leigh. A novel approach to observing articular cartilage deformation in vitro via magnetic resonance imaging. *J Magn Reson Imaging*, 9(5):653–662, 1999.

[85] K. Keinan-Adamsky, H. Shinar, and G. Navon. The effect of detachment of the articular cartilage from its calcified zone on the cartilage microstructure, assessed by ^{2}H-spectroscopic double quantum filtered MRI. *J Orthop Res*, 23:109–117, 2005.

[86] K. Keinan-Adamsky, H. Shinar, and G. Navon. Multinuclear NMR and MRI studies of the maturation of pig articular cartilage. *Magn Reson Med*, 55(3):532–540, 2006.

[87] J. H. Kellgren and J. S. Lawrence. Radiological assessment of osteo-arthrosis. *Ann Rheum Dis*, 16(4):494–502, 1957.

[88] D. K. Kim, T. L. Ceckler, V. C. Hascall, A. Calabro, and R. S. Balaban. Analysis of water-macromolecule proton magnetization transfer in articular cartilage. *Magn Reson Med*, 29(2):211–215, 1993.

[89] K. Király, M. M. Hyttinen, T. Lapveteläinen, M. Elo, I. Kiviranta, J. Dobai, L. Modis, H. J. Helminen, and J. P. Arokoski. Specimen preparation and quantification of collagen birefringence in unstained sections of articular cartilage using image analysis and polarizing light microscopy. *Histochem J*, 29(4):317–327, 1997.

[90] K. Király, T. Lapveteläinen, J. Arokoski, K. Törrönen, L. Modis, I. Kiviranta, and H. J. Helminen. Application of selected cationic dyes for the semiquantitative estimation of glycosaminoglycans in histological sections of articular cartilage by microspectrophotometry. *Histochem J*, 28(8):577–590, 1996.

[91] C. Kittel. *Intoduction to solid state physics, 7th edition*. John Wiley & sons, New York, 1996.

[92] I. Kiviranta, J. Jurvelin, M. Tammi, A. M. Säämänen, and H. J. Helminen. Microspectrophotometric quantitation of glycosaminoglycans in articular cartilage sections stained with safranin O. *Histochemistry*, 82(3):249–255, 1985.

[93] S. H. Koenig. The need for electron paramagnetic resonance and water exchange-rate data for understanding small magnetic resonance imaging contrast agents and their macromolecular complexes. *Invest Radiol*, 29 Suppl 2:S127–130., 1994.

[94] H. Koepp, W. Eger, C. Muehleman, A. Valdellon, J. A. Buckwalter, K. E. Kuettner, and A. A. Cole. Prevalence of articular cartilage degeneration in the ankle and knee joints of human organ donors. *J Orthop Sci*, 4(6):407–412, 1999.

[95] R.K. Korhonen, M. S. Laasanen, J. Töyräs, R. Lappalainen, H. Helminen, and

J. Jurvelin. Fibril reinforced poroelastic model predicts specifically mechanical behavior of normal, proteoglycan depleted and collagen degraded articular cartilage. *J Biomech*, 36:1373–1379, 2003.

[96] K. Kose, Y. Matsuda, T. Kurimoto, S. Hashimoto, Y. Yamazaki, T. Haishi, S. Utsuzawa, H. Yoshioka, S. Okada, M. Aoki, and T. Tsuzaki. Development of a compact MRI system for trabecular bone volume fraction measurements. *Magn Reson Med*, 52(2):440–444, 2004.

[97] J. Kurkijärvi, M. Nissi, I. Kiviranta, J. Jurvelin, and M. T. Nieminen. Delayed gadolinium-enhanced MRI of cartilage (dGEMRIC) and T_2 characteristics of human knee articular cartilage: topographical variation and relationships to mechanical properties. *Magn Reson Med*, 52:41–46, 2004.

[98] M. S. Laasanen, J. Töyräs, R. K. Korhonen, J. Rieppo, S. Saarakkala, M. T. Nieminen, J. Hirvonen, and J. S. Jurvelin. Biomechanical properties of knee articular cartilage. *Biorheology*, 40(1-3):133–140, 2003.

[99] W. M. Lai, J. S. Hou, and V. C. Mow. A triphasic theory for the swelling and deformation behaviors of articular cartilage. *J Biomech Eng*, 113(3):245–258, 1991.

[100] A. Laib and P. Ruegsegger. Calibration of trabecular bone structure measurements of in vivo three-dimensional peripheral quantitative computed tomography with 28-µm-resolution microcomputed tomography. *Bone*, 24(1):35–39, 1999.

[101] P. J. Lattanzio, K. W. Marshall, A. Z. Damyanovich, and H. Peemoeller. Macromolecule and water magnetization exchange modeling in articular cartilage. *Magn Reson Med*, 44(6):840–851, 2000.

[102] K. B. Lehner, H. P. Rechl, J. K. Gmeinwieser, A. F. Heuck, H. P. Lukas, and H. P. Kohl. Structure, function, and degeneration of bovine hyaline cartilage: assessment with MR imaging in vitro. *Radiology*, 170(2):495–499, 1989.

[103] R. K. Lemperg, S. E. Larsson, and S. O. Hjertquist. Distribution of water and glycosaminoglycans in different layers of cattle articular cartilage. *Isr J Med Sci*, 7(3):419–421, 1971.

[104] C. C. Lester and R. G. Bryant. Magnetically coupled paramagnetic relaxation agents. *Magn Reson Med*, 24(2):236–242, 1992.

[105] M. Levitt and R. Freeman. Compensation for pulse imperfections in NMR spin-echo experiments. *J Magn Reson*, 43:65–80, 1981.

[106] F. Linde and I. Hvid. Stiffness behaviour of trabecular bone specimens. *J Biomech*, 20(1):83–89, 1987.

[107] T. M. Link, S. Majumdar, P. Augat, J. C. Lin, D. Newitt, N. E. Lane, and H. K. Genant. Proximal femur: assessment for osteoporosis with T_2^* decay characteristics at MR imaging. *Radiology*, 209(2):531–536, 1998.

[108] T. M. Link, S. Majumdar, J. C. Lin, D. Newitt, P. Augat, X. Ouyang, A. Mathur, and H. K. Genant. A comparative study of trabecular bone properties in the spine and femur using high resolution MRI and CT. *J Bone Miner Res*, 13(1):122–132, 1998.

[109] T. M. Link, V. Vieth, R. Langenberg, N. Meier, A. Lotter, D. Newitt, and S. Majumdar. Structure analysis of high resolution magnetic resonance imaging of the proximal femur: in vitro correlation with biomechanical strength and BMD. *Calcif Tissue Int*, 72(2):156–165, 2003.

[110] S. Lüsse, H. Claassen, T. Gehrke, J. Hassenpflug, M. Schunke, M. Heller, and

C. C. Gluer. Evaluation of water content by spatially resolved transverse relaxation times of human articular cartilage. *Magn Reson Imaging*, 18(4):423–430, 2000.

[111] J. Magland, B. Vasilic, and F. W. Wehrli. Fast low-angle dual spin-echo (FLADE): a new robust pulse sequence for structural imaging of trabecular bone. *Magn Reson Med*, 55(3):465–471, 2006.

[112] C. F. Maier, S. G. Tan, H. Hariharan, and H. G. Potter. T_2 quantitation of articular cartilage at 1.5 T. *J Magn Reson Imaging*, 17(3):358–364, 2003.

[113] S. Majumdar. Quantitative study of the susceptibility difference between trabecular bone and bone marrow: computer simulations. *Magn Reson Med*, 22(1):101–110, 1991.

[114] S. Majumdar, H. K. Genant, S. Grampp, D. C. Newitt, V. H. Truong, J. C. Lin, and A. Mathur. Correlation of trabecular bone structure with age, bone mineral density, and osteoporotic status: in vivo studies in the distal radius using high resolution magnetic resonance imaging. *J Bone Miner Res*, 12(1):111–118, 1997.

[115] S. Majumdar, D. Newitt, M. Jergas, A. Gies, E. Chiu, D. Osman, J. Keltner, J. Keyak, and H. Genant. Evaluation of technical factors affecting the quantification of trabecular bone structure using magnetic resonance imaging. *Bone*, 17(4):417–430, 1995.

[116] S. Majumdar, D. Thomasson, A. Shimakawa, and H. K. Genant. Quantitation of the susceptibility difference between trabecular bone and bone marrow: experimental studies. *Magn Reson Med*, 22(1):111–127, 1991.

[117] H. J. Mankin, H. Dorfman, L. Lippiello, and A. Zarins. Biochemical and metabolic abnormalities in articular cartilage from osteo-arthritic human hips. II. correlation of morphology with biochemical and metabolic data. *J Bone Joint Surg Am*, 53(3):523–537, 1971.

[118] A. Maroudas. Physicochemical properties of cartilage in the light of ion exchange theory. *Biophys J*, 8(5):575–595, 1968.

[119] A. Maroudas, H. Evans, and L. Almeida. Cartilage of the hip joint. Topographical variation of glycosaminoglycan content in normal and fibrillated tissue. *Ann Rheum Dis*, 32(1):1–9., 1973.

[120] A. Maroudas, H. Muir, and J. Wingham. The correlation of fixed negative charge with glycosaminoglycan content of human articular cartilage. *Biochim Biophys Acta*, 177(3):492–500, 1969.

[121] A. Maroudas and R. Schneiderman. "free" and "exchangeable" or "trapped" and "non-exchangeable" water in cartilage. *J Orthop Res*, 5(1):133–138, 1987.

[122] H. Matsui, M. Shimizu, and H. Tsuji. Cartilage and subchondral bone interaction in osteoarthrosis of human knee joint: a histological and histomorphometric study. *Microsc Res Tech*, 37(4):333–342, 1997.

[123] D. McKeag, B. W. Smith, R. Edminster, T. Laird, J. Clark, and S. Herron. Estimating the severity of osteoarthritis with magnetic resonance spectroscopy. *Semin Arthritis Rheum*, 21(4):227–238, 1992.

[124] C. A. McKenzie, A. Williams, P. V. Prasad, and D. Burstein. Three-dimensional delayed gadolinium-enhanced MRI of cartilage (dGEMRIC) at 1.5T and 3.0T. *J Magn Reson Imaging*, 24(4):928–933, 2006.

[125] T. Mendlik, S. C. Faber, J. Weber, J. Hohe, E. Rauch, M. Reiser, and C. Glaser. T_2 quantitation of human articular cartilage in a clinical setting at 1.5 T: implemen-

tation and testing of four multiecho pulse sequence designs for validity. *Invest Radiol*, 39(5):288–299, 2004.

[126] N. M. Menezes, M. L. Gray, J. R. Hartke, and D. Burstein. T_2 and $T_{1\rho}$ MRI in articular cartilage systems. *Magn Reson Med*, 51(3):503–509, 2004.

[127] S. Michaeli, D. J. Sorce, D. Idiyatullin, K. Ugurbil, and M. Garwood. Transverse relaxation in the rotating frame induced by chemical exchange. *J Magn Reson*, 169(2):293–299, 2004.

[128] V. Mlynarik, A. Degrassi, R. Toffanin, F. Vittur, M. Cova, and R. S. Pozzi-Mucelli. Investigation of laminar appearance of articular cartilage by means of magnetic resonance microscopy. *Magn Reson Imaging*, 14(4):435–442, 1996.

[129] V. Mlynarik, S. Trattnig, M. Huber, A. Zembsch, and H. Imhof. The role of relaxation times in monitoring proteoglycan depletion in articular cartilage. *J Magn Reson Imaging*, 10(4):497–502., 1999.

[130] J. M. Modl, L. A. Sether, V. M. Haughton, and J. B. Kneeland. Articular cartilage: correlation of histologic zones with signal intensity at MR imaging. *Radiology*, 181(3):853–855, 1991.

[131] E. F. Morgan, H. H. Bayraktar, and T. M. Keaveny. Trabecular bone modulus-density relationships depend on anatomic site. *J Biomech*, 36(7):897–904, 2003.

[132] V. C. Mow, D. C. Fithian, and M. A. Kelly. Fundamentals of articular cartilage and meniscus biomechanics. In J. W. Ewing, editor, *Articular cartilage and knee joint function: basic science and arthroscopy*, pages 1–18. Raven Press Ltd., New York, 1990.

[133] V. C. Mow, S. C. Kuei, W. M. Lai, and C. G. Armstrong. Biphasic creep and stress relaxation of articular cartilage in compression: Theory and experiments. *J Biomech Eng*, 102(1):73–84, 1980.

[134] V. C. Mow, A. Ratcliffe, and A. R. Poole. Cartilage and diarthrodial joints as paradigms for hierarchical materials and structures. *Biomaterials*, 13(2):67–97, 1992.

[135] V. C. Mow, W. Zhu, and A. Ratcliffe. Structure and function of articular cartilage and meniscus. In V. C. Mow and W. C. Hayes, editors, *Basic orthopaedic biomechanics*, pages 143–198. Raven Press, Ltd, New York, 1991.

[136] H. Muir. The chondrocyte, architect of cartilage. biomechanics, structure, function and molecular biology of cartilage matrix macromolecules. *Bioessays*, 17(12):1039–1048, 1995.

[137] D. Nag, G. P. Liney, P. Gillespie, and K. P. Sherman. Quantification of T_2 relaxation changes in articular cartilage with in situ mechanical loading of the knee. *J Magn Reson Imaging*, 19(3):317–322, 2004.

[138] M. T. Nieminen, N. Menezes, A. Williams, and D. Burstein. T_2 of articular cartilage in the presence of Gd-DTPA^{2-}. *Magn Reson Med*, 51:1147–1152, 2004.

[139] M. T. Nieminen, J. Töyräs, M. S. Laasanen, J. Silvennoinen, H.J. Helminen, and J.S. Jurvelin. Prediction of biomechanical properties of articular cartilage with quantitative magnetic resonance imaging. *J Biomech*, 37:321–328, 2004.

[140] M. T. Nieminen, J. Töyräs, J. Rieppo, J. M. Hakumäki, J. Silvennoinen, H. J. Helminen, and J. S. Jurvelin. Quantitative MR microscopy of enzymatically degraded articular cartilage. *Magn Reson Med*, 43(5):676–681, 2000.

[141] M.T. Nieminen, J. Rieppo, J. Silvennoinen, J. Töyräs, J.M. Hakumäki, M.M. Hyttinen, H.J. Helminen, and J.S. Jurvelin. Spatial assessment of articular carti-

lage proteoglycans with Gd-DTPA -enhanced T_1 imaging. *Magn Reson Med*, 48(4):640–648, 2002.

[142] M.T. Nieminen, J. Rieppo, J. Töyräs, J.M. Hakumäki, M.J. Silvennoinen, M.M. Hyttinen, H.J. Helminen, and J.S. Jurvelin. T_2 relaxation reveals spatial collagen architecture in articular cartilage: a comparative quantitative MRI and polarized light microscopic study. *Magn Reson Med*, 46(3):487–493, 2001.

[143] M.J. Nissi, J. Töyräs, M.S. Laasanen, J. Rieppo, S. Saarakkala, R. Lappalainen, J.S. Jurvelin, and M.T. Nieminen. Proteoglycan and collagen sensitive MRI evaluation of normal and degenerated articular cartilage. *J Orthop Res*, 22:557–564, 2004.

[144] T. Nojiri, N. Watanabe, T. Namura, W. Narita, K. Ikoma, T. Suginoshita, H. Takamiya, H. Komiyama, H. Ito, T. Nishimura, and T. Kubo. Utility of delayed gadolinium-enhanced MRI (dGEMRIC) for qualitative evaluation of articular cartilage of patellofemoral joint. *Knee Surg Sports Traumatol Arthrosc*, pages 1–6, 2006.

[145] S. F. Othman, H. Xu, T. J. Royston, and R. L. Magin. Microscopic magnetic resonance elastography (μMRE). *Magn Reson Med*, 54(3):605–615, 2005.

[146] F. Palmieri, F. De Keyzer, F. Maes, and I. Van Breuseghem. Magnetization transfer analysis of cartilage repair tissue: a preliminary study. *Skeletal Radiol*, 2006.

[147] J. R. Parsons and J. Black. The viscoelastic shear behavior of normal rabbit articular cartilage. *J Biomech*, 10(1):21–29, 1977.

[148] J. Pfeuffer, I. Tkac, and R. Gruetter. Extracellular-intracellular distribution of glucose and lactate in the rat brain assessed noninvasively by diffusion-weighted ^{1}H nuclear magnetic resonance spectroscopy in vivo. *J Cereb Blood Flow Metab*, 20(4):736–746, 2000.

[149] L. Pothuaud, B. Van Rietbergen, L. Mosekilde, O. Beuf, P. Levitz, C. L. Benhamou, and S. Majumdar. Combination of topological parameters and bone volume fraction better predicts the mechanical properties of trabecular bone. *J Biomech*, 35(8):1091–1099, 2002.

[150] K. Potter, L. H. Kidder, I. W. Levin, E. N. Lewis, and R. G. Spencer. Imaging of collagen and proteoglycan in cartilage sections using Fourier transform infrared spectral imaging. *Arthritis Rheum*, 44(4):846–855, 2001.

[151] E. L. Radin. Osteoarthrosis. what is known about prevention. *Clin Orthop Relat Res*, (222):60–65, 1987.

[152] E. L. Radin. The aetiology and treatment of osteoarthrosis and how to elucidate them. *Rheumatology in Europe*, 27(2):47–48, 1998.

[153] P. Raux, P. R. Townsend, R. Miegel, R. M. Rose, and E. L. Radin. Trabecular architecture of the human patella. *J Biomech*, 8(1):1–7, 1975.

[154] R. R. Regatte, S. V. Akella, A. Borthakur, J. B. Kneeland, and R. Reddy. Proteoglycan depletion-induced changes in transverse relaxation maps of cartilage: comparison of T_2 and $T_{1\rho}$. *Acad Radiol*, 9(12):1388–1394, 2002.

[155] R. R. Regatte, S. V. Akella, J. H. Lonner, J. B. Kneeland, and R. Reddy. $T_{1\rho}$ relaxation mapping in human osteoarthritis (OA) cartilage: comparison of $T_{1\rho}$ with T_2. *J Magn Reson Imaging*, 23:547–553, 2006.

[156] R. R. Regatte, S. V. Akella, A. J. Wheaton, A. Borthakur, J. B. Kneeland, and R. Reddy. $T_{1\rho}$-relaxation mapping of human femoral-tibial cartilage in vivo. *J Magn Reson Imaging*, 18(3):336–341, 2003.

[157] R. R. Regatte, J. H. Kaufman, E. A. Noyszewski, and R. Reddy. Sodium and proton MR properties of cartilage during compression. *J Magn Reson Imaging*, 10(6):961–967, 1999.

[158] J. Rieppo, J. Hallikainen, J.S. Jurvelin, H.J. Helminen, and M. M. Hyttinen. Novel quantitative polarization microscopic assessment of cartilage and bone birefringence, orientation and anisotropy. In *49th Annual Meeting of the Orthopaedic Research Society*, page 570, New Orleans, Louisiana, 2003.

[159] J. Rieppo, U. Siitonen, E. P. Halmesmäki, M. S. Laasanen, J. Töyräs, S. Saarakkala, I. Kiviranta, M. M. Hyttinen, J. S. Jurvelin, and H. J. Helminen. FTIRI-characterization of human patellar cartilage - comparison to light microscopy and mechanical testing. In *49th Annual Meeting of the Orthopaedic Research Society*, page 290, New Orleans, Louisiana, 2003.

[160] E. Rommel and R. Kimmich. Volume-selective determination of the spin-lattice relaxation time in the rotating frame $T_{1\rho}$, and $T_{1\rho}$ imaging. *Magn Reson Med*, 12(2):209–218, 1989.

[161] E. M. Roos and L. Dahlberg. Positive effects of moderate exercise on glycosaminoglycan content in knee cartilage: a four-month, randomized, controlled trial in patients at risk of osteoarthritis. *Arthritis Rheum*, 52(11):3507–3514, 2005.

[162] E. Roux and L. De Broe. Contrast agents in magnetic resonance imaging. *J Belge Radiol*, 71(1):31–36, 1988.

[163] J. D. Rubenstein, J. K. Kim, and R. M. Henkelman. Effects of compression and recovery on bovine articular cartilage: appearance on MR images. *Radiology*, 201(3):843–850, 1996.

[164] J. D. Rubenstein, J. K. Kim, I. Morova-Protzner, P. L. Stanchev, and R. M. Henkelman. Effects of collagen orientation on MR imaging characteristics of bovine articular cartilage. *Radiology*, 188(1):219–226, 1993.

[165] J. Samosky, D. Burstein, E. Grimson, R. Howe, S. Martin, and M. Gray. Spatially-localized correlation of dGEMRIC-measured GAG distribution and mechanical stiffness in the human tibial plateau. *J Orthop Res*, 23(1):93–101, 2005.

[166] G. E. Santyr, R. M. Henkelman, and M. J. Bronskill. Spin locking for magnetic resonance imaging with application to human breast. *Magn Reson Med*, 12(1):25–37, 1989.

[167] C. A. Sell, J. N. Masi, A. Burghardt, D. Newitt, T. M. Link, and S. Majumdar. Quantification of trabecular bone structure using magnetic resonance imaging at 3 Tesla – calibration studies using microcomputed tomography as a standard of reference. *Calcif Tissue Int*, 76(5):355–364, 2005.

[168] G. S. Seo, J. Aoki, H. Moriya, O. Karakida, S. Sone, H. Hidaka, and T. Katsuyama. Hyaline cartilage: in vivo and in vitro assessment with magnetization transfer imaging. *Radiology*, 201(2):525–530, 1996.

[169] R. E. Sepponen, J. A. Pohjonen, J. T. Sipponen, and J. I. Tanttu. A method for $T_{1\rho}$ imaging. *J Comput Assist Tomogr*, 9(6):1007–1011, 1985.

[170] L. A. Setton, H. Tohyama, and V. C. Mow. Swelling and curling behaviors of articular cartilage. *J Biomech Eng*, 120(3):355–361, 1998.

[171] E. M. Shapiro, A. Borthakur, R. Dandora, A. Kriss, J. S. Leigh, and R. Reddy. Sodium visibility and quantitation in intact bovine articular cartilage using high field ^{23}Na MRI and MRS. *J Magn Reson*, 142(1):24–31, 2000.

[172] E. M. Shapiro, A. Borthakur, A. Gougoutas, and R. Reddy. ^{23}Na MRI accurately measures fixed charge density in articular cartilage. *Magn Reson Med*, 47(2):284–291, 2002.

[173] H. Shinar and G. Navon. Multinuclear NMR and microscopic MRI studies of the articular cartilage nanostructure. *NMR Biomed*, 19(7):877–893, 2006.

[174] F. H. Silver, G. Bradica, and A. Tria. Do changes in the mechanical properties of articular cartilage promote catabolic destruction of cartilage and osteoarthritis? *Matrix Biol*, 23(7):467–476, 2004.

[175] J. Soulhat, M. D. Buschmann, and A. Shirazi-Adl. A fibril-network-reinforced biphasic model of cartilage in unconfined compression. *J Biomech Eng*, 121(3):340–347, 1999.

[176] T. D. Spector, D. J. Hart, J. Byrne, P. A. Harris, J. E. Dacre, and D. V. Doyle. Definition of osteoarthritis of the knee for epidemiological studies. *Ann Rheum Dis*, 52(11):790–794, 1993.

[177] G. J. Stanisz and R. M. Henkelman. Gd-DTPA relaxivity depends on macromolecular content. *Magn Reson Med*, 44(5):665–667, 2000.

[178] A. Stevens and J.S. Lowe. *Human histology, 2nd edition*. Mosby, London, 1997.

[179] C. J. Tiderius, L. E. Olsson, H. de Verdier, P. Leander, O. Ekberg, and L. Dahlberg. Gd-DTPA^{2-}-enhanced MRI of femoral knee cartilage: a dose-response study in healthy volunteers. *Magn Reson Med*, 46(6):1067–1071, 2001.

[180] C. J. Tiderius, L. E. Olsson, P. Leander, O. Ekberg, and L. Dahlberg. Delayed gadolinium-enhanced MRI of cartilage (dGEMRIC) in early knee osteoarthritis. *Magn Reson Med*, 49(3):488–492, 2003.

[181] S. Tomiha, N. Iita, F. Okada, T. Furuya, K. Kose, and T. Haishi. Trabecular bone volume fraction measurements of a large number of subjects using a compact MRI. *Magn Reson Imaging*, 23(10):1011–1015, 2005.

[182] H. Toumi, I. Higashiyama, D. Suzuki, T. Kumai, G. Bydder, D. McGonagle, P. Emery, J. Fairclough, and M. Benjamin. Regional variations in human patellar trabecular architecture and the structure of the proximal patellar tendon enthesis. *J Anat*, 208(1):47–57, 2006.

[183] C. H. Turner. Yield behavior of bovine cancellous bone. *J Biomech Eng*, 111(3):256–260, 1989.

[184] C. H. Turner. Biomechanics of bone: determinants of skeletal fragility and bone quality. *Osteoporos Int*, 13(2):97–104, 2002.

[185] C. H. Turner and D. B. Burr. Basic biomechanical measurements of bone: a tutorial. *Bone*, 14(4):595–608, 1993.

[186] J. Töyräs, J. Rieppo, M. T. Nieminen, H. J. Helminen, and J. S. Jurvelin. Characterization of enzymatically induced degradation of articular cartilage using high frequency ultrasound. *Phys Med Biol*, 44(11):2723–2733, 1999.

[187] D. Ulrich, B. van Rietbergen, A. Laib, and P. Ruegsegger. The ability of three-dimensional structural indices to reflect mechanical aspects of trabecular bone. *Bone*, 25(1):55–60, 1999.

[188] B. C. Vande Berg, J. Malghem, F. E. Lecouvet, and B. Maldague. Magnetic resonance imaging of normal bone marrow. *Eur Radiol*, 8(8):1327–1334, 1998.

[189] M. Venn and A. Maroudas. Chemical composition and swelling of normal and osteoarthrotic femoral head cartilage. I. chemical composition. *Ann Rheum Dis*, 36(2):121–129, 1977.

[190] M. F. Venn. Chemical composition of human femoral head cartilage: influence of topographical position and fibrillation. *Ann Rheum Dis*, 38(1):57–62., 1979.

[191] L. Wachsmuth, H. P. Juretschke, and R. X. Raiss. Can magnetization transfer magnetic resonance imaging follow proteoglycan depletion in articular cartilage? *Magma*, 5(1):71–78, 1997.

[192] A. Watanabe, Y. Wada, T. Obata, T. Ueda, M. Tamura, H. Ikehira, and H. Moriya. Delayed gadolinium-enhanced MR to determine glycosaminoglycan concentration in reparative cartilage after autologous chondrocyte implantation: preliminary results. *Radiology*, 239(1):201–208, 2006.

[193] J.S. Wayne, K.A. Kraft, K.J. Shields, C. Yin, J.R. Owen, and D.G. Disler. MR imaging of normal and matrix-depleted cartilage: Correlation with biomechanical function and biochemical composition. *Radiology*, 228:493–499, 2003.

[194] F. W. Wehrli and M. A. Fernandez-Seara. Nuclear magnetic resonance studies of bone water. *Ann Biomed Eng*, 33(1):79–86, 2005.

[195] F. W. Wehrli, H. K. Song, P. K. Saha, and A. C. Wright. Quantitative MRI for the assessment of bone structure and function. *NMR Biomed*, 19(7):731–764, 2006.

[196] A. J. Wheaton, F. L. Casey, A. J. Gougoutas, G. R. Dodge, A. Borthakur, J. H. Lonner, H. R. Schumacher, and R. Reddy. Correlation of $T_{1\rho}$ with fixed charge density in cartilage. *J Magn Reson Imaging*, 20(3):519–525, 2004.

[197] A. J. Wheaton, G. R. Dodge, A. Borthakur, J. B. Kneeland, H. R. Schumacher, and R. Reddy. Detection of changes in articular cartilage proteoglycan by $T_{1\rho}$ magnetic resonance imaging. *J Orthop Res*, 23:102–108, 2005.

[198] A. J. Wheaton, G. R. Dodge, D. M. Elliott, S. B. Nicoll, and R. Reddy. Quantification of cartilage biomechanical and biochemical properties via $T_{1\rho}$ magnetic resonance imaging. *Magn Reson Med*, 54(5):1087–1093, 2005.

[199] A. Williams, A. Gillis, C. McKenzie, B. Po, L. Sharma, L. Micheli, B. McKeon, and D. Burstein. Glycosaminoglycan distribution in cartilage as determined by delayed gadolinium-enhanced MRI of cartilage (dGEMRIC): potential clinical applications. *AJR Am J Roentgenol*, 182(1):167–172, 2004.

[200] W.S.C. Williams. *Nuclear and particle physics*. Oxford University Press Inc., New York, 1991.

[201] Y. Xia. Relaxation anisotropy in cartilage by NMR microscopy (µMRI) at 14- µm resolution. *Magn Reson Med*, 39(6):941–949, 1998.

[202] Y. Xia, J. B. Moody, and H. Alhadlaq. Orientational dependence of T_2 relaxation in articular cartilage: A microscopic MRI (µMRI) study. *Magn Reson Med*, 48(3):460–469, 2002.

[203] Y. Xia, J. B. Moody, N. Burton-Wurster, and G. Lust. Quantitative *in situ* correlation between microscopic MRI and polarized light microscopy studies of articular cartilage. *Osteoarthritis Cartilage*, 9(5):393–406., 2001.

[204] A. A. Young, P. Stanwell, A. Williams, J. A. Rohrsheim, D. A. Parker, B. Giuffre, and A. M. Ellis. Glycosaminoglycan content of knee cartilage following posterior cruciate ligament rupture demonstrated by delayed gadolinium-enhanced magnetic resonance imaging of cartilage (dGEMRIC). A case report. *J Bone Joint Surg Am*, 87(12):2763–2767, 2005.

[205] J.H. Zar. *Biostatical Analysis, 2nd Edition*. Prentice Hall Inc., Englewood Cliffs, N.J., 1984.

ORIGINAL PUBLICATIONS

Kuopio University Publications C. Natural and Environmental Sciences

C 199. Tarvainen, Tanja. Computational Methods for Light Transport in Optical Tomography.
2006. 123 p. Acad. Diss.

C 200. Heikkinen, Päivi. Studies on Cancer-related Effects of Radiofrequency Electromagnetic Fields. 2006. 165 p. Acad. Diss.

C 201. Laatikainen, Tarja. Pesticide induced responses in ectomycorrhizal fungi and symbiont Scots pine seedlings.
2006. 180 p. Acad. Diss.

C 202. Tiitta, Markku. Non-destructive methods for characterisation of wood material.
2006. 70 p. Acad. Diss.

C 203. Lehesranta, Satu. Proteomics in the Detection of Unintended Effects in Genetically Modified Crop Plants.
2006. 71 p. Acad. Diss.

C 204. Boman, Eeva. Radiotherapy forward and inverse problem applying Boltzmann transport equation.
2007. 138 p. Acad. Diss.

C 205. Saarakkala, Simo. Pre-Clinical Ultrasound Diagnostics of Articular Cartilage and Subchondral Bone.
2007. 96 p. Acad. Diss.

C 206. Korhonen, Samuli-Petrus. FLUFF-BALL, a Fuzzy Superposition and QSAR Technique - Towards an Automated Computational Detection of Biologically Active Compounds Using Multivariate Methods.
2007. 154 p. Acad. Diss.

C 207. Matilainen, Merja. Identification and characterization of target genes of the nuclear reseptors VDR and PPARs: implementing in silico methods into the analysis of nuclear receptor regulomes.
2007. 112 p. Acad. Diss.

C 208. Anttonen, Mikko J. Evaluation of Means to Increase the Content of Bioactive Phenolic Compounds in Soft Fruits.
2007. 93 p. Acad. Diss.

C 209. Pirkanniemi, Kari. Complexing agents: a study of short term toxicity, catalytic oxidative degradation and concentrations in industrial waste waters.
2007. 83 p. Acad. Diss.

C 210. Leppänen, Teemu. Effect of fiber orientation on cockling of paper.
2007. 96 p. Acad. Diss.

C 211. Nieminen, Heikki. Acoustic Properties of Articular Cartilage: Effect of Structure, Composition and Mechanical Loading.
2007. 80 p. Acad. Diss.

C 212. Tossavainen, Olli-Pekka. Shape estimation in electrical impedance tomography.
2007. 64 p. Acad. Diss.

C 213. Georgiadis, Stefanos. State-Space Modeling and Bayesian Methods for Evoked Potential Estimation.
2007. 179 p. Acad. Diss.